Technical Physics Letters, Vol. 29, No. 9, 2003, pp. 701–704. Translated from Pis'ma v Zhurnal Tekhnicheskoĭ Fiziki, Vol. 29, No. 17, 2003, pp. 1–7.

Atom-Bombardment-Induced Electron Emission from a Cathode in a Glow Discharge: Example of an Open Discharge

A. R. Sorokin

Institute of Semiconductor Physics, Siberian Division, Russian Academy of Sciences, Novosibirsk, 630090 Russia

e-mail: IFP@isp.nsc.ru

Received November 29, 2002

Abstract—An analysis of the glow discharge conditions shows that processes involved in this phenomenon should be described in terms of the electron emission coefficients γ determined in a technical (γ_t) rather than in an ultrahigh vacuum. The results of calculations of the electron beam formation efficiency η in a glow discharge, performed using the γ_t values, agree well with the experimentally measured efficiencies. Further refinement of these calculations is inexpedient because of unavoidable uncertainty of the γ values under real discharge conditions. © *2003 MAIK "Nauka/Interperiodica".*

Data on the coefficients γ of electron emission from cathodes bombarded with high-energy (tens to hundreds electronvolts) ions (γ_i) and/or neutral atoms (γ_a) can differ by one to two orders of magnitude depending on the vacuum conditions of measurements: ultrahigh ($p < 10^{-9}$ Torr) [1, 2] versus technical ($p \gg 10^{-9}$ Torr) [3]. Atoms of such energies are present in still insufficiently studied glow discharges featuring a potential drop within 1–10 kV near the cathode, in particular in the so-called open discharge in systems with anode grid [4].

Therefore, a question naturally arises as to which γ values correspond to the real discharge conditions. This knowledge is important, in particular, for estimating the efficiency and elucidating the mechanism of electron beam formation in glow discharges. In this paper, the above question is analyzed in the case of an open discharge representing a kind of the glow discharge [5, 6].

1. An "anomalously high" efficiency of the electron beam formation under the open discharge conditions was used as a basis for the statements that open discharge is essentially a new type of discharge of the photoemission type and attracted attention to the mechanism of this discharge. In all papers devoted to the open discharge, the energy efficiency η of the electron beam formation is determined as the ratio of the collector current j_c to the total current, whereas traditional electron guns are characterized by the efficiency parameter defined as $\approx\gamma(\gamma + 1)^{-1}$ and measured with the aid of calorimeters [7]. However, it was recently demonstrated that the parameter γ depends on the fraction k of electrons generated within the discharge gap volume and reaching the collector, so that $\eta \approx \mu(\gamma + k)(\gamma + 1)^{-1}$. According to the results of the field measurements [9], typical open discharge satisfies the conditions of electron "runaway" [8] in the entire gap so that $k \approx 1$ and, hence, η is virtually independent of γ and is approximately equal to μ (the geometric transparency of the anode grid). This conclusion breaks the basis of reasoning behind the photoelectron nature of the open discharge [9, 10], but the question concerning the real energy efficiency of the electron beam formation still remains unanswered.

The presence of a sufficiently strong field over the entire discharge gap width d can be established without measuring the field distribution. One has only to check that the anomalous discharge current [11]

$$j_{AD} = 2.5 \times 10^{-12} p^2 (U_{cf})^3 \quad (1)$$

(which is equivalent to the current in a discharge with the cathode fall of the potential U_{cf} equal to the applied voltage U) is significantly greater than the measured value: $j_{AD}/j \gg 1$ (i.e., either the cathode fall region is incompletely formed or a significant part of the applied voltage U drops outside this region having a length of l_{cf}). According to the data in [10, Table 2], the condition $j_{AD}/j \gg 1$ is usually satisfied in the open discharge. Nevertheless, it was suggested [10] that all the applied voltage U can drop in the region l_{cf} that is on the order of the ion charge transfer length λ_{ct} and, hence, the condition of electron "runaway" is not satisfied outside l_{cf}.

The results of calculations [9] of the parameter $\gamma_{ia} = \gamma_i + \Sigma\gamma_a$ for helium, performed with allowance of the energy losses for the high-energy atoms involved in elastic collisions, gave the γ_{ia} values lower by a factor of 2.3–3 than the coefficients [4] determined with neglect of such losses. Note that, on taking into account

that the appearance of an electric field at the cathode leads to an increase in γ (e.g., by a factor of 2–3 [7] for $E_c = 2 \times 10^5$ V/cm typical of the open discharge), the discrepancy becomes significantly smaller. A still greater discrepancy with the calculation [4] was obtained in [10]. However, the calculations in [9] were performed using an approximate value of the total cross section σ_{es} for elastic scattering, rather than the transport value σ_{tr} characterizing the true energy losses of impinging particles [12]. The estimates in [10] were obtained assuming, in particular, that $l_{cf} \sim \lambda_{ct}$ for $\gamma_a = 0$. The problem of applicability of the coefficients γ measured in technical and ultrahigh vacuum was also discussed in [10], but the γ values were incorrect.

Below, we will consider these questions and discrepancies and determine whether the atom-bombardment-induced electron emission from a cathode can account for the electron beam formation efficiency observed in a glow discharge of the open type.

2. Using a formula for the potential energy of interaction of helium atoms [13], $V_{He} = Cr^{-5}$ ($C = 3.5 \times 10^{-40}$ eV cm^5). For colliding heavy particles (moving with nonthermal velocities), the elastic scattering is restricted to small angles θ and the corresponding differential scattering cross section is given by the formula [14]

$$d\sigma_{es} = 0.2(8C/3E_a)^{2/5}\theta^{-12/5}d\Omega. \quad (2)$$

In classical mechanics, this cross section diverges for small θ values, while the transport cross section converges to

$$\sigma_{tr} = f(1-\cos\theta)(d\sigma_{es}/d\Omega)d\Omega$$
$$\approx \int (d\sigma_{es}/d\Omega)\theta^3 d\theta = (\pi/8)(8C/3E_a)^{2/5}(\theta_{max})^{8/5}. \quad (3)$$

Substituting $\theta_{max} \sim 1$ into expression (3), we obtain for the atoms with $E_a = 100$ eV an estimate of $\sigma_{tr} = 1.5 \times 10^{-17}$ cm^2. For scattering at large angles, a rough overstated estimate is provided by the approximation of hard (impermeable) spheres: $\sigma = 8 \times 10^{-17}$ cm^2 ($\sigma = \pi r^2$, where $r \approx (C/E_a)^{1/5}$). Then, the total cross section is estimated as $\sigma_{tr} + \sigma = 9.5 \times 10^{-17}$ cm^2, which is still about two times smaller than $\sigma_{es} = 1.8 \times 10^{-16}$ cm^2 in [9]. In addition, we have to take into account (i) the contribution to the electron emission due to atoms acquiring a large proportion of the energy of impinging atoms scattered by large angles and (ii) the presence of a strong field on the cathode surface.

The energy efficiency determined by calorimetry under the anomalous discharge conditions [15] amounted to 70% for $U = 2.4$ kV (no data were reported for 2.4 kV $< U \leqslant$ 10 kV), which exactly coincides with the value calculated in [4]. For increasing the electron emission, the experiments in [15] were performed with He containing 1% O_2. The results of experiments performed in this study showed that adding O_2 (using duralumin cathode) does not enhance the electron emission (instead, the current even decreased for a given U value). However, the presence of oxygen significantly increases stability of the discharge, which allowed the system to operate at higher U and j values or at severalfold greater working gas pressures. Probably, this very effect was implied in [15] and mentioned in [7], where it was pointed out that attaining high E values at the cathode surface was facilitated in thin-film structures with high-ohmic aluminum oxide coatings (for regenerating these coatings, it was recommended to add O_2 to the working gas [7]).

Thus, the above analysis shows that the γ_{ia} values calculated in [4] correctly characterize the energy efficiency of the electron beam formation in this glow discharge.

3. Let us consider the estimates of γ_{ia} obtained in [10] for $j > 1$ A/cm^2 under the assumption that $l_{cf} \sim \lambda_{ct}$ and $\gamma_{ia} \approx \gamma_i$ (fast atoms do not appear). It can be shown that the condition $l_{cf} \sim \lambda_{ct}$ cannot be satisfied in a typical open discharge with the parameters (according to oscillograms in [10, Fig. 3]) $p_{He} = 30$ Torr, $U = 5.5$ kV at a maximum current of $j = 35$ A/cm^2 (which corresponds to an equivalent value of $j_{AD} = 370$ A/cm^2), and a duration of $\tau \approx 100$ ns. Indeed, assuming that $\sigma_{ct} = 10^{-15}$ cm^2, we obtain for the field strength at the cathode surface $E_c \approx 2U/l_{cf} = 2U\sigma_{ct}N_a = 10^7$ V/cm.

Typical times of the onset of explosive emission processes on the cathode surface in vacuum for $E_c = 10^6$ V/cm amount to a few nanoseconds [16]. As is known [7], the vacuum breakdown takes place at $E_c = (3–5) \times 10^5$ V/cm. A discharge ($\tau \approx 100$ ns) in the gap with a mechanically polished aluminum cathode converts into a spark at $E_c = (0.5–1) \times 10^5$ V/cm, while the same in the gap with an electrochemically polished cathode is observed at $E_c = 4.5 \times 10^5$ V/cm [11].

It is interesting to compare the field strength $E_c = 2.7 \times 10^5$ V/cm experimentally measured for $p_{He} = 20$ Torr, $U = 7.8$ kV, and $j = 45$ A/cm^2 [9] to the value calculated assuming $l_{cf} \sim \lambda_{ct}$. The latter estimate is again on the order of 10^7 V/cm.

Thus, the experiments show that the condition $l_{cf} \sim \lambda_{ct}$ cannot be satisfied in a typical open discharge because of the onset of explosive emission processes on the cathode surface. Moreover, for the photoelectron discharge considered in [10], an additional question arises as to the source of ions completely screening the field in the gap beyond the limits of $\lambda_{ct} \ll l_{cf}$ in an anomalous discharge with a current one to two orders of magnitude lower than that in the open discharge. Therefore, a strong field is present in the entire gap featuring the open discharge; the parameter η is independent of γ

and, hence, does not characterize the energy efficiency of the open discharge (in agreement with [8]).

4. In [10], the estimates of γ_{ia} were also obtained for $l_{cf} \gg \lambda_{ct}$ using the γ values determined under the conditions of ultrahigh and technical vacuum. Let us consider the latter case, which is closer to the real discharge conditions.

Judging by the reference cited in [10], the formula $\gamma_{ia} \sim 0.2 \times 10^{-3}U$ for aluminum cathode was obtained based on the data of [7, Fig. 4.7(b)]. For $U = 6$ kV, this formula yields $\gamma_{ia} = 1.2$. However, the figure in [7] is reproduced (from the original paper [17]) with an error: the figures indicating cathode materials at the curves are mixed up. In fact, the aluminum cathode corresponds to $U = 5$ kV, for which the above formula yields $\gamma_{ia} = 4$. Moreover, the data in [17] were obtained in vacuum (rather than in a discharge) and refer only to ions accelerated by a voltage of U in a gap of length l", so that we obtain an estimate for γ_i (rather than γ_{ia}) in a field of $E_c = 2 \times 10^3$ V/cm: $\gamma_i = 4$. This value is significantly greater than that for a technical vacuum [3] in the absence of electric field (an almost tenfold smaller value of 0.48 was obtained for $eU = 6$ keV in an ultrahigh vacuum [10]).

In addition, it should be noted that the conditions of determining γ in ultrahigh vacuum are identical to those recommended for the investigations of discharge in vacuum [18]: (i) residual pressure not exceeding 10^{-9} Torr; (ii) vacuum system not employing oil diffusion pumps, organic lubricants, and organic seals; (iii) adsorption coverage on the electrode surfaces not exceeding 1/10 monolayer; etc. Obviously, these conditions cannot be satisfied under real discharge conditions. According to monograph [19], experiments give evidence that cleaner surfaces correspond to smaller γ values, the difference in γ between clean and contaminated surfaces being more pronounced in the region of low energies. In particular, γ as a function of the Li^+ ion energy for an atomically clean tungsten surface exceeds the values for the same surface covered with O_2 and N_2 adlayers by one order of magnitude for energies below 350 eV and by a factor of 2–3, above 500 eV (the increase in γ_i related to the kinetic emission equally refers to γ_a). We can also make a recourse to monograph [20], where γ values coinciding with those measured in ultrahigh vacuum were obtained in a lower vacuum of $\sim 10^{-7}$ Torr, but the target was preliminarily heated nearly to the melting point. Then the heating was terminated and the γ value was measured within a few seconds after vanishing of the thermal emission (γ started increasing immediately after that). Finally, it is necessary to emphasize the coincidence of the measured energy efficiency [15] with the results of calculations [4] based on the γ values determined under technical vacuum conditions [3] (the same data were used for the calculations in [9]). Note that a typical open discharge is characterized by $E_a \lesssim 300$ eV.

The above considerations lead to an important conclusion: the real discharge conditions are best described using either the results of very early determinations of γ [21] or the recent data obtained in technical vacuum [3] (the results of these measurements coincide [3]). Such a choice eliminates the considerable uncertainty in γ pointed out in [12].

5. While not dwelling upon all the questions considered in [10], let us discuss the results of measurements of the current j and the efficiency η as functions of the cathode area S involved in the discharge. In the experiment [10], the S value was varied from 0.014 to 1 cm^2 by partly shielding the cathode with a ring-shaped mica plate with a thickness below d. The anode grid has the same area S. The observed decrease on j and η with increasing S, which was explained in [10] by changes in the geometry of cathode illumination from the drift space, are in fact caused by the edge effects. Near the edge of the hole in the mica plate, the field lines exhibit bending as in a hole cathode [7]. As a result, the cathode area involved in the discharge decreases (as can be seen in [8, Fig. 2]) and the current j drops with decreasing S. The value of η decreases as a result of the electron beam scattering on the continuous anode part, which is caused by the same edge effects.

Conclusions. The assumption [10] that all voltage drops in a region of λ_{ct} is at variance with experiment, since such conditions would give rise to explosive processes on the cathode.

In addition to what was established in [8], the above considerations confirm that, in a typical open discharge, the electric field is strong over the entire gap and the parameter η is independent of the coefficient γ. This fact breaks the basis of reasoning for a photoelectron nature of the open discharge [9, 10].

The results of γ_{ia} calculations [4] correctly describe the energy efficiency of the electron beam formation in a glow discharge. Further refinement of such calculations is inexpedient because of unavoidable uncertainty in the γ_i and γ_a values under real discharge conditions with heavy particle energies from tens to hundreds of electronvolts.

The main conclusion is that processes in a glow discharge cannot be correctly evaluated using the electron emission coefficients γ determined under the ideal ultrahigh vacuum conditions. The best estimates are obtained using the γ values measured in a technical vacuum.

Acknowledgments. The author is grateful to D.A. Shapiro for his help in obtaining estimates of the elastic scattering cross sections for helium atoms.

REFERENCES

1. G. Lakits, A. Arnau, and H. Winter, Phys. Rev. B **42**, 15 (1990).
2. G. Lakits, F. Aumayr, M. Heim, *et al.*, Phys. Rev. A **42**, 5780 (1990).

3. H. C. Hayden and N. G. Utterback, Phys. Rev. A **135**, 1575 (1964).
4. A. R. Sorokin, Pis'ma Zh. Tekh. Fiz. **26** (24), 89 (2000) [Tech. Phys. Lett. **26**, 1114 (2000)].
5. A. R. Sorokin, Pis'ma Zh. Tekh. Fiz. **28** (9), 14 (2002) [Tech. Phys. Lett. **28**, 361 (2002)].
6. A. R. Sorokin, Opt. Atmos. Okeana **14**, 1062 (2001).
7. M. A. Zav'yalov, Yu. E. Kreĭndel', A. A. Novikov, and L. P. Shanturin, *Plasma Processes in Electron Guns* (Énergoatomizdat, Moscow, 1989).
8. A. R. Sorokin, Pis'ma Zh. Tekh. Fiz. **29** (4), 86 (2003) [Tech. Phys. Lett. **29**, 171 (2003)].
9. G. V. Kolbychev, Opt. Atmos. Okeana **14**, 1056 (2001).
10. A. P. Bokhan and P. A. Bokhan, Opt. Atmos. Okeana **15**, 216 (2002).
11. K. A. Klimenko and Yu. D. Korolev, Zh. Tekh. Fiz. **60** (9), 138 (1990) [Sov. Phys. Tech. Phys. **35**, 1084 (1990)].
12. Yu. P. Raĭzer, *Gas Discharge Physics* (Nauka, Moscow, 1987; Springer-Verlag, Berlin, 1991).
13. I. Amdur and J. E. Jordan, J. Chem. Phys. **34**, 1525 (1961).
14. L. D. Landau and E. M. Lifshits, *Course of Theoretical Physics*, Vol. 1: *Mechanics* (Nauka, Moscow, 1982; Pergamon, New York, 1988).
15. Z. Yu, J. J. Rocca, and G. J. Collins, J. Appl. Phys. **54**, 131 (1983).
16. Yu. D. Korolev and G. A. Mesyats, *The Physics of Pulse Breakdown* (Nauka, Moscow, 1991).
17. H. C. Bourne, R. W. Cloud, and J. G. Trump, J. Appl. Phys. **26**, 596 (1955).
18. V. L. Granovskiĭ, N. B. Rozanova, L. N. Kosmarskiĭ, *et al.*, Radiotekh. Élektron. (Moscow), No. 12, 2102 (1963).
19. I. N. Slivkov, V. N. Mikhailov, N. I. Sidorov, *et al.*, *Vacuum Breakdown and Electrical Discharge in Vacuum* (Atomizdat, Moscow, 1966).
20. U. A. Arifov, *Interaction of Atomic Particles with a Solid Surface* (Nauka, Moscow, 1968; Consultants Bureau, New York, 1969).
21. A. Z. Rostagni, Physik **88**, 55 (1934).

Translated by P. Pozdeev

Technical Physics Letters, Vol. 29, No. 9, 2003, pp. 705–707. Translated from Pis'ma v Zhurnal Tekhnicheskoĭ Fiziki, Vol. 29, No. 17, 2003, pp. 8–15.

Magnetic Field Sensor Based on Compensated Silicon

M. K. Bakhadyrkhanov, Kh. M. Iliev, K. S. Ayupov, and O. É. Sattorov

Tashkent State Technical University, Tashkent, Uzbekistan

e-mail: tstu@uzpak.uz

Received April 8, 2003

Abstract—The phenomenon of negative magnetoresistance in compensated silicon doped with manganese has been studied. The possibility of using this effect in magnetic field sensors is assessed. © *2003 MAIK "Nauka/Interperiodica".*

Magnetic field sensors are widely used in various fields of technology. Operation of existing semiconductor devices of this kind is based on the Hall effect leading to the positive magnetoresistance in semiconductors and related device structures [1–6]. The main disadvantage of these sensors is a relatively low sensitivity ($\Delta\rho/\rho_0 \leq 5\%$). We believe that the most promising way to increase the sensitivity of magnetic field sensors is to use the new physical phenomenon of negative magnetoresistance discovered in compensated silicon doped with impurities possessing incompletely filed *d* electron shells [7–9].

We have studied the phenomenon of negative magnetoresistance in compensated silicon doped with manganese and assessed the possibility of using this effect in magnetic field sensors. The samples of compensated Si⟨B,Mn⟩ were obtained by manganese diffusion from the gas phase into the initial *p*-type single crystal silicon (KDB-1 grade) with a resistivity of 1 Ω cm. The temperature and duration of the diffusion annealing were varied so as to obtain compensated and overcompensated samples of the *p*- and *n*-types with an initial room-temperature zero-field resistivity ρ_0 in the range from 10^2 to 10^5 Ω cm. Homogeneity of the distribution of electrically active Mn atoms in the volume of silicon was ensured by using a constant source of dopant, a sufficiently large diffusion time, and a high rate of cooling (above 200 K/s).

More than 20 samples prepared under identical conditions were studied for each value of the initial resistivity (with a scatter in ρ_0 not exceeding 25%). The results of statistical data processing showed that the scatter of $\Delta\rho/\rho_0$ values measured in a magnetic field for such a group 20 of samples did not exceed 0.5% (i.e., the scatter in ρ_0 did not significantly influence the relative magnetoresistance). The characteristics of degradation on storage were determined in a series of 10 samples possessing various initial resistivities, which were kept for one month at a temperature of about 50°C. No changes in the resistivity or $\Delta\rho/\rho_0$ values were observed to within the experimental accuracy, which confirmed the stability of the parameters of Si⟨B,Mn⟩ at temperatures up to 50°C.

The room-temperature magnetoresistance of compensated Si⟨B,Mn⟩ samples was measured in both transverse (**H** ⊥ **J**) and longitudinal (**H** ∥ **J**) magnetic fields. The measurements were performed in the dark and under illumination with a total spectrum of an incandescent lamp. The values of $\Delta\rho/\rho_0$ were determined by measuring the current in a sample at a constant applied voltage (the electric field strength was 50 V/cm). The magnetic field strength was varied from 0 to 20 kOe, which corresponded to the conditions of weak magnetic field. It was found that reversal of the magnetic field direction (180° rotation) did not change the $\Delta\rho/\rho_0$ values. In contrast to the case of overcompensated *n*-Si⟨B,Mn⟩, where the magnetoresistance was always positive (irrespective of the resistivity), the samples of compensated *p*-Si⟨B,Mn⟩ exhibited a number of very interesting phenomena.

Figure 1 shows plots of a relative change in the resistivity versus transverse magnetic field strength *H* (**H** ⊥ **J**) for a series of compensated *p*-Si⟨B,Mn⟩ samples with various resistivities. As can be seen from these data, the samples with $\rho_0 \leq 3 \times 10^2$ Ω cm exhibit a small positive magnetoresistance (comparable with that of the initial silicon) in the entire range of magnetic fields (Fig. 1, curve *1*). In the samples with $\rho_0 \geq 5 \times 10^2$ Ω cm, the magnetoresistance is initially positive but then changes sign and increases in absolute value with the magnetic field strength (curves *2* and *3*). As the resistivity of *p*-Si⟨B,Mn⟩ increases, the point of the magnetoresistance inversion shifts toward smaller values of the magnetic field strength and the samples with $\rho_0 > 5 \times 10^3$ Ω cm exhibit negative magnetoresistance in the entire range of transverse magnetic fields.

The maximum negative magnetoresistance was observed in the samples of *p*-Si⟨B,Mn⟩ with $\rho_0 \approx (6–8) \times 10^3$ Ω cm. It should be noted that the absolute value of $\Delta\rho/\rho_0$ in these samples is greater than that of the posi-

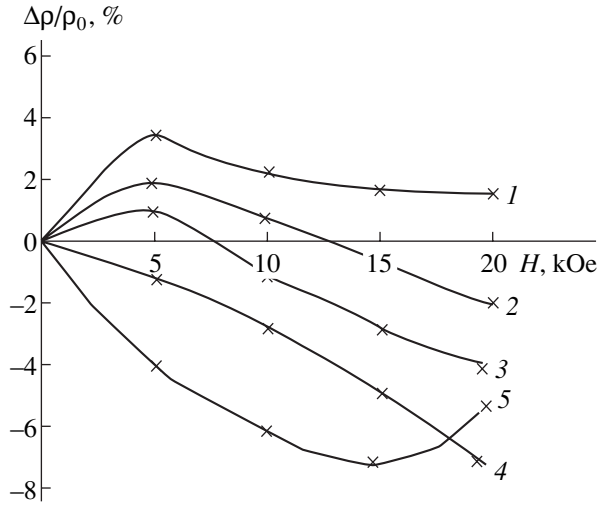

Fig. 1. Plots of the dark magnetoresistance versus magnetic field strength measured at $T = 300$ K and $E = 50$ V/cm for Si⟨B,Mn⟩ samples with various initial resistivities $\rho_0 = 2.5 \times 10^2$ (*1*), 5×10^2 (*2*), 1.5×10^3 (*3*), 6×10^3 (*4*), and 6.5×10^4 Ω cm.

tive magnetoresistance in overcompensated samples measured under identical conditions.

As is known from published data [10, 11], strongly compensated *p*-Si⟨B,Mn⟩ samples are characterized by a high photosensitivity, which allows the resistivity of this material to be controlled by varying the illumination level. Figure 2 presents a plot of the resistivity versus total light intensity for Si⟨B,Mn⟩ samples with $\rho_0 = 1.3 \times 10^5$ Ω cm measured at $T = 300$ K and $E = 50$ V/cm in the absence of magnetic field. Estimates obtained from the results of measurements of the photoelectromagnetic effect showed that the error of resistivity determination related to this effect does not exceed 0.9% for $H = 20$ kOe and $I = 50$ lx and decreases with the resistivity.

In contrast to the usual low-ohmic semiconductors, strongly compensated silicon doped with manganese is characterized by a very strong dependence of the magnetoresistance on the illumination intensity. We have studied this dependence for strongly compensated Si⟨B,Mn⟩ samples with $\rho_0 = 1.3 \times 10^5$ and 6.2×10^3 Ω cm exposed to a magnetic field of $H = 20$ kOe and illuminated with the light of an incandescent lamp. Figure 3 (curve *1*) shows the plot of $\Delta\rho/\rho_0$ versus I for a sample with $\rho_0 = 1.3 \times 10^5$ Ω cm, possessing a maximum concentration of electrically active Mn atoms. As can be seen, the curve has two clearly pronounced regions. In the first region, where the illumination intensity increases from zero to $I = 50$ lx, the magnetoresistance rapidly grows and reaches a maximum $(\Delta\rho/\rho_0)_{max}$ at $I = 45$–50 lx. As the illumination intensity grows further, the negative magnetoresistance decreases in absolute value and is close to zero for a large total light intensity ($I > 100$ lx). The results of these measurements showed that the I values corresponding to $(\Delta\rho/\rho_0)_{max}$ shift toward higher intensities with decreasing resistivity of the sample (Fig. 3, curve *2*). It should be noted that the negative magnetoresistance reaches an anomalously large absolute value (up to 50%) only for a certain total illumination intensity.

We believe that the negative magnetoresistance strongly depends on the compensating dopant (Mn) concentration. In order to check this hypothesis, we prepared samples of strongly compensated *p*-Si⟨B,Mn⟩

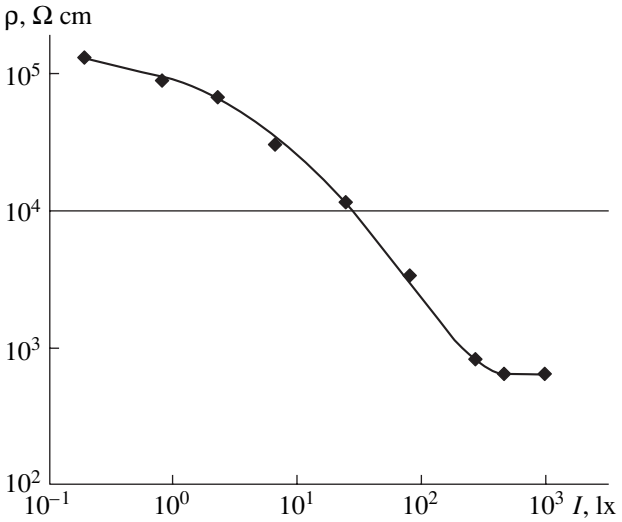

Fig. 2. A plot of the resistivity versus total light intensity for Si⟨B,Mn⟩ samples with $\rho_0 = 1.3 \times 10^5$ Ω cm measured at $T = 300$ K and $E = 50$ V/cm in the absence of magnetic field.

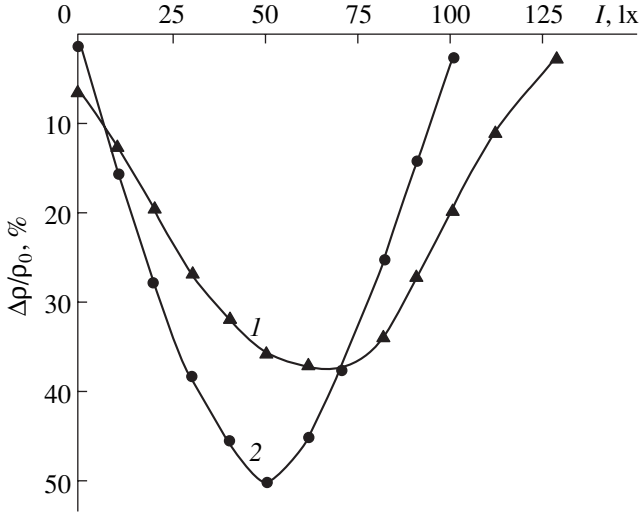

Fig. 3. Plots of the magnetoresistance versus total light intensity for Si⟨B,Mn⟩ samples prepared from KDB-1 wafers with $\rho_0 = 1.3 \times 10^5$ (*1*) and 6.2×10^3 Ω cm (*2*) and measured at $T = 300$ K, $E = 50$ V/cm, and $H = 20$ kOe.

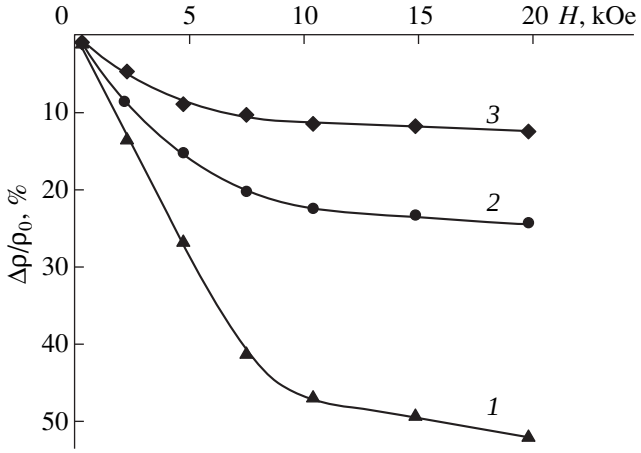

Fig. 4. Plots of the magnetoresistance versus magnetic field strength measured under illumination at I = 50 lx, E = 50 V/cm and T = 300 K for Si⟨B,Mn⟩ samples with the same initial resistivity $\rho_0 = 1.3 \times 10^5$ Ω cm and different compensating dopant concentrations, prepared from various initial materials: (*1*) KDB-1; (*2*) KDB-10; (*3*) KDB-100.

using initial wafers of KDB-1, KDB-10, and KDB-100 possessing equal resistivities, in which the density of electrically active Mn atoms varied from 10^{14} to 2×10^{16} cm^{-3}. Figure 4 shows the plots of negative magnetoresistance versus magnetic field strength for these samples. As can be seen from these data, the absolute value of magnetoresistance in Si⟨B,Mn⟩ with $N_{Mn} = 2 \times 10^{16}$ cm^{-3} is 5–6 times that with $N_{Mn} = 10^{14}$ cm^{-3} under otherwise equal conditions (resistivity, illumination, temperature, etc.). It was established that the points where the linear variation of the magnetoresistance exhibits a break shift toward greater magnetic fields with increasing density of electrically active Mn atoms. This behavior can be related to an increase in the density of Mn atoms with the d^5s^0 electron structure, that is, in the density of magnetically sensitive centers. Note that the very small magnetoresistance of the initial and control (manganese-free) samples is also indicative of a large contribution of Mn atoms to the magnetoresistance of compensated silicon.

The results presented above show that, under certain conditions, the sensitivity of magnetic field sensors with negative magnetoresistance, based on a compensated silicon doped with manganese, can be more than ten times greater than the sensitivity of analogous devices based on a material with positive magnetoresistance. Thus, by controlling the illumination intensity, selecting the initial resistivity, and controlling the concentration of introduced electrically active Mn atoms, it is possible to obtain a material with maximum negative magnetoresistance, which can serve as a basis for the development of new, highly effective magnetic field sensors.

REFERENCES

1. V. I. Stafeev and É. I. Karakushan, *Magnetodiodes* (Nauka, Moscow, 1975).
2. I. M. Vikulin and V. I. Stafeev, *Physics of Semiconductor Devices* (Radio i Svyaz', Moscow, 1980).
3. S. A. Gredeskul and V. D. Freĭlikher, Usp. Fiz. Nauk **160**, 239 (1990) [Sov. Phys. Usp. **33**, 134 (1990)].
4. A. I. Olemskoĭ, Usp. Fiz. Nauk **166**, 697 (1996) [Phys. Usp. **39**, 651 (1996)].
5. A. G. Groshev and S. G. Novokshonov, Fiz. Tverd. Tela (St. Petersburg) **42**, 1322 (2000) [Phys. Solid State **42**, 1361 (2000)].
6. A. I. Abramovich and A. V. Michurin, Fiz. Tverd. Tela (St. Petersburg) **42**, 2052 (2000) [Phys. Solid State **42**, 2113 (2000)].
7. D. G. Andrianov, A. S. Savel'ev, V. I. Fistul', *et al.*, Fiz. Tekh. Poluprovodn. (Leningrad) **9**, 210 (1975) [Sov. Phys. Semicond. **9**, 141 (1975)].
8. D. G. Andrianov, G. V. Lazareva, V. I. Fistul', *et al.*, Fiz. Tekh. Poluprovodn. (Leningrad) **9**, 1555 (1975) [Sov. Phys. Semicond. **9**, 1026 (1975)].
9. É. M. Omel'yanovskiĭ and V. I. Fistul', *Transition Metal Impurities in Semiconductors* (Metallurgiya, Moscow, 1983; IOP, 1986).
10. M. K. Bakhadyrkhanov, S. Zainobidinov, T. S. Kamilov, and A. T. Teshabaev, Fiz. Tekh. Poluprovodn. (Leningrad) **9**, 76 (1975) [Sov. Phys. Semicond. **9**, 48 (1975)].
11. M. K. Bakhadyrkhanov, K. A. Azizov, and A. T. Teshabaev, Fiz. Tekh. Poluprovodn. (Leningrad) **14**, 1028 (1980) [Sov. Phys. Semicond. **14**, 1363 (1980)].

Translated by P. Pozdeev

Technical Physics Letters, Vol. 29, No. 9, 2003, pp. 708–711. Translated from Pis'ma v Zhurnal Tekhnicheskoĭ Fiziki, Vol. 29, No. 17, 2003, pp. 16–22.

The Energy of a Photon Flux in a Dielectric Waveguide

I. V. Dzedolik

Tauride National University, Simferopol, Ukraine

e-mail: dzedolik@crimea.edu

Received February 10, 2003; in final form, March 14, 2003

Abstract—Propagation of a monochromatic electromagnetic field in a round dielectric waveguide is considered within the framework of a quantum field approach. A Hamiltonian of the photon flux–dielectric waveguide system is found and expressions for the system energy in the linear and nonlinear approximations are obtained. It is shown that the energy depends on the ratio of the numbers of photons with left- and right-handed helicity.

Theoretical analysis of the electromagnetic field propagation in dielectric waveguides is performed quite well using methods of classical electrodynamics [1]. However, the electromagnetic field in a medium represents a flux of photons and, hence, can be considered as a quantum object [2, p. 109]. For this reason, some features of the field dynamics in a waveguide is more conveniently treated within the framework of quantum theory.

Let us consider the propagation of a monochromatic electromagnetic field in a round dielectric waveguide in the linear approximation. Using the Hamiltonian gage $\Phi = 0$ (see [3, p. 16] and [4, p. 76]) for the potentials in a stationary medium in the absence of free charges and currents, the field equations in the waveguide under consideration can be written as

$$\nabla^2\mathbf{A} - \frac{\varepsilon}{c^2}\frac{\partial^2\mathbf{A}}{\partial t^2} = \nabla(\nabla\mathbf{A}), \tag{1}$$

where $\varepsilon = \varepsilon(r)$ is the dielectric permittivity of the waveguide as a function of the radial coordinate. Taking into account the axial symmetry of the problem, a solution to Eq. (1) can be selected in the form of $\mathbf{A} = \mathbf{F}(r)\exp[i(\omega t - \beta z + \kappa l\varphi)]$ (where $\kappa = \pm 1$ and $l = 0, 1, 2, \ldots$).The boundary conditions correspond to continuity of the tangential components of the electric field $E_{\varphi, z} = -\partial A_{\varphi, z}/c\partial t$ and magnetic field $B_{\varphi, z} = (\nabla \times \mathbf{A})_{\varphi, z}$ on the waveguide wall with a radius of r_0. Here, the function $\mathbf{F}$ denotes the corresponding polynomials (depending on the profile of permittivity ε) and the propagation constants β_l of the waveguide modes satisfy a characteristic equation obtained from the boundary conditions for $r = r_0$ [1].

Expanding the field inside the waveguide into modes with right- and left-handed circular polarization ($\kappa = \pm 1$), we obtain

$$\mathbf{A} = \sum_l\sum_\kappa \mathbf{F}_l(r) \times \{a_{l\kappa}(t)\exp[i(\beta_l z - \kappa l\varphi)] + a^*_{l\kappa}(t)\exp[-i(\beta_l z - \kappa l\varphi)]\}, \tag{2}$$

where $a_{l\kappa}(t) \sim \exp(-i\omega t)$ are the mode amplitudes. To pass to the quantum theory, let us transform the variables so as to write the field equations in Hamiltonian form. To this end, we introduce the canonical coordinates and momenta [5, p. 20]

$$Q_{l\kappa} = \frac{1}{2}(a_{l\kappa} + a^*_{l\kappa}), \quad P_{l\kappa} = \frac{\omega}{2i}(a_{l\kappa} - a^*_{l\kappa}), \tag{3}$$

which satisfy the equations $\dot{Q}_{l\kappa} = \partial H/\partial P_{l\kappa}$ and $\dot{P}_{l\kappa} = -\partial H/\partial Q_{l\kappa}$ (the upper dot denotes the time derivative). In the new variables (3), vector potential (2) takes the form

$$\mathbf{A} = 2\sum_l\sum_\kappa \mathbf{F}_l(Q_{l\kappa}\cos\phi_{l\kappa} - \omega^{-1}P_{l\kappa}\sin\phi_{l\kappa}), \tag{4}$$

where $\phi_{l\kappa} = \beta_l z - \kappa l\varphi$.

The system Hamiltonian can be found using a classical expression for the energy of a monochromatic electromagnetic field in a nonmagnetic dielectric medium:

$$\tilde{E}_L = \frac{1}{8\pi}\int_V dV(\varepsilon\mathbf{E}^2 + \mathbf{B}^2). \tag{5}$$

Upon substituting expressions for the electric field $\mathbf{E} = -\partial\mathbf{A}/c\partial t$ and magnetic field $\mathbf{B} = \nabla \times \mathbf{A}$ into Eq. (5), we integrate over a finite volume V representing a cylinder with the radius r_0 and the length Λ (proportional to the distance between the adjacent field nodes). Replacing

the canonical variables by operators obeying the commutation rules $[\hat{P}_{l\kappa j}, \hat{Q}_{l\kappa j'}] = -i\hbar\delta_{jj'}$, we transform the expression for the energy to the Hamiltonian: $\tilde{E}_L \longrightarrow \hat{H}_L$. Introducing the annihilation and generation operators

$$a_{l\kappa j} = \frac{1}{\sqrt{2\hbar\omega}}(\omega\hat{Q}_{l\kappa j} + i\hat{P}_{l\kappa j}),$$
$$a^+_{l\kappa j} = \frac{1}{\sqrt{2\hbar\omega}}(\omega\hat{Q}_{l\kappa j} - i\hat{P}_{l\kappa j}) \quad (6)$$

obeying the commutation rules $[a_{l\kappa j}, a^+_{l\kappa j'}] = \delta_{jj'}$, we obtain the Hamiltonian

$$\hat{H}_L = \hbar\omega\sum_l\sum_{\kappa=\pm1}\left[\frac{1}{2}\sum_{j=1,2,3} q_{lj}(a_{l\kappa j}a^+_{l\kappa j} + a^+_{l\kappa j}a_{l\kappa j}) + \kappa l q_{14}(a_{l\kappa z}a^+_{l\kappa\varphi} + a^+_{l\kappa z}a_{l\kappa\varphi})\right], \quad (7)$$

where

$$q_{l1} = \Lambda\int_0^1 dRR\left(\frac{\varepsilon r_0^2}{c^2} + \frac{\beta_l^2 r_0^2 + l^2/R^2}{\omega^2}\right)\mathbf{F}_l^2,$$

$$q_{l2} = \Lambda\int_0^1 dRR\left[\left(\frac{\varepsilon r_0^2}{c^2} + \frac{\beta_l^2 r_0^2 + 1/R^2}{\omega^2}\right)\mathbf{F}_l^2 + \frac{1}{\omega^2}\left(U_l^2\mathbf{F}_l'^2 + \frac{2U_l}{R}\mathbf{F}_l\mathbf{F}_l'\right)\right],$$

$$q_{l3} = \Lambda\int_0^1 dRR\left[\left(\frac{\varepsilon r_0^2}{c^2} + \frac{l^2}{\omega^2 R^2}\right)\mathbf{F}_l^2 + \frac{U_l^2}{\omega^2}\mathbf{F}_l'^2\right],$$

$$q_{l4} = \frac{\Lambda\beta_l r_0}{\omega^2}\int_0^1 dR\mathbf{F}_l^2,$$

$U_l = r_0(\omega^2\varepsilon/c^2 - \beta_l^2)^{1/2}$, and $R = r/r_0$ (prime denotes a derivative with respect to the corresponding argument).

The energy of the system can be expressed in terms of the number of photons $N_{l\kappa j}$ ($j \longrightarrow r, \varphi, z$) in the corresponding mode component:

$$\tilde{E}_L = \hbar\omega\sum_l\sum_{\kappa=\pm1}\left[\sum_{j=1,2,3} q_{lj}\left(N_{l\kappa j} + \frac{1}{2}\right) + \kappa l q_{l4}(\sqrt{N_{l\kappa z}(N_{l\kappa\varphi}+1)} + \sqrt{N_{l\kappa\phi}(N_{l\kappa z}+1)})\right]. \quad (8)$$

In the case when the numbers of photons with the right-handed ($\kappa = 1$) and left-handed ($\kappa = -1$) helicities in the linearly polarized mode component are equal, the terms with the coefficient q_{l4} in Eq. (8) vanish upon summation with respect to κ. Otherwise, when the field represents a superposition of circularly polarized modes with $l \neq 0$, the terms with q_{l4} are not canceled and the energy (8) depends on the relation between the numbers of photons ($N_{l\kappa\varphi}$, $N_{l\kappa z}$) with the left- and right-handed helicities in the corresponding mode component. This can be treated as the dependence of the system energy on the "spin–orbit interaction" [6] of the electromagnetic field in a waveguide, provided that the orbital moment of the field (characterized by the mode index l) in the superposition of modes in the waveguide is nonzero and the spin is characterized by the mode polarization.

A classical interpretation of this phenomenon can be provided by considering each mode with the index $l > 0$ as corresponding to a ray (normal to the wave front at a given point) propagating along the left- or right-handed helix upon reflection from the waveguide walls. If the direction of rotation of a circularly polarized mode coincides with (or is opposite to) that of the helical beam trajectory, the field energy increases (or decreases), so that the asymmetry in the cylindrical system appears as a result of the symmetry breakage in the case of a nonparaxial excitation of the waveguide. Another variant of the classical interpretation of the phenomenon under consideration is based on the theory of generation of the stable circular (CV) and unstable (IV) optical vortices with a difference in the momentum transfer caused by the spin–orbit interaction of the corresponding waveguide modes [7].

The ratio of the system energies for the linear ($\tilde{E}_{LL}$) and circular ($\tilde{E}_{LC}$) mode polarizations,

$$\frac{\tilde{E}_{LL}}{\tilde{E}_{LC}} = \sum_{j=1,2,3} q_{lj}\left(N^{\pm}_{lj} + \frac{1}{2}\right)\left\{\sum_{j=1,2,3} q_{lj}\left(N_{lj} + \frac{1}{2}\right) + \kappa l q_{l4}(\sqrt{N_{lz}(N_{l\varphi}+1)} + \sqrt{N_{l\varphi}(N_{lz}+1)})\right\}^{-1},$$

depends on the number of photons in the corresponding mode components (here, the number of photons in the

linearly and circularly polarized modes are equal: $N_{lj}^{(+)} = N_{lj}^{(-)} = N_{lj\kappa}$). In the particular case of $l = 1$, we put $N_{1x} = N_{1\varphi} + N_{1z} \equiv N$, $q_{1x} = q_{14}$ and obtain $\tilde{E}_{LL}/\tilde{E}_{LC} = (N + 1/2)\{N + 1 + \kappa[\sqrt{a_z N(a_\varphi N + 1)} + \sqrt{a_\varphi N(a_z N + 1)}\,]\}^{-1}$, where $a_\varphi + a_z = 1$. Thus, $\tilde{E}_{LL}/\tilde{E}_{LC}$ can be either smaller or greater than unity, depending on the direction of rotation of the circularly polarized mode ($\kappa = \pm 1$). For laser radiation with $\lambda = 0.63$ μm and a power of $P = 5$ mW, we have $N \approx P \cdot 1c/\hbar\omega = 2.5 \times 10^{15}$. Assuming $a_\varphi + 10^{-7} = 1$, we obtain $\tilde{E}_{LL}/\tilde{E}_{LC} = 0.99937$ for $\kappa = 1$ and $\tilde{E}_{LL}/\tilde{E}_{LC} = 1.00063$ for $\kappa = -1$.

Practical verification of the predicted effect is possible in a relatively simple experiment. If a linearly polarized laser beam passes through a quartz crystal plate of thickness d with the planes parallel to the optical axis, there appears an optical path difference $\Delta d = (n_0 - n_e)d$ between the extraordinary wave (with the refractive index n_e and the electric vector $\mathbf{E}_e$ parallel to the optical axis) and ordinary wave (with the refractive index n_0 and the electric vector $\mathbf{E}_0$ perpendicular to the optical axis). The corresponding phase shift between the ordinary and extraordinary waves is $\Delta\phi = 2\pi\Delta d/\lambda$. This implies that the end of the electric vector $\mathbf{E}$ at the plate output will move by a trajectory described by the equation $x^2/a^2 + y^2/b^2 - 2xy\cos(\Delta\phi)/ab = \sin^2(\Delta\phi)$ [8].

For a normally incident, linearly polarized wave with the electric vector $\mathbf{E}$ oriented at an angle of $\delta = \pi/4$ relative to the optical axis, the amplitudes of the electric vector oscillations along and across the axis are equal: $a = E\cos\delta = E\sin\delta = b$. In a plate of thickness $d = (m + 1/4)\lambda/(n_0 - n_e)$, where $m = 0, 1, 2, \ldots$, $n_0 = 1.54282$, and $n_e = 1.55188$, the output wave acquires a circular polarization. The direction of rotation (clockwise versus anticlockwise) of the $\mathbf{E}$ vector in the transmitted wave is determined by mutual orientation of the $\mathbf{E}$ vector and the optical axis of the plate.

Thus, by rotating the plate in the plane (around the normal), we obtain transmitted radiation with either left- or right-handed circular polarization. Using a microobjective, the output radiation possessing circular (right- or left-handed) or linear polarization (with the plate turned) can be fed to an optical fiber and transmitted to a photodiode connected to a digital voltmeter. By measuring a difference between the voltmeter response to the radiation with right- or left-handed circular and linear polarizations, one can detect the aforementioned energy effect in the fiber waveguide.

Let us take into account the nonlinear response of the dielectric waveguide (e.g., of fused quartz widely used for manufacturing optical fibers). For this purpose, it is necessary to introduce nonlinear terms into the field equations and the energy expression:

$$\nabla^2\mathbf{A} - \frac{\varepsilon}{c^2}\frac{\partial^2\mathbf{A}}{\partial t^2} = \nabla(\nabla\mathbf{A}) + \frac{\alpha_3}{c^4}\frac{\partial}{\partial t}\left(\frac{\partial\mathbf{A}}{\partial t}\right)^3, \tag{9}$$

$$\tilde{E}_{NL} = \frac{1}{8\pi}\int_V dV\left(\varepsilon\mathbf{E}^2 + \frac{\alpha_3}{2}\mathbf{E}^4 + \mathbf{B}^2\right). \tag{10}$$

Here, $\alpha_3 = 4\pi\chi_3$ is a coefficient characterizing the cubic component of the permittivity as a function of the field strength [9]. Assuming that the nonlinear response is small (so that the general mode structure is retained), the Hamiltonian can be represented as a sum of the linear and nonlinear parts, $\hat{H} = \hat{H}_L + \hat{H}_{NL}$, where

$$\hat{H}_{NL} = 8(\hbar\omega)^2\sum_l\sum_{\kappa=\pm1}\tilde{q}_l\left[\sum_j\sum_{j'}(a_{l\kappa j}a_{l\kappa j}a^+_{l\kappa j'}a^+_{l\kappa j'} + a^+_{l\kappa j}a^+_{l\kappa j}a_{l\kappa j'}a_{l\kappa j'} + a_{l\kappa j}a^+_{l\kappa j}a_{l\kappa j'}a^+_{l\kappa j'} + a^+_{l\kappa j}a_{l\kappa j'}a^+_{l\kappa j}a_{l\kappa j'} + a_{l\kappa j}a^+_{l\kappa j}a^+_{l\kappa j'}a_{l\kappa j'} + a^+_{l\kappa j}a_{l\kappa j}a_{l\kappa j'}a^+_{l\kappa j'})\right], \tag{11}$$

$$\tilde{q}_l = \frac{\alpha_3\Lambda r_0^2}{c^4}\int_0^1 dRR\mathbf{F}_l^4.$$

In the nonlinear case under consideration, the energy of the system is $\tilde{E} = \tilde{E}_L + \tilde{E}_{NL}$. The linear term $\tilde{E}_L$ is given by expression (8), while the nonlinear term $\tilde{E}_{NL}$ is determined using Hamiltonian (11):

$$\tilde{E}_{NL} = 48(\hbar\omega)^2\sum_l\sum_{\kappa=\pm1}\tilde{q}_l \times\left\{\sum_{j,j'}\left[N_{l\kappa j}\left(N_{l\kappa j'} + \frac{1}{2}\right) + \frac{1}{2}N_{l\kappa j'}\right] + 2\right\}. \tag{12}$$

As can be seen from this expression, a nonlinear contribution to the system energy in the given approximation (unlike the linear system energy (8)) is independent of the photon helicity κ.

To summarize, the energy of an electromagnetic field propagating in a round dielectric waveguide depends on the relative number of photons with left- and right-handed helicity in the mode component (i.e., on the field polarization). For a superposition of circularly polarized modes in a waveguide, the energy can be either greater or smaller than the energy of linearly polarized modes. This is related to the momentum transfer from the circularly polarized field to the

waveguide. This effect can be used in the development of fiber sensors for the remote measurement of physical quantities.

Acknowledgments. The author is grateful to K.N. Alekseev and P.N. Leifer for fruitful discussions.

REFERENCES

1. A. W. Snyder and J. D. Love, *Optical Waveguide Theory* (Chapman and Hall, London, 1983; Radio i Svyaz', Moscow, 1987).
2. V. L. Ginzburg, *Theoretical Physics and Astrophysics* (Nauka, Moscow, 1987; Pergamon, Oxford, 1979).
3. L. D. Faddeev and A. A. Slavnov, *Gauge Fields: Introduction to Quantum Theory* (Nauka, Moscow, 1988; Addison-Wesley, Redwood, 1990).
4. L. D. Landau and E. M. Lifshits, *Course of Theoretical Physics*, Vol. 2: *The Classical Theory of Fields* (Nauka, Moscow, 1988; Pergamon, Oxford, 1975).
5. V. B. Berestetskiĭ, E. M. Lifshits, and L. P. Pitaevskiĭ, *Course of Theoretical Physics*, Vol. 4: *Quantum Electrodynamics* (Nauka, Moscow, 1989; Pergamon, New York, 1982).
6. V. S. Liberman and B. Ya. Zel'dovich, Phys. Rev. A **46**, 5199 (1992).
7. C. N. Alexeyev, M. S. Soskin, and A. V. Volyar, Semicond. Phys. Quantum Electron. Optoelectron. **3**, 501 (2000).
8. G. S. Landsberg, *Optics* (Nauka, Moscow, 1976).
9. S. A. Akhmanov, V. A. Vysloukh, and A. S. Chirkin, *The Optics of Femtosecond Laser Pulses* (Nauka, Moscow, 1988).

Translated by P. Pozdeev

Technical Physics Letters, Vol. 29, No. 9, 2003, pp. 712–713. Translated from Pis'ma v Zhurnal Tekhnicheskoĭ Fiziki, Vol. 29, No. 17, 2003, pp. 23–27.

Surface Barrier Diode Based on Zinc Selenide with a Passivating Zinc Oxide Film

V. P. Makhniy and V. V. Melnik

Chernivtsi National University, Chernivtsi, Ukraine

e-mail: oe-dpt@chnu.edu.ua

Received February 28, 2003; in final form, April 9, 2003

Abstract—We propose a method of fabricating surface barrier diodes with overlapped metal junction, which provides for a significant decrease in the reverse currents and an increase in the breakdown voltage. © *2003 MAIK "Nauka/Interperiodica".*

An important problem in the technology of surface barrier diodes is related to the development of structures in which breakdown is caused by processes in the volume charge layer rather than by surface and/or edge effects. Various methods have been proposed to eliminate the latter effects, for example, by creating a storage ring with a *p–n* junction, insulating layer, or a groove, by using a structure having the form of a truncated cone, etc. [1].

In this context, we have studied the electrical properties of zinc selenide based surface barrier diodes with overlapped metal junction, which are used as UV photodetectors [2–4]. Elimination of the edge effect would provide for a decrease in the reverse leak currents and a significant increase in the shortwave sensitivity of a photodetector operating in the photodiode regime [5].

The substrates were *n*-ZnSe single crystal wafers with an uncompensated room-temperature donor concentration of $N_d \approx 10^{17}$ cm^{-3} (determined from the Hall effect measurements to within ±10%). The rectifying junction was created by depositing a semitransparent nickel film. The ohmic junctions on the opposite side of the substrate were created by fusing indium at 350°C. The diode fabrication technology has been described in detail elsewhere [3].

Theoretical values of the breakdown voltage for a metal–semiconductor junction, as well as for a sharp *p–n* junction, are given by the formula [1]

$$V_B = 60\left(\frac{E_g}{1.1}\right)^{3/2}\left(\frac{N_d}{10^{16}}\right)^{-3/4}\text{V}, \qquad (1)$$

where E_g is the semiconductor bandgap width. According to formula (1), the diode structures under consideration ($N_d \approx 10^{17}$ cm^{-3}; $E_g \approx 2.7$ eV at 300 K) are expected to have V_B about 40 V. However, the real breakdown voltages of experimental diodes did not exceed 18–20 V (Fig. 1, curve *2*) even despite thorough chemical etching of the substrate crystal in the stage of the rectifying junction formation. This discrepancy is probably caused by the edge effects. In order to eliminate these effects, the metal–ZnSe structures were treated in a concentrated hydrogen peroxide solution known to affect the surface of the base substrate while virtually not interacting with metals used in the rectifying and ohmic junctions on ZnSe [1].

The results of our investigations showed that the aforementioned treatment of the diode structure leads to a significant decrease in the reverse current I at a constant voltage. An analysis of the plots of I versus the time t_a and the temperature T_a of the sample treatment showed evidence of a complicated character of this process. It was found that the $I(t_a)$ curves exhibit a minimum for any V and T_a in the range of voltages and tem-

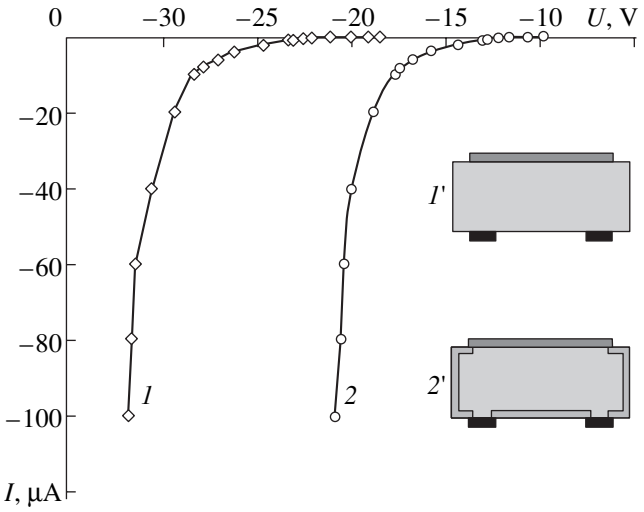

Fig. 1. Ni–ZnSe junctions (*1*, *1*') before and (*2*, *2*) after the treatment with H_2O_2 solution: (*1*, *2*) reverse branches of the current–voltage characteristics; (*1*', *2*') schematic diagrams of the diode structures.

1063-7850/03/2909-0712$24.00 © 2003 MAIK "Nauka/Interperiodica"

peratures studied. Figure 2 shows a typical family of such plots for one of the Ni–ZnSe junctions at T_a = 300 K. It should be noted that analogous effects were observed for all diode structures studied, irrespective of the substrate doping level and the rectifying junction material.

An analysis of the experimental data led us to the conclusion that the observed decrease in the reverse current is related to the formation of a high-resistivity ZnO layer on the free surface of the substrate treated with H_2O_2. This hypothesis was confirmed by the presence of a peak corresponding to the bandgap width of zinc oxide in the reflection spectra of samples upon the treatment. According to [6, 7], the oxidation of ZnSe surface is accompanied by the displacement of selenium with more active hydrogen and the formation of zinc oxide. The process of substitution possesses a diffusion character, whereby the thickness d of the ZnO layer formed in H_2O_2 for the oxidation process duration $t > 160$ s is described by the empirical expression $d \approx 60t^{1/2}$. The data reported in [7] and the results of our measurements indicate that the room-temperature resistivity of zinc oxide falls within 10^8–10^{10} Ω cm.

Thus, the oxide layer plays the role of a passivating film leading to a decrease in the surface recombination rate and, eventually, in the leak current and the total reverse current. It should be noted that the high-resistivity layer appears (due to a diffusion character of the process) under the rectifying junction along the entire perimeter. Although the length of this penetration is not as large, being virtually equal to the thickness of the ZnO layer formed (0.5–1 μm), this insulation is quite sufficient to provide for a significant decrease in the edge breakdown probability. In other words, the oxidation treatment leads to the formation of a diode with overlap between the metal junction and passivating film (Fig. 1) [1].

The breakdown voltage in such overlapped structures is significantly higher than the initial value. In the case illustrated in Fig. 1, the breakdown voltage increased up to $V_B \approx 31$ V. The remaining difference from the value anticipated according to formula (1) is explained by some other factors, the main one of which is the "microplasma" character of the breakdown. This is confirmed by observations of the prebreakdown luminescence from the metal–ZnSe junctions, which has the form of numerous bright spots randomly distributed over the entire area of the rectifying junction. This negative effect can be eliminated by special treatments of the semiconductor substrate prior to forming the rectifying junction. One such method has been patented in [8].

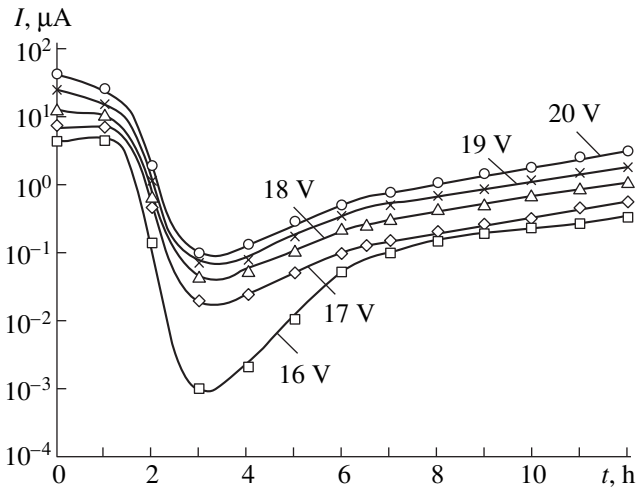

Fig. 2. Plots of the reverse current versus H_2O_2 treatment time for Ni–ZnSe junctions measured at various bias voltages.

In conclusion, it should be noted that the proposed method is principally applicable to other semiconductor compounds containing zinc. Analogous results were obtained in our experiments with metal–semiconductor junctions based on ZnTe, ZnS, and solid solutions of the ZnS_xSe_{1-x} system [9].

REFERENCES

1. S. Sze, *Physics of Semiconductor Devices* (Wiley, New York, 1981; Mir, Moscow, 1984), Vol. 1.
2. V. P. Makhniĭ and V. V. Mel'nik, Promisl. Vlasn.: Ofic. Bull., No. 5, 1995.
3. V. P. Makhniĭ and V. V. Mel'nik, Fiz. Tekh. Poluprovodn. (St. Petersburg) **29**, 1468 (1995) [Semiconductors **29**, 764 (1995)].
4. V. P. Makhniy, L. P. Galchinetskiy, and V. D. Rizikov, Proc. SPIE **904**, 617 (1999).
5. V. P. Makhniĭ, Zh. Tekh. Fiz. **68** (9), 123 (1998) [Tech. Phys. **43**, 1119 (1998)].
6. M. Yamaguchi, A. Yamamoto, and M. Roudo, J. Appl. Phys. **48**, 196 (1977).
7. L. S. Gagara, Candidate's Dissertation (Kishinev, 1986).
8. V. P. Makhniĭ and V. E. Baranyuk, USSR Inventor's Certificate No. 1835986 (1991).
9. V. P. Makhniĭ and V. V. Mel'nik, Ukr. Patent Application No. 2002119482 (November 28, 2002).

Translated by P. Pozdeev

Technical Physics Letters, Vol. 29, No. 9, 2003, pp. 714–717. Translated from Pis'ma v Zhurnal Tekhnicheskoĭ Fiziki, Vol. 29, No. 17, 2003, pp. 28–35.

The Effect of Intrinsic Charge of a Nonlinearly Oscillating Drop on the Internal Resonance Interaction of Modes

S. O. Shiryaeva

Yaroslavl State University, Yaroslavl, Russia

e-mail: shir@uniyar.ac.ru

Received March 4, 2003

Abstract—The resonance interaction of modes in a charged drop performing nonlinear capillary oscillations is weakly sensitive to changes in the intrinsic charge. This is related to a small frequency detuning of these modes in response to the charge variation in a subcritical (according to Rayleigh) region. © *2003 MAIK "Nauka/Interperiodica".*

Formulation of the problem. Investigations into the resonance interaction of modes in a nonlinearly oscillating charged drop are of interest in the context of numerous applied problems, in particular, with the study of physical mechanisms underlying the lighting discharge initiation in stormy clouds [1, 2].

Let us consider the time evolution of the shape of a drop of the ideal, incompressible, and perfectly conducting liquid with the density ρ, the surface tension γ, and the total charge Q distributed over the surface. Occurring in vacuum, the drop performs nonlinear oscillations since, at the initial time $t = 0$, the equilibrium surface of the drop (a sphere of radius R) is subject to a virtual axisymmetric perturbation of a certain finite amplitude much smaller as compared to the drop radius. As is known [3–5], the nonlinear capillary oscillations of the drop feature a resonance energy exchange between the oscillation modes, which can lead to a strong deformation of the drop surface, redistribution of the charge, and initiation of a corona discharge near the drop even for the intrinsic charge significantly below the critical level according to the Rayleigh stability criterion.

The aim of this study is to elucidate the effect of the drop charge on the laws of the resonance mode interaction.

The mathematical formulation of the problem is completely analogous to that used previously for an analysis of the nonlinear oscillations of a charged liquid drop in vacuum [3–7] and is not presented here in view of the small volume of this publication. The shape of the generating axisymmetric surface of the oscillating drop is described in the dimensionless variables such that $R = \rho = \gamma = 1$ and represented as expansion in terms of a small parameter ε characterizing the amplitude of the initial perturbation of the equilibrium spherical surface. The analytical expression describing the drop surface in a spherical coordinate system in the quadratic approximation with respect to ε can be found in the following form:

$$r(\theta, t)1 + \varepsilon\left\{\sum_{i \in \Theta} M_i^{(1)}(t)P_i(\mu)\right\} + \varepsilon^2\left\{\sum_{n=0}^{\infty} M_n^{(2)}(t)P_n(\mu)\right\} + O(\varepsilon^3), \quad (1)$$

where Θ is the spectrum of modes determining perturbation of the initial surface, $P_n(\mu)$ are the Legendre polynomials, and $\mu \equiv \cos\theta$.

Problem solution. The above problem is solved by the asymptotic multiscale method, which yields the following system of differential equations for determining the coefficients of expansion (1):

$$\frac{\partial^2 M_n^{(1)}(T_0, T_1)}{\partial T_0^2} + \omega_n^2 M_n^{(1)}(T_0, T_1) = 0; \quad (2)$$

$$\frac{\partial^2 M_n^{(2)}(T_0, T_1)}{\partial T_0^2} + \omega_n^2 M_n^{(2)}(T_0, T_1) = -2i\omega_n \frac{dA_n^{(1)}(T_1)}{dT_1}\exp[i\omega_n T_0] + \sum_{l=2}^{\infty}\sum_{m=2}^{\infty}\{[\gamma_{lmn} + \omega_l\omega_m\eta_{lmn}]A_l^{(1)}(T_1)A_m^{(1)}(T_1) \times \exp[i(\omega_l + \omega_m)T_0] + [\gamma_{lmn} - \omega_l\omega_m\eta_{lmn}]A_l^{(1)}(T_1) \times \overline{A_m^{(1)}(T_1)}\exp[i(\omega_l - \omega_m)T_0]\} + \text{c.c.}; \quad (3)$$

$$T_0 \equiv t; \quad T_1 \equiv \varepsilon t; \quad \omega_n^2 \equiv n(n-1)[(n+2) - W];$$

1063-7850/03/2909-0714$24.00 © 2003 MAIK "Nauka/Interperiodica"

$$W \equiv \frac{Q^2}{4\pi};$$

$$\gamma_{ijn} \equiv K_{ijn}\left[\omega_i^2(n-i+1) + 2n[j(j+1)-1]\right.$$

$$\left. + (j(i+1) - i(2i-2n+7) + 3)n\frac{W}{2}\right] + \alpha_{ijn}\left[\frac{1}{i}\omega_i^2 + n\frac{W}{2}\right];$$

$$\eta_{ijn} \equiv K_{ijn}\left(\frac{n}{2} - i + 1\right) + \alpha_{ijn}\frac{1}{i}\left(1 + \frac{n}{2j}\right);$$

$$K_{ijn} \equiv [C_{i0j0}^{n0}]^2; \quad \alpha_{ijn} \equiv -\sqrt{i(i+1)j(j+1)}C_{i0j0}^{n0}C_{i(-1)j1}^{n0};$$

where "c.c." denotes complex conjugate terms and a top bar indicates complex conjugation. Here, C_{i0j0}^{n0} and $C_{i(-1)j1}^{n0}$ are the Clebsch–Gordan coefficients [8], which are different from zero only when their bottom indices obey the conditions

$$|i-j| \le n \le (i+j); \quad i+j+n = 2g,$$

where g is an integer. A solution to Eqs. (2) is offered by harmonic functions with the time-dependent coefficients:

$$M_n^{(1)}(T_0, T_1) = a_n^{(1)}(T_1)\exp[ib_n^{(1)}(T_1)]\exp[i\omega_n T_0] + \text{c.c.},$$

where $a_n^{(1)}(T_1)$ and $b_n^{(1)}(T_1)$ are real function of the time T_1. The form of these functions can be determined only upon considering the problem to within the second order of smallness, that is, after solving Eq. (3).

Analysis of the solution. The form of the right-hand side of Eq. (3) shows that, when any three oscillation modes with the numbers p, q, k obey the relations $\omega_p + \omega_q = \omega_k$ or $\omega_p - \omega_q = \omega_k$, the modes enter into a resonance interaction. Let the index n indicate modes excited due to a nonlinear interaction in the second order of smallness, while k, p, and q refer to the modes coupled by the resonance interaction.

Let us analyze Eq. (3) for the modes with $n = k, p, q$ and characterize proximity of the combination of frequencies $\omega_p \pm \omega_q$ to ω_k in terms of the detuning parameter $\sigma \sim O(1)$ determined by the relation

$$\omega_p \pm \omega_q = \omega_k(1 + \varepsilon\sigma).$$

Note that the detuning parameter can be related to the drop charge (and the parameter W). This implies that, by varying the charge, it is possible to control the frequency of oscillations so as to shift this frequency from the exact resonance position.

For the sake of simplicity and brevity, let us consider the case of a degenerate resonance obeying the relation

$$\omega_k = 2\omega_p.$$

A simple analysis of the resonance interaction analogous to that performed in [5] leads to the following expressions for the time-dependent coefficients of the first order of smallness at the kth and pth modes in expansion (1):

$$\begin{aligned} M_k^{(1)}(t) &= 2a_k^{(1)}(\varepsilon t)\cos[2\omega_k t - \beta_k^{(1)}(\varepsilon t)]; \\ M_P^{(1)}(t) &= 2a_p^{(1)}(\varepsilon t)\cos[\omega_p t - b_p^{(1)}(\varepsilon t)]. \end{aligned} \quad (4)$$

Here, the real functions $a_k^{(1)}(\varepsilon t)$, $\beta_k^{(1)}(\varepsilon t)$, $a_p^{(1)}(\varepsilon t)$, and $b_p^{(1)}(\varepsilon t)$ are solutions of the following system of differential equations:

$$4\omega_k\frac{da_k^{(1)}(T_1)}{dT_1} = \Lambda_{ppk}^{(+)}[a_p^{(1)}(T_1)]^2\sin[\varphi_{kp}^{(1)}(T_1)]; \quad (5)$$

$$4\omega_k a_k^{(1)}(T_1)\frac{d\beta_k^{(1)}(T_1)}{dT_1} = 4\omega_k^2 a_k^{(1)}(T_1)\sigma + \Lambda_{ppk}^{(+)}[a_p^{(1)}(T_1)]^2\cos[\varphi_{kp}^{(1)}(T_1)];$$

$$2\omega_p\frac{da_p^{(1)}(T_1)}{dT_1} = -\Lambda_{kpp}^{(-)}a_k^{(1)}(T_1)a_p^{(1)}(T_1)\sin[\varphi_{kp}^{(1)}(T_1)];$$

$$2\omega_p a_p^{(1)}(T_1)\frac{db_p^{(1)}(T_1)}{dT_1} = -\Lambda_{kpp}^{(-)}a_k^{(1)}(T_1)a_p^{(1)}(T_1)\cos[\varphi_{kp}^{(1)}(T_1)];$$

$$\varphi_{kp}^{(1)}(T_1) = \beta_k^{(1)}(T_1) + 2b_p^{(1)}(T_1);$$

$$\Lambda_{pqk}^{(\pm)} = (\gamma_{pqk} + \gamma_{qpk}) \pm \omega_p\omega_q(\eta_{pqk} + \eta_{qpk}).$$

Figures 1a–1e illustrate the time variation of the amplitudes $M_4^{(1)}(t)$ and $M_6^{(1)}(t)$ for the fourth and sixth modes in the resonance interaction. These curves were calculated using Eqs. (4) and (5) at $\varepsilon = 0.3$ for the exact resonance $W_r = 2.66667$ and for various values of the parameter W (related to the detuning σ) different from W_r. In the initial moment, only the fourth mode was excited, and the sixth mode had a zero amplitude.

A comparison of the curves in Figs. 1a–1e shows that the nonlinear interaction of modes exhibits a resonance character for any value of the parameter $W <$

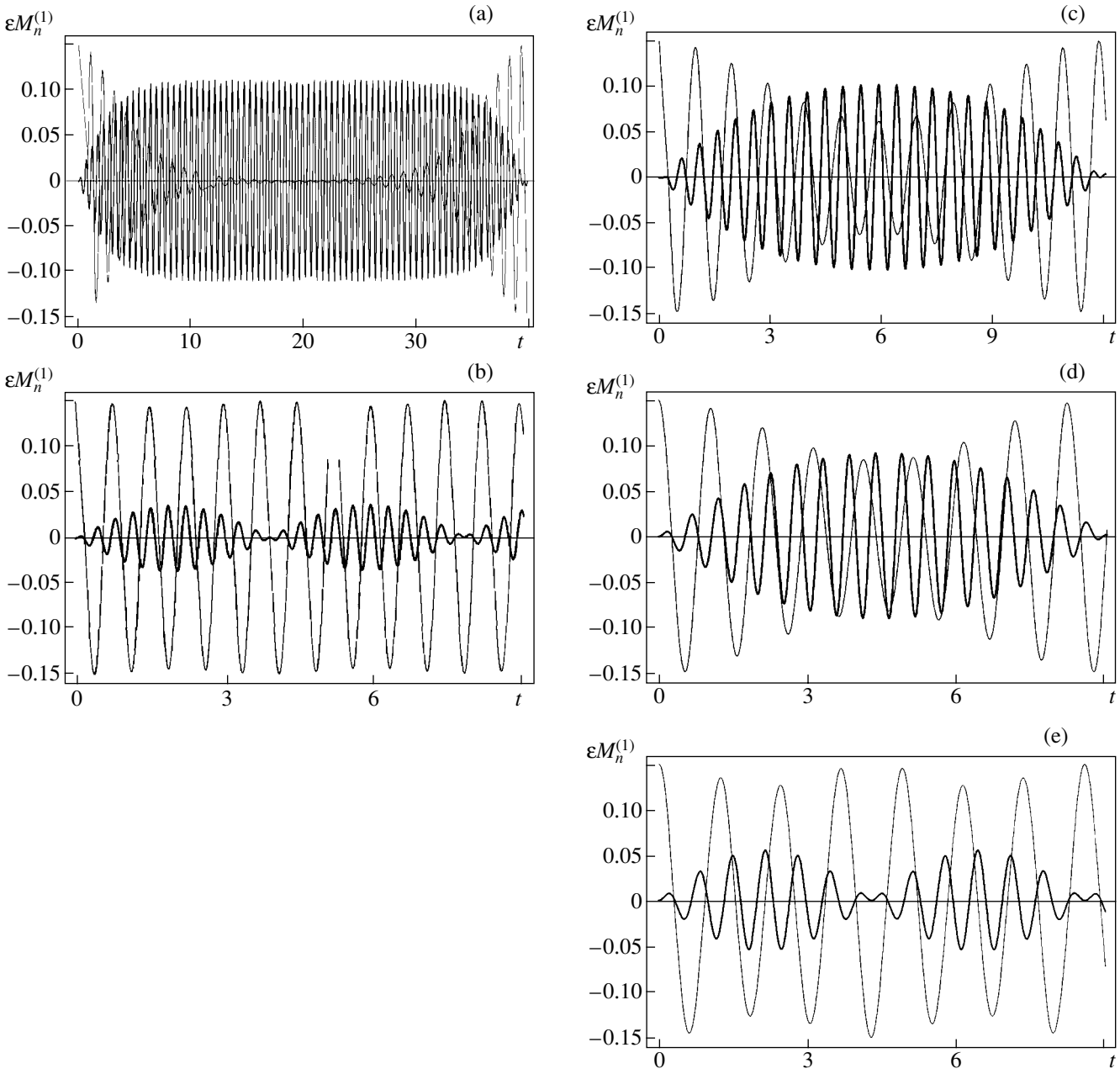

Fig. 1. Time variation of the dimensionless amplitudes of the fourth and sixth modes in exact resonance $W_r = 2.6667$ (a) and for various values of the detuning parameter $W = 0$ (b), 2.5 (c), 3 (d), and 3.9 (e). Thin solid curve represents the initially excited fourth mode, thick solid curve shows the resonance-pumped sixth mode.

$W_{cr} = 4$. This is explained by the smallness of frequency detuning for the fourth and sixth modes in response to a change in W in the interval indicated. An increase in the absolute value of the detuning parameter leads to a decrease in the characteristic time of the resonance mode interaction (determined by the time of the mode amplitude buildup to a maximum level) and in the fraction of energy transferred from the initially excited fourth mode to the resonance-excited sixth mode (complete energy pumping takes place only under the conditions of exact resonance).

Conclusions. The resonance interaction of modes in a charged drop performing nonlinear capillary oscillations is weakly sensitive to variations in the intrinsic charge. As a result, the mode resonances are determined entirely by the spectrum of modes excited at the initial time. The amplitude of resonance-pumped modes in various frequency sets depends on the detuning determined by deviations of the charge from a resonance value for the given set of frequencies.

Acknowledgments. This study was supported by Presidential Grant No. 00-15-9925.

REFERENCES

1. S. O. Shiryaeva, A. I. Grigor'ev, and D. F. Belonozhko, Pis'ma Zh. Tekh. Fiz. **29** (6), 69 (2003) [Tech. Phys. Lett. **29**, 249 (2003)].
2. A. I. Grigor'ev and S. O. Shiryaeva, Phys. Scr. **54**, 660 (1996).
3. J. A. Tsamopoulos and R. A. Brown, J. Fluid Mech. **147**, 373 (1984).
4. S. O. Shiryaeva, D. F. Belonozhko, and A. I. Grigor'ev, Pis'ma Zh. Tekh. Fiz. **28** (22), 45 (2002) [Tech. Phys. Lett. **28**, 945 (2002)].
5. S. O. Shiryaeva, Zh. Tekh. Fiz. **73** (2), 19 (2003) [Tech. Phys. **48**, 152 (2003)].
6. S. O. Shiryaeva, Zh. Tekh. Fiz. **71** (2), 27 (2001) [Tech. Phys. **46**, 158 (2001)].
7. S. O. Shiryaeva, Izv. Ross. Akad. Nauk, Mekh. Zhidk. Gaza, No. 3, 173 (2001).
8. D. A. Varshalovich, A. N. Moskalev, and V. K. Khersonskiĭ, *Quantum Theory of Angular Momentum* (Nauka, Leningrad, 1975).

Translated by P. Pozdeev

Technical Physics Letters, Vol. 29, No. 9, 2003, pp. 718–720. Translated from Pis'ma v Zhurnal Tekhnicheskoĭ Fiziki, Vol. 29, No. 17, 2003, pp. 36–40.

A Condition Imposed on the Electromagnetic Polarizability of a Bianisotropic Lossless Scatterer

P. A. Belov[a,*], S. I. Maslovski[a], K. R. Simovski[a], and S. A. Tretyakov[b,]**

[a] *Institute of Fine Mechanics and Optics (Technical University), St. Petersburg, Russia*

[b] *Helsinki University of Technology, Radio Laboratory, P.O. Box 3000, FIN-02015 HUT, Finland*

*e-mail: * belov@rain.ifmo.ru; ** stas@cc.hut.fi*

Received February 27, 2003

Abstract—In the dipole and local field approximations, electromagnetic scatterers are modeled in terms of the polarizability tensor. The matrix elements of this tensor, which are determined by the scatterer geometry, are complex even in the absence of losses in the material. There is a criterion that the polarizability tensor must obey if the scatterers possess no dissipative losses. This condition, derived here for bianisotropic scatterers, can be applied to analytical modeling of periodic structures composed of such scattering inclusions. *© 2003 MAIK "Nauka/Interperiodica".*

The field scattered from small scatterers of a complicated shape is frequently described in a dipole approximation. Within the framework of this approximation, the scatterer is replaced by a pair of dipoles, including the electric and magnetic ones, the fields of which model the scattered field. The substitution of dipoles for scatterers of a complicated geometry leads to the introduction of a polarizability operator relating the dipole moments to the local electric and magnetic fields (external with respect to the scatterer). This operator carries all information about the scatterer geometry and material. In the general case, the polarizability operator depends both on the field frequency ω and on the character of the external field distribution in the volume of scatterer.

Within the framework of the homogeneous local field approximation, the dipole moments are determined by the electric and magnetic fields (assumed constant in the scatterer volume). In this case, the polarizability operator can be replaced by a 6×6 polarizability tensor $\bar{\bar{\alpha}}$ such that

$$\begin{pmatrix} \mathbf{p} \\ \mathbf{m} \end{pmatrix} = \bar{\bar{\alpha}} \begin{pmatrix} \mathbf{E} \\ \mathbf{H} \end{pmatrix}, \tag{1}$$

where **p** and **m** are the complex amplitudes of the electric and magnetic fields; **E** and **H** are the local electric and magnetic fields acting upon the scatterer. The pairs of vectors (**p**, **m**) and (**E**, **H**) form 6-vectors obeying relation (1).

Most papers devoted to bianisotropic media (see, e.g., [1–3]) use the dyadic formalism, according to which relation (1) is represented as

$$\begin{cases} \mathbf{p} = \bar{\bar{a}}_{ee} \cdot \mathbf{E} + \bar{\bar{a}}_{em} \cdot \mathbf{H}, \\ \mathbf{m} = \bar{\bar{a}}_{me} \cdot \mathbf{E} + \bar{\bar{a}}_{mm} \cdot \mathbf{H}, \end{cases} \tag{2}$$

where $\bar{\bar{a}}_{ee}$, $\bar{\bar{a}}_{em}$, $\bar{\bar{a}}_{me}$, and $\bar{\bar{a}}_{mm}$ are three-dimensional dyads. Thus, in this formalism, the polarizability tensor is

$$\bar{\bar{\alpha}} = \begin{pmatrix} \bar{\bar{a}}_{ee} & \bar{\bar{a}}_{em} \\ \bar{\bar{a}}_{me} & \bar{\bar{a}}_{mm} \end{pmatrix}. \tag{3}$$

For an isotropic nonmagnetic scatterer, whereby $\bar{\bar{a}}_{ee} = \alpha \bar{\bar{I}}$ and $\bar{\bar{a}}_{em} = \bar{\bar{a}}_{me} = \bar{\bar{a}}_{mm} = 0$ ($\bar{\bar{I}}$ being the unity dyad), Sipe and Kranendonk [4] showed that a lossless scatterer obeys the condition

$$\mathrm{Im}\left\{\frac{1}{\alpha}\right\} = -\frac{k^3}{6\pi\varepsilon_0}, \tag{4}$$

where $k = \omega\sqrt{\varepsilon_0\mu_0}$ is the wavenumber of the isotropic medium containing the scatterer and ε_0 and μ_0 are the dielectric permittivity and the magnetic permeability of this medium, respectively. Relation (4), referred to below as the Sipe–Kranendonk condition, poses limitation on the complex quantity α by fixing the imaginary

part of the inverse quantity. The real and imaginary parts of α obey the relation

$$\mathrm{Im}\{\alpha\} = \frac{k^3}{6\pi\varepsilon_0}\sqrt{(\mathrm{Re}\{\alpha\})^2 + (\mathrm{Im}\{\alpha\})^2}. \quad (5)$$

This condition, which plays an important role in the theory of light scattering (see, e.g., [5]), was considered long ago by Planck [6] and Mandelshtam [7].

The Sipe–Kranendonk condition (4) follows from the law of energy conservation in the scatterer. This relation is very useful in the analysis of regular structures, including three-dimensional [8, 9] and two-dimensional [10–12] lattices, where it represents the condition of energy conservation in the periodic structure under consideration. It is interesting to note that the Sipe–Kranendonk condition can be derived proceeding from the law of energy conservation both in a single scatterer and in a regular structure: the results are identical. Below we will follow the former way to generalize the Sipe–Kranendonk condition (4) in the case of bianisotropic scatterers.

Let us calculate the power spent by an external field for exciting a bianisotropic scatterer:

$$P^{ext} = \frac{1}{2}\mathrm{Re}\{(j\omega\mathbf{p})^* \cdot \mathbf{E} + (j\omega\mathbf{m}) \cdot \mathbf{H}^*\}$$

$$= -\frac{\omega}{2}\mathrm{Im}\left\{\begin{pmatrix}\mathbf{p}\\ \mathbf{m}\end{pmatrix}^* \cdot \begin{pmatrix}\mathbf{E}\\ \mathbf{H}\end{pmatrix}\right\} = -\frac{\omega}{2}\mathrm{Im}\left\{\begin{pmatrix}\mathbf{p}\\ \mathbf{m}\end{pmatrix}^* \cdot \bar{\bar{\alpha}}^{-1} \cdot \begin{pmatrix}\mathbf{p}\\ \mathbf{m}\end{pmatrix}\right\} \quad (6)$$

$$= -\frac{\omega}{4j}\begin{pmatrix}\mathbf{p}\\ \mathbf{m}\end{pmatrix}^* \cdot [\bar{\bar{\alpha}}^{-1} - (\bar{\bar{\alpha}}^{-1})^\dagger]\begin{pmatrix}\mathbf{p}\\ \mathbf{m}\end{pmatrix}.$$

Here, the symbol † denotes the Hermitian conjugation operator. Note that, in a complex basis set $\{\mathbf{e}_i\}|_{i=1'}^{6}$, the Hermitian conjugation of the tensor is not equivalent to the Hermitian conjugation of the corresponding matrix and requires the basis set to be conjugated as well:

$$\bar{\bar{\alpha}} = \sum_{i=1}^{6}\sum_{j=1}^{6}\alpha_{ij}e_ie_j,$$
$$\bar{\bar{\alpha}}^\dagger \equiv \sum_{i=1}^{6}\sum_{j=1}^{6}\alpha_{ji}^*e_i^*e_j^* = \sum_{i=1}^{6}\sum_{j=1}^{6}\alpha_{ij}^\dagger e_i^*e_j^* \neq \sum_{i=1}^{6}\sum_{j=1}^{6}\alpha_{ij}^\dagger e_ie_j. \quad (7)$$

This fact is useful in considering gyrotropic scatterers [9], whereby the polarizability tensor is conveniently written in the basis set of the elliptic polarization vectors. The power radiated from the scatterer is given by the formula

$$P^{rad} = \frac{\omega^4}{12\pi c}(\mu_0\mathbf{p}^* \cdot \mathbf{p} + \varepsilon_0\mathbf{m}^* \cdot \mathbf{m})$$
$$= \frac{\omega^4}{12\pi c}\begin{pmatrix}\mathbf{p}\\ \mathbf{m}\end{pmatrix}^* \cdot \begin{pmatrix}\mu_0\bar{\bar{I}} & 0\\ 0 & \varepsilon_0\bar{\bar{I}}\end{pmatrix} \cdot \begin{pmatrix}\mathbf{p}\\ \mathbf{m}\end{pmatrix}. \quad (8)$$

If the scatterer is lossless, the external (received) (6) and radiated (8) powers are equal:

$$P^{ext} = P^{rad}. \quad (9)$$

Once the inverse tensor $\bar{\bar{\alpha}}^{-1}$ exists, it is possible to determine the electric and/or magnetic fields necessary for the excitation of any given dipole moments **p** and **m**. As a result, the generalized Sipe–Kranendonk condition (4) acquires the following form:

$$\frac{1}{2j}[\bar{\bar{\alpha}}^{-1} - (\bar{\bar{\alpha}}^{-1})^\dagger] = -\frac{k^3}{6\pi}\begin{pmatrix}\bar{\bar{I}}/\varepsilon_0 & 0\\ 0 & \bar{\bar{I}}/\mu_0\end{pmatrix}. \quad (10)$$

For reciprocal media ($\bar{\bar{a}}_{ee} = \bar{\bar{a}}_{ee}^T$, $\bar{\bar{a}}_{mm} = \bar{\bar{a}}_{mm}^T$, $\bar{\bar{a}}_{em} = -\bar{\bar{a}}_{me}^T$), this condition in the dyadic interpretation reduces to the three equivalent dyadic equations (provided that the corresponding dyads exist) [12]

$$\mathrm{Im}\{(\bar{\bar{a}}_{ee} - \bar{\bar{a}}_{em}\bar{\bar{a}}_{mm}^{-1}\bar{\bar{a}}_{me})^{-1}\} = \frac{k^3}{6\pi\varepsilon_0}\bar{\bar{I}}, \quad (11)$$

$$\mathrm{Im}\{(\bar{\bar{a}}_{mm} - \bar{\bar{a}}_{me}\bar{\bar{a}}_{ee}^{-1}\bar{\bar{a}}_{em})^{-1}\} = \frac{k^3}{6\pi\varepsilon_0}\bar{\bar{I}}, \quad (12)$$

$$\mathrm{Re}\{(\bar{\bar{a}}_{ee} - \bar{\bar{a}}_{em}\bar{\bar{a}}_{mm}^{-1}\bar{\bar{a}}_{me})^{-1}\bar{\bar{a}}_{em}\bar{\bar{a}}_{mm}^{-1}\} = 0. \quad (13)$$

Should the scatterer not to possess bianisotropic properties ($\bar{\bar{a}}_{em} = \bar{\bar{a}}_{me} = 0$), Eq. (10) separates into two independent conditions:

$$\mathrm{Im}\{\bar{\bar{a}}_{ee}^{-1}\} = -\frac{k^3}{6\pi\varepsilon_0}\bar{\bar{I}},$$
$$\mathrm{Im}\{\bar{\bar{a}}_{mm}^{-1}\} = -\frac{k^3}{6\pi\varepsilon_0}\bar{\bar{I}}. \quad (14)$$

To summarize, we have presented derivation of the generalized Sipe–Kranendonk condition for lossless bianisotropic scatterers. this condition follows from the energy conservation law for a single scatterer and is

very useful in the analysis of energy balance in regular structures containing numerous scatterers [8–12].

REFERENCES

1. S. A. Tretyakov, F. Mariotte, C. R. Simovski, *et al.*, IEEE Trans. Antennas Propag. **44**, 1006 (1996).
2. C. R. Simovski, S. A. Tretyakov, A. A. Sochava, *et al.*, J. Electromagn. Waves Appl. **11**, 1509 (1997).
3. C. R. Simovski, M. S. Kondratjev, P. A. Belov, *et al.*, IEEE Trans. Antennas Propag. **47**, 1429 (1999).
4. J. E. Sipe and J. van Kranendonk, Phys. Rev. A **9**, 1806 (1974).
5. I. I. Sobel'man, Usp. Fiz. Nauk **172** (1), 85 (2002).
6. M. Planck, Sitzungsber. K. Preuss. Akad. Wiss. **24**, 470 (1902).
7. L. I. Mandelshtam, *Complete Collection of Works* (Akad. Nauk SSSR, Moscow, 1948), Vol. 1.
8. S. A. Tretyakov and A. J. Viitanen, J. Opt. Soc. Am. A **17**, 1791 (2000).
9. P. A. Belov, S. A. Tretyakov, and A. J. Viitanen, Phys. Rev. E **66**, 016608 (2002).
10. S. A. Tretyakov and A. J. Viitanen, J. Electromagn. Waves Appl. **14**, 1159 (2000).
11. P. A. Belov and S. A. Tretyakov, J. Electromagn. Waves Appl. **16**, 129 (2002).
12. V. V. Yatsenko, S. I. Maslovski, S. A. Tretyakov, *et al.*, IEEE Trans. Antennas Propag. **51**, 2 (2003).

Translated by P. Pozdeev

Technical Physics Letters, Vol. 29, No. 9, 2003, pp. 721–724. Translated from Pis'ma v Zhurnal Tekhnicheskoĭ Fiziki, Vol. 29, No. 17, 2003, pp. 41–48.

Temperature Variation of the Morphology of Nanocluster Ensembles in the Ge/Si(100) System

V. G. Dubrovskiĭ[a], V. M. Ustinov[a], A. A. Tonkikh[a], V. A. Egorov[a], G. E. Cirlin[b], and P. Werner[c]

[a] *Institute of Analytical Instrument Building, Russian Academy of Sciences, St. Petersburg, Russia*
[b] *Ioffe Physicotechnical Institute, Russian Academy of Sciences, St. Petersburg, 194021 Russia*
[c] *Max Planck Institut für Mikrostrukturphysik, Halle, Germany*

Revised manuscript received February 18, 2003

Abstract—The morphological characteristics of hut-cluster ensembles formed in a Ge/Si(100) heteroepitaxial system have been studied as functions of the substrate surface temperature by theoretical methods and by atomic force microscopy. As the temperature increases from 420 to 500°C, the lateral size of nanoclusters with a square base (grown at the same rate of 0.0345 ML/s to a total coverage of 6.2 ML) grows from 12 to 20 nm, while their number density on the substrate surface drops from 5.6×10^{10} to 1.5×10^{10} cm^{-2}. Predictions of a kinetic model are in sufficiently good agreement with the experimental data. © *2003 MAIK "Nauka/Interperiodica".*

Introduction. Processes involved in the formation of ensembles of coherent islands in heteroepitaxial semiconductor structures are of considerable interest from the standpoint of both basic science and practical applications related to the obtaining of high-density quantum dot (QD) arrays [1]. Spatial confinement of the charge carriers in three directions results in the atomic-like spectrum of energy states of QDs, which makes these systems promising objects for optoelectronics. Because of such dimensional quantization effects, the working wavelengths of light-emitting devices with active regions based on the QD heterostructures depend on the lateral size of islands, while the emission intensity depends on the number density of islands on the substrate surface. This circumstance accounts for the importance of studying the effect of controllable technological parameters on the morphology of QD ensembles [2].

In this context, we have studied the dependence of the lateral size and surface density of QDs on the substrate temperature in the initial growth stage. The experiments were performed with model Ge/Si(100) heterostructures, which represent a promising system for the development of silicon-based optoelectronic devices [3].

Theoretical model. A kinetic model describing the formation of coherent islands in the initial growth stage [4, 5] gives the following qualitative pattern of the process. A two-dimensional surface is stable when the wetting layer thickness is smaller than the equilibrium thickness determined according to the Müller–Kern criterion [6]: $h_{eq} = k_0 \ln[\Phi/h_0(1 - z(\theta))\lambda\varepsilon_0^2]$. Here, k_0 is the coefficient of relaxation of the adhesion to substrate, Φ is the wetting energy density on the substrate surface, $z(\theta)$ is the relative elastic energy relaxation in the island as a function of the contact angle θ [7], λ is the elastic modulus of the deposit, and ε_0 is the lattice mismatch. The maximum rate of island nucleation is observed for a critical wetting layer thickness of $h_c = (1 + \zeta_*)h_{eq}$ at the time $t_* = \zeta_* t_{eq}$, where $t_{eq} = h_{eq}/V$ is the time required for the growth of an equilibrium wetting layer, V is the growth rate expressed in monolayers per second (ML/s), and $\zeta_* = 0.24A^{3/2}/B(\ln Q)^{1/2}$ is a parameter corresponding to the maximum degree of metastability. Here, the constants $A \equiv [\sigma(\theta)/\cos\theta - \sigma(0)]\alpha^2(\theta)l_0^2/k_BT$ and $B \equiv (h_{eq}/k_0)[1 - z(\theta)]\lambda\varepsilon_0^2 h_0 l_0^2/k_BT$ are determined by the ratios of the additional surface energy of an island and the difference of elastic energies in the island and wetting layer, respectively, to the thermal energy; $\sigma(\theta)$ and $\sigma(0)$ are the surface energy densities on the island side face and the substrate surface, respectively; l_0 is the distance between atoms on the surface; T is the surface temperature, $\alpha(\theta) \equiv (6h_0\cot\theta/l_0)^{1/3}$ is the geometric factor, and h_0 is the monolayer height.

If the principal mechanism of island growth is via diffusion of a material from wetting layer to islands [4, 5], the control parameter is $Q = t_{eq}/\tau$, where $\tau = 3l_0^2/8\alpha B\nu D(T)$, $D(T)$ is the temperature-dependent coefficient of volume diffusion in the wetting layer and ν is the parameter of truncation of the elastic force potential. The temperature dependence of the diffusion coefficient can be approximated by the Arrhenius law, $D(T) = D_0\exp(-T_D/T)$, where T_D is the characteristic diffusion temperature. The above expressions refer to

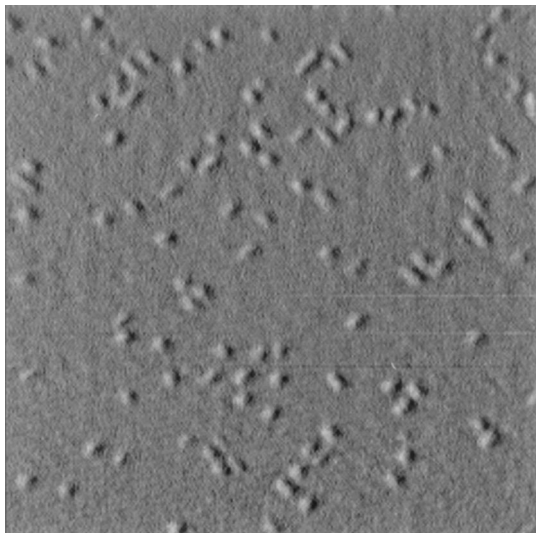

Fig. 1. AFM image of the surface of a sample obtained at 450°C (scanned area, 500 × 500 nm; the image sides are parallel to the crystallographic directions [011] and [$0\bar{1}1$]).

islands of a square pyramidal shape with a base side length L and the height to lateral size ratio $\beta = \tan\theta/2$.

The island nucleation is virtually complete by the time $t = t_* + \Delta t$, where $\Delta t = (0.57/\ln Q)t_*$ is the duration of the nucleation stage. The nucleation stage is followed by the stage of island size relaxation, whereby the number density of islands on the surface remains constant, while the relative average island size l increases according to the relation

$$\frac{t - t_*}{t_R} = \ln\left[\frac{(1 + l + l^2)^{1/2}}{1 - l}\right] - \sqrt{3}\arctan\left(\frac{2l + 1}{\sqrt{3}}\right) + \frac{\pi}{2\sqrt{3}}, \quad t_* \le t \le 3t_R. \tag{1}$$

Here, $l(t) = L(t)/L_R$, $L(t)$ is the average lateral island size, and L_R is the average lateral size at the end of the relaxation stage. The latter value is given by the formula

$$L_R = 0.2\alpha l_0 \frac{A^{3/2}}{B}\frac{Q^{1/2}}{(\ln Q)^{2/3}}. \tag{2}$$

A characteristic duration of the island size relaxation stage is $t_R = [0.47/(\ln Q)^{1/3}]t_*$. The number density of islands on the surface upon the nucleation stage is

$$N = \frac{30}{l_0^2}h_{eq}\frac{B^2}{A^3}\frac{(\ln Q)^{3/2}}{Q^{3/2}}. \tag{3}$$

The above formulas are valid under the condition that $F = (5.2)\ln Q \gg 1$, which ensures the applicability of a macroscopic description of the nucleation process and implies the time hierarchy $\Delta t \ll t_R \ll t_*$ [4]. The large parameter F of the theory represents the activation barrier for nucleation at a maximum wetting layer thickness [4, 5]. In all equations, the time is measured from the moment when the wetting layer thickness attains the equilibrium value h_{eq}.

Experimental. The experiments were performed on a molecular beam epitaxy (MBE) system of the SIVA type (Riber, France). The nanoclusters of Ge/Si(100) were grown at various substrate temperatures T = 420 (*1*), 450 (*2*), 470 (*3*), and 500°C (*4*). The MBE growth techniques and the methods of sample structure characterization were described in detail elsewhere [3]. The growth rate of germanium nanoclusters in all experiments was 0.0345 ML/s. The time of growth termination corresponded to the deposition of a total amount of germanium equivalent to 6.2 ML. For the growth rate indicated above, the deposition time was 180 s. The sample surface morphology was studied by atomic force microscopy (AFM) using a setup of the Digital Instruments Inc. (USA).

Results and discussion. Figure 1 shows a typical AFM image of the sample surface. An analysis of such patterns showed that the nanoclusters grown at 420°C have the shape of a pyramid with an approximately square base. When the substrate temperature was increased, the AFM images revealed the presence of clusters of the two kinds, with square and rectangular bases, the latter being elongated in the x axis direction (the x and y axes are directed along [010] and [001], respectively). The L_x/L_y ratio in elongated clusters varied from 1.74 to 2.64. In samples of all four types, the fraction of clusters with square bases was dominating. The contact angle increased with the growth temperature. The average size of clusters of both kinds grown to 6.2 ML exhibited a significant increase with the temperature. The experimental values of the average lateral size and the number density of nanoclusters determined from the AFM data are presented in Table 1. The error of cluster size determination did not exceed 5%.

Theoretical calculations for the clusters with square bases grown at four temperatures were performed with the following values of parameters: $\lambda = 1.27 \times 10^{12}$ dyn/cm^2; $\varepsilon_0 = 0.042$, $h_0 = 0.145$ nm; $l_0 = 0.395$ nm; $\Phi = 450$ erg/cm^2; $\sigma(0) = 800$ erg/cm^2; $\sigma(\theta) = 830$ erg/cm^2; $k_0 = 0.68$; $\nu = 10$; $T_D = 5000$ K; and $D(T = 470°C) = 1.8 \times 10^{-13}$ cm^2/s. The contact angle at each temperature was determined as the ratio of the measured value of the island height to lateral size. The values of $z(\theta)$ were calculated using data from [7]. The average size of nanoclusters was calculated using expressions (1) and (2) for the time moment corresponding to the deposition of 6.2 ML of germanium. The number density of islands on the surface was cal-

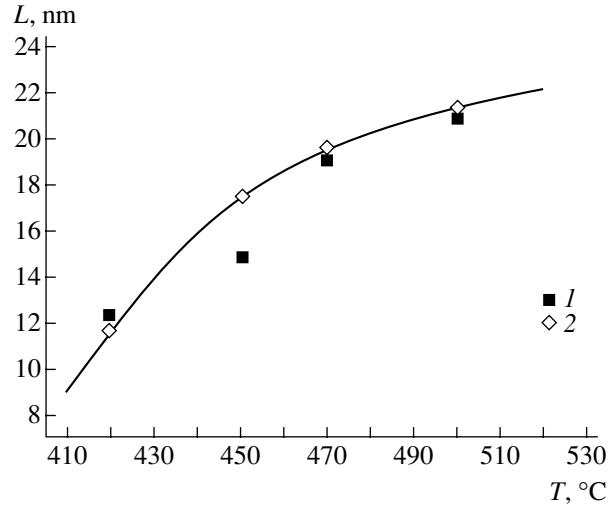

Fig. 2. Experimental (*1*) and theoretical (*2*) plots of the average lateral size of Ge/Si(100) nanoclusters versus substrate temperature.

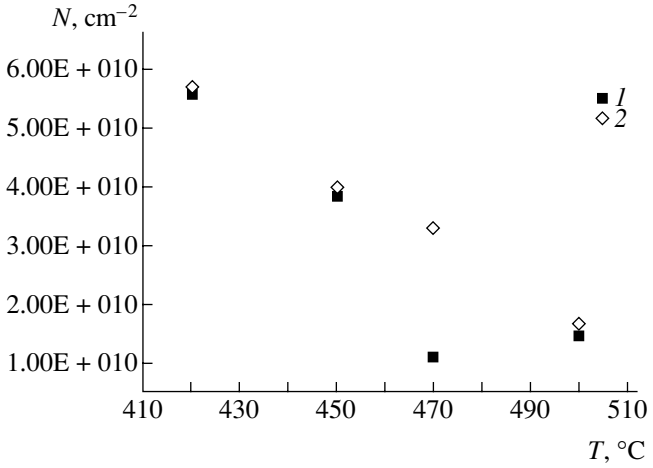

Fig. 3. Experimental (*1*) and theoretical (*2*) plots of the number density of Ge/Si(100) nanoclusters versus substrate temperature.

culated by formula (3). The results of theoretical calculations of the main process characteristics are summarized in Table 2.

The experimental and theoretical values of the average lateral size and number density of Ge/Si(100) clusters are compared in Figs. 2 and 3. As can be seen, the measured and calculated values virtually coincide for three temperatures (T = 420, 470, and 500°C for the average lateral size and T = 420, 470, and 500°C for the island number density). The experimental points for the average island size at 450°C and the island number density at 470°C somewhat fall out of the monotonic dependences. This can be related to the presence of a significant fraction of elongated islands and/or to insufficient area scanned during the AFM measurements.

To summarize, the results of our investigation show that the average lateral size of Ge/Si(100) nanoclusters increases and their number density decreases with increasing substrate temperature. The process of nanocluster formation has a substantially kinetic character in the initial growth stage. Predictions of the kinetic model adopted agree quite well with the experimental data. These results open the way to the obtaining of Ge/Si(100) nanostructures with the parameters con-

Table 1. Experimental values of the parameters of Ge/Si(100) nanoclusters determined using atomic force microscopy

Sample	T, °C	Number density of clusters, 10^{10} cm^{-2}	Island height, nm	Lateral size, nm			
				Square clusters		Rectangular clusters	
				L_x	L_y	L_x	L_y
1	420	5.6	1.3	11.8	13.0	–	–
2	450	3.9	2.5	14.2	15.3	24.7	11.8
3	470	1.1	3.0	20.2	17.9	33.1	19.0
4	500	1.5	5.0	20.2	21.3	53.1	20.1

Table 2. Calculated characteristics of the process of Ge/Si(100) nanocluster formation

T, °C	θ, deg	h_{eq}, ML	h_c, ML	t_{eq}, s	t_*, s	t_0, s	Δt, s	t_R, s	F	L_R, nm	L_0, nm	N, cm^{-2}
420	13	2.7	5.7	77	95	103	7.1	23	19	25	11.7	5.7×10^{10}
450	19	2.6	5.5	74	90	106	6.5	21	20	26	17.5	4.0×10^{10}
470	18	2.4	5.5	74	90	106	6.2	21	20	28	19.6	3.3×10^{10}
500	26	2.4	5.5	69	94	111	6.4	22	21	31	21.3	1.7×10^{10}

Note: the cluster size $L_0 = L(t_0)$ and the time t_0 correspond to 6.2 ML of the material deposited onto substrate.

trolled by selecting the substrate temperature during MBE growth.

Acknowledgments. This study was supported in part by the Research Programs of the Ministry of Industry, Science, and Technology of the Russian Federation.

One of the authors (G.E.C.) is grateful to the Alexander von Humboldt Stiftung.

REFERENCES

1. D. Bimberg, M. Grundmann, and N. N. Ledentsov, *Quantum Dot Heterostructures* (Wiley, Chichester, 1998).
2. O. P. Pchelyakov, Yu. B. Bolkhovityanov, A. V. Dvurechenskiĭ, *et al.*, Fiz. Tekh. Poluprovodn. (St. Petersburg) **34**, 1281 (2000) [Semiconductors **34**, 1229 (2000)].
3. G. E. Cirlin, V. A. Egorov, L. V. Sokolov, and P. Werner, Fiz. Tekh. Poluprovodn. (St. Petersburg) **36**, 1379 (2002) [Semiconductors **36**, 1294 (2002)].
4. V. G. Dubrovskii, G. E. Cirlin, and V. M. Ustinov, Phys. Rev. B (in press).
5. S. A. Kukushkin, A. V. Osipov, F. Shmidt, and P. Hess, Fiz. Tekh. Poluprovodn. (St. Petersburg) **36**, 1177 (2002) [Semiconductors **36**, 1097 (2002)].
6. P. Müller and R. Kern, Appl. Surf. Sci. **102**, 6 (1996).
7. C. Ratsch and A. Zangwill, Surf. Sci. **293**, 123 (1993).

Translated by P. Pozdeev

Technical Physics Letters, Vol. 29, No. 9, 2003, pp. 725–727. Translated from Pis'ma v Zhurnal Tekhnicheskoĭ Fiziki, Vol. 29, No. 17, 2003, pp. 49–54.

Near Ultraviolet Diagnostics of Oxide Layers in Si–SiO_2 Structures

A. Yu. Askinazi, A. P. Baraban, and L. V. Miloglyadova

Institute of Physics, St. Petersburg State University, St. Petersburg, Russia

Received March 17, 2003

Abstract—We propose a method for the rapid diagnostics of Si–SiO_2 structures based on the measurement of high-frequency capacitance–voltage characteristics in an electrolyte–insulator–semiconductor system upon preliminary irradiation of the samples in the near UV spectral range. © *2003 MAIK "Nauka/Interperiodica".*

At present, there is a wide class of semiconductor devices based on Si–SiO_2 structures in which the silicon oxide layer plays an active role. At the same time, some factors (such as ion implantation and external field application) may change the charged state of the oxide layer in these structures either during fabrication or in the course of subsequent operation. For this reason, studying the nature and properties of electrically active centers formed in these structures under the action of various external factors is of considerable importance. In this context, development of fast and nondestructive methods for the diagnostics of Si–SiO_2 structures is of interest for both basic science and technological applications. From this standpoint, a valuable method is offered by the measurement of high-frequency capacitance–voltage characteristics of the samples in an electrolyte–insulator–semiconductor system [1] in combination with irradiation of the samples in the near UV spectral range. This method provides, on the one hand, additional information about the presence, nature, and properties of the electrically active centers in SiO_2 and, on the other hand, reveals conditions under which the Si–SiO_2 structures are most sensitive with respect to near UV radiation. This latter is of considerable interest for the development of near UV radiation sensors.

The purpose of this study was to assess the possibilities of rapid diagnostics of the properties of electrically active centers formed in the SiO_2 layer of Si–SiO_2 structures as a result of irradiation in the near UV spectral range.

The experiments were performed with Si–SiO_2 structures possessing significantly different physical properties, which were prepared by various methods: (i) thermal oxidation of KDB-10 (or KDB-100) grade silicon wafers in water vapor at 950°C (oxide layer thickness, 60 nm); (ii) implantation of 190-keV oxygen ions to a dose of 1.8×10^{18} cm^{-2} into silicon substrates at 650°C, followed by annealing for 6 h at $T = 1320$°C and etching of the uppermost damaged layer (this process, known as SIMOX technology, leads to the formation of an approximately 450-nm-thick SiO_2 layer), and (iii) thermal oxidation of KDB-10 (or KDB-100) grade silicon wafers in a wet oxygen atmosphere at 950°C (oxide layer thickness, 90 nm), followed by 43-keV argon ion implantation to a dose of 10^{12}–10^{14} cm^{-2} and rapid thermal annealing at 450°C.

The sample structures were irradiated in the near UV range (4–6 eV) using the light of a DRL-250 mercury lamp. The electric field action (with plus on Si) was studied in an electrolyte–insulator–semiconductor system [1] at voltages not producing destructive breakdown of the oxide layer in the samples studied. All the measurements were performed at a temperature of 293 K.

Structures of the first type exhibited insignificant initial effective positive charge (~10^{11} cm^{-2}), the density of which could be modified by the electric field application in the electrolyte–insulator–semiconductor system [1, 2]. As demonstrated previously [1, 2], the charge state of the oxide layer upon the electric field action depends both on the electric field strength in this layer and on the treatment duration. The range of electric fields can be conditionally divided into four regions ($E1 < E2 < E3 < E4$ in the notation of [2], see Fig. 1). In this study, special attention was given to the field action in the $E3$ region (which leads to the formation of positively charged electrically active centers at the Si–SiO_2 interface [2]) and in the $E4$ region (where the impact ionization process develops in the oxide layer volume, leading to a complicated distribution of charged centers in this layer [2]) (Fig. 1).

As noted above, a field action in the $E3$ region led to a significant increase in the effective positive charge of the Si–SiO_2 structures (Fig. 1) [2]. Subsequent near UV irradiation of such samples led to virtually complete neutralization of this charge. However, repeated field action in the $E3$ region increased the sample charge again to a level approximately equal to that upon the first action (Fig. 1).

1063-7850/03/2909-0725$24.00

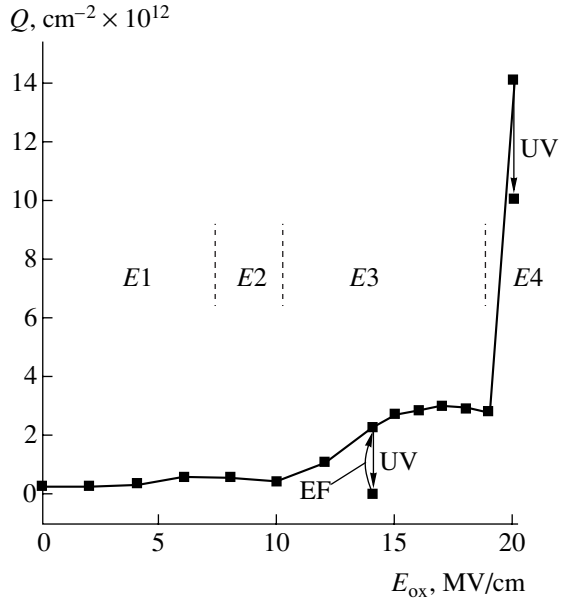

Fig. 1. Plots of the total effective charge density Q versus electric field strength E_{ox} in the oxide layer of Si–SiO_2 structures (UV is the effect of near UV irradiation; EF is the result of the electric field action in the electrolyte–insulator–semiconductor system).

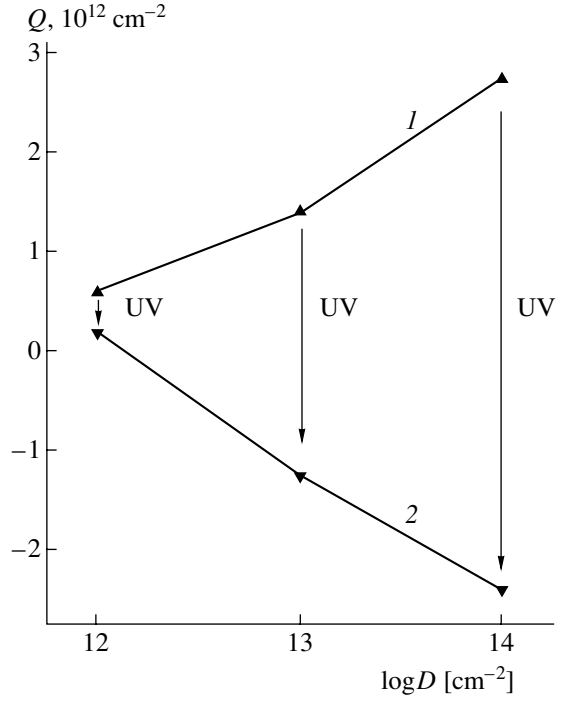

Fig. 2. Plots of the effective charge density Q versus implantation dose D in structures of the third type after (*1*) implantation and (*2*) subsequent near UV irradiation.

A field action in the $E4$ region more significantly increased the effective positive charge of the oxide layer in Si–SiO_2 structures of the first type (Fig. 1) [2]. However, in this case, subsequent near UV irradiation of the samples decreased the charge only by a value comparable with the charge formed under the field action in the $E3$ region (Fig. 1).

The samples of Si–SiO_2 structures of the second type initially possessed a considerable effective positive charge [3, 4], which was still increased under the field action. Subsequent near UV irradiation led to virtually complete neutralization of this charge both before and after the field action [3].

In Si–SiO_2 structures of the third type, ion implantation led to the appearance of an effective positive charge with a magnitude proportional to the total ion dose [5]. Here, the near UV irradiation of the on-implanted structures led to the formation of a considerable effective negative charge comparable in magnitude with the positive charge produced by the ion implantation (Fig. 2) [5].

In all the aforementioned cases, the sample recharge caused by the near UV irradiation is related to the photoinjection of electrons from a silicon substrate into the SiO_2 layer and their transport in a Coulomb field of the positively charged electrically active centers. This is confirmed by a spectral threshold of the irradiation-induced recharge of the electrically active centers. This threshold (about 4.3 eV) corresponds to the potential barrier height for electrons at the Si–SiO_2 interface. Another piece of evidence is the absence of the irradiation-induced recharge in Si–SiO_2 structures upon application of an electric field suppressing the photocurrent.

However, various Si–SiO_2 structures exhibited different response to the near UV irradiation. We have concluded that, in structures of the first type, a field action in the $E4$ region leads to the formation of additional electrically active centers in the oxide region, which are different from the positively charged centers formed in the $E3$ region: the former centers are not recharged under the near UV irradiation. For structures of the second type, we conclude that the electrically active centers responsible for the positive charging of SIMOX structures and those responsible for the charge induced by the field action are of a like nature, possessing two states: positively charged and neutral. In structures of the third type, ion implantation leads to the formation of positively charged amphoteric centers, which are recharged under near UV irradiation to a negative state.

Thus, irradiation of the Si–SiO_2 structures in the near UV spectral range leads to different consequences depending on the sample pretreatment, which provides information about the properties of electrically active centers formed in the volume of oxide layer. Structures of the third type are most sensitive with respect to near UV radiation.

Acknowledgments. This study was supported by the Ministry of Defense of the Russian Federation (project no. PD02-1.2-356).

REFERENCES

1. A. P. Baraban, V. V. Bulavinov, and P. P. Konorov, *Electronics of SiO_2 Layers on Silicon* (Leningr. Gos. Univ., Leningrad, 1988).
2. A. P. Baraban, V. V. Bulavinov, and A. G. Troshikhin, Pis'ma Zh. Tekh. Fiz. **19** (18), 27 (1993) [Tech. Phys. Lett. **19**, 577 (1993)].
3. A. Yu. Askinazi, A. P. Baraban, V. A. Dmitriev, *et al.*, Pis'ma Zh. Tekh. Fiz. **27** (10), 57 (2001) [Tech. Phys. Lett. **27**, 422 (2001)].
4. A. Yu. Askinazi, A. P. Baraban, and L. V. Miloglyadova, Zh. Tekh. Fiz. **72** (5), 61 (2002) [Tech. Phys. **47**, 574 (2002)].
5. A. P. Baraban and L. V. Malyavka, Pis'ma Zh. Tekh. Fiz. **26** (4), 53 (2000) [Tech. Phys. Lett. **26**, 159 (2000)].

Translated by P. Pozdeev

Technical Physics Letters, Vol. 29, No. 9, 2003, pp. 728–731. Translated from Pis'ma v Zhurnal Tekhnicheskoĭ Fiziki, Vol. 29, No. 17, 2003, pp. 55–61.

Ensuring Stable Operation of Ferroelectric Microwave Devices in a Broad Temperature Range

S. P. Zubko* and A. Kh. Kurbanov

St. Petersburg State Electrotechnical University, St. Petersburg, Russia

** e-mail: SPZubko@mail.eltech.ru*

Received March 19, 2003

Abstract—Several approaches to ensuring stable operation of controlled ferroelectric microwave devices in a broad temperature range are considered. A new method is proposed for electrical compensation of the temperature dependence of the parameters of ferroelectric devices. © *2003 MAIK "Nauka/Interperiodica".*

One of the main properties of ferroelectrics is a strong dependence of their dielectric characteristics on the temperature. For this reason, an important problem always encountered in the development of control devices based of ferroelectric materials is related to ensuring their stable operation in a broad temperature range. For example, phase shifters used in phased-array antennas for radars and anticollision systems on board moving vehicles have to provide stable control of the signal phase in a temperature range from –60°C to +60°C.

There are several possible approaches to ensuring stable operation of ferroelectric devices in a broad temperature range. The simplest method consists in placing a given device inside a thermostatted case where a constant temperature is maintained independently of the ambient temperature. The temperature stabilization can also be provided by developing adjustable devices with posistors [1], representing thermoresistors with a positive temperature coefficient of resistance. Posistors are based on barium titanate with micrtoadditives of rare earth elements. However, the behavior of such materials depends not only on the temperature, but on the applied voltage as well. A general disadvantage of these approaches to temperature control is a relatively large time required for the system to attain the operation regime.

Another approach can be referred to as technological. This approach is based on the use of ferroelectric $Ba_xSr_{1-x}TiO_3$ (BST) films with nonuniform distribution of barium across the film thickness. Such films can be considered as multilayer structures comprising several ferroelectric layers with different barium content x. Since the BST phase transition temperature depends on the barium content, various layers possess different temperatures of the transition to a ferroelectric state. As a result, the temperature dependence of the overall permittivity of such a multilayer film exhibits a virtually flat maximum in a sufficiently broad temperature interval [2, 3]. However, in this case, there arises a problem of providing technological reproducibility of such multilayer films.

We believe that the most expedient solution is offered by the method of electrical compensation, whereby the temperature dependence of the dielectric permittivity is compensated by applying a temperature-dependent control voltage to the ferroelectric layer [4, 5].

Electrical Compensation of the Temperature Dependence of Capacitance of a Ferroelectric Capacitor

Model representation of the control voltage as a function of the temperature. The permittivity of ferroelectrics of the displacement type (such as BST) depends on the temperature as described by the relations [6, 7]

$$\varepsilon_f(E, T, x) = \varepsilon_{00}(x)/\Phi(E, T, x), \tag{1}$$

$$\begin{aligned}\Phi(E, T, x) = {} & [(\xi(E, x)^2 + \eta(T, x)^3)^{1/2} + \xi(E, x)]^{2/3} \\ & + [(\xi(E, x)^2 + \eta(T, x)^3)^{1/2} - \xi(E, x)]^{2/3} - \eta(T, x),\end{aligned} \tag{2}$$

$$\begin{aligned}\xi(E, x) &= \sqrt{\left(\frac{E}{E_N(x)}\right)^2 + \left(\xi_s\frac{E_N(0)}{E_N(x)}\right)^2}, \\ \eta(T, x) &= \frac{T}{T_C(x)} - 1,\end{aligned} \tag{3}$$

where ξ_s is a parameter characterizing the crystallographic quality of the ferroelectrics, E_N is the normalizing field (characterizing nonlinearity of the material), $\varepsilon_{00} = C_w/T_C$, C_w is the Curie–Weiss constant, and T_C is the Curie temperature. Dependence of the model parameters on the barium content x was considered in detail elsewhere [7, 8].

Equating the right-hand side of relation (1) to a certain permittivity ε_g required for the device operation,

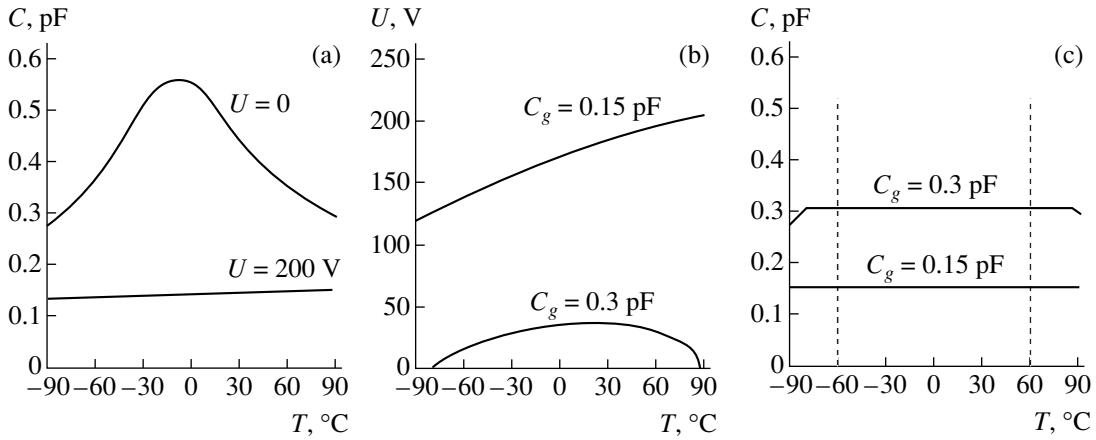

Fig. 1. Temperature dependence of the parameters of a planar ferroelectric capacitor based on a $Ba_{0.5}Sr_{0.5}TiO_3$ film: (a) capacitance at two different control voltages ($\xi_s = 0.6$); (b) temperature-dependent control voltage corresponding to two preset values of the capacitance; (c) capacitance controlled by a temperature-dependent voltage determined according to Eqs. (4)–(6).

we can derive the temperature dependence of the control field strength:

$$E(T, \varepsilon_g) = \sqrt{\left(\frac{\varepsilon_{00}(x)}{\varepsilon_g} - \eta(T, x)\right)\left(\frac{\varepsilon_{00}(x)}{2\varepsilon_g} + \eta(T, x)\right)^2 E_N^2(x) - \xi_s^2 E_N^2(0)}. \quad (4)$$

Using the methods of partial capacitance and conform mapping, the permittivity of the ferroelectrics can be recalculated to the capacitance of an effective planar capacitor (Fig. 1a) [9]:

$$C(U, T, x) = w\varepsilon_0\left[\frac{\varepsilon_f(U, T, x) - \varepsilon_s - 1}{s/h + 4\ln(2)/\pi} + \frac{2}{\pi}\ln\left(4\frac{L}{s}\right) + (\varepsilon_s - 1)\frac{1}{\pi}\ln\left(\frac{16H}{\pi s}\right)\right], \quad (5)$$

where s is the planar capacitor gap width, h is the ferroelectric film thickness, L is the electrode length, H is the substrate thickness, w is the capacitor width [9], and ε_s is the permittivity of the substrate.

The relation between the control field strength and applied voltage in the planar capacitor is as follows [10]:

$$U(T, C_g) = E(T, C_g)(s + h). \quad (6)$$

In formula (6) (unlike expression (4)), the bias field strength is considered as a function of the temperature and the capacitance C_g because the permittivity is determined proceeding from the capacitance (required for the device operation) using expression (5) relating the capacitance and permittivity of a planar capacitor (including a substrate with the ferroelectric film). The form of the $U(T, C_g)$ function is shown in Fig. 1b.

As can be seen from Fig. 1c, application of a temperature-dependent control voltage according to (4)–(6) to the ferroelectric capacitor makes the system independent of the temperature in a rather broad interval.

Electrical thermocompensation. In order to provide for the required electrical thermocompensation, the bias voltage is applied to the adjustable ferroelectric capacitor via a correction circuit. The bias voltage correction in response to variation of the capacitor parameters with the temperature and other external factors can be performed in either the analog or the digital regime. Figure 2 shows a schematic diagram of the discrete voltage correction module comprising a controlled power supply source (*PS*), analog-to-digital converters (ADCs) of the voltage and temperature (Λ_U/# and Λ_T/#, respectively), decoders of the voltage and temperature signals (SW_U and SW_T, respectively), digital-to- analog (DAC) converter (#/Λ), comparator (*CM*), ferroelectric capacitor (C_f), and temperature sensor (*TS*).

In this control unit, the voltage is corrected through multiplying it by the correction coefficient $K_{U,T}$ (*CC*) determined proceeding from the required values of the control voltage and the temperature. The coefficients $K_{U,T}$ (*CC*) are determined by formula

$$K_{U,T} = \frac{U(T, C_g)}{U_c}, \quad (7)$$

where $U_c = U(T_0, C_g)$ at $T_0 = 20$°C, and represented in the form of a discrete matrix (Fig. 2).

The current values of the voltage U_c and the temperature signals $U(T)$ are selected by two ADCs. The current temperature is measured by an external temperature sensor mounted in the same case as the controlled device. These signals, processed by decoders, select the column and row to determine the *CC* value by which the current value of U_c has to be multiplied at a given temperature. The *CC* signal is converted by DAC into

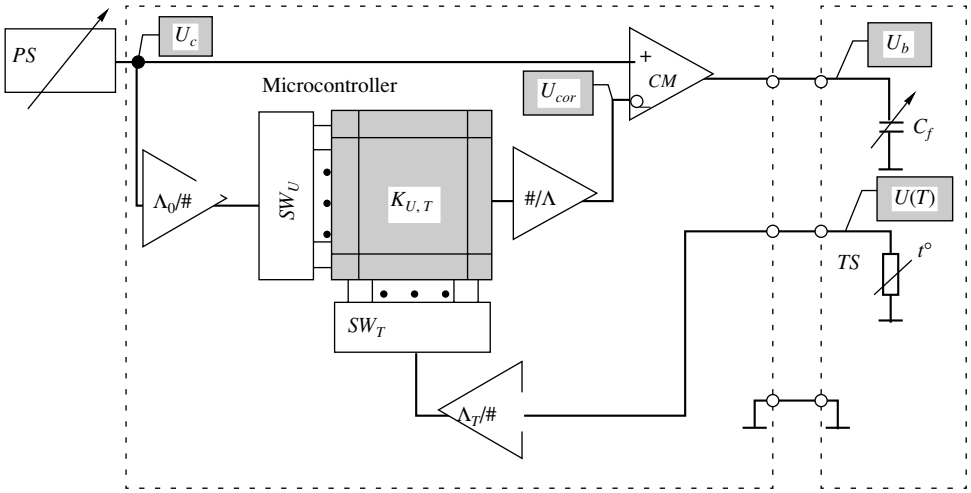

Fig. 2. Schematic diagram of the bias voltage correction module (CVM) (see the text for explanations).

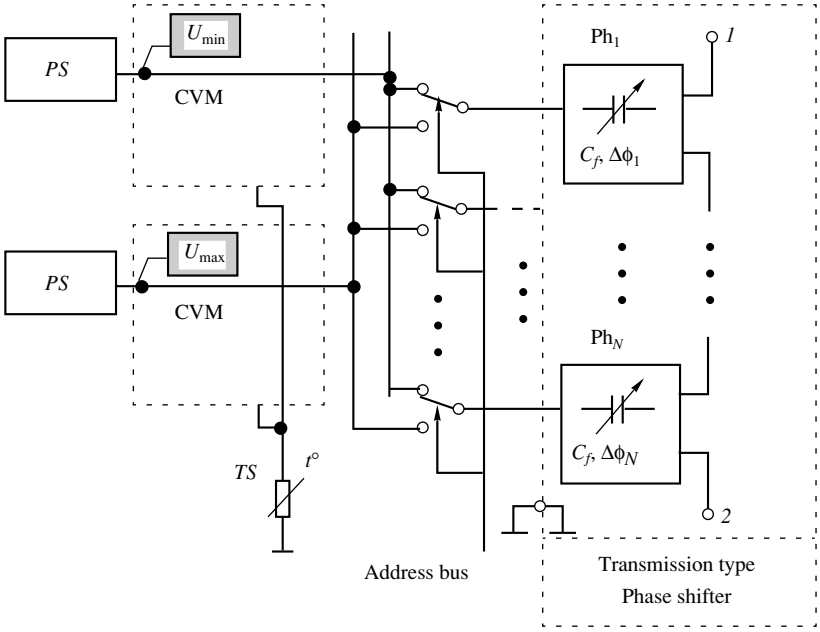

Fig. 3. Schematic diagram of the application of corrected bias voltage to discrete phase shifters (Ph_1, …, Ph_N): (*1*) input; (*2*) output.

the analog correction voltage U_{cor} and fed to the comparator *CM*. Upon comparing the U_c and U_{cor} values, *CM* yield the required bias voltage U_b applied to the controlled device. In this bias voltage correction scheme, the characteristic time of response to a temperature variation is on the order of 10 μs.

An advantage of the proposed method is its flexibility, which is provided by changing the tabulated *CC* values. A certain disadvantage is the discreteness of the working temperature interval (limited by the digital capacity of DACs and ADCs) that has to be divided into subintervals. If each bit of the phase shifter corresponds to the same capacitance, the number of control units can be reduced to two. In this circuit, only one temperature sensor is required for both correction units controlling the ferroelectric capacitors. The corresponding commutation scheme is depicted in Fig. 3, where CVM are the voltage correction modules described above (Fig. 2). In this case, the device response speed is determined by the operation time of elements switching the temperature-compensated bias voltage.

In the case of phased-array antennas of large size, featuring nonuniform temperature distribution over the entire area, it is necessary to use several CVMs and temperature sensors for each temperature region.

Acknowledgments. The authors are grateful to O.G. Vendik and I.B. Vendik for fruitful discussions.

This study was supported in part by the Ministry of Education of the Russian Federation (project no. PD02-2.7-130) and by the Ministry of Industry, Science, and Technology of the Russian Federation (project no. 239 SP/MLP-10 within the framework of the State Contract no. 40.012.1.11.46 of 01.02.02).

REFERENCES

1. *Semiconductors Based on Barium Titanate*, Ed. by V. M. Petrov (Énergoizdat, Moscow, 1981).
2. O. G. Vendik, S. P. Zubko, S. F. Karmanenko, *et al.*, J. Appl. Phys. **91**, 331 (2002).
3. E. K. Hollmann, V. I. Gol'drin, V. E. Loginov, *et al.*, Pis'ma Zh. Tekh. Fiz. **25** (14), 1 (1999) [Tech. Phys. Lett. **25**, 549 (1999)].
4. A. M. Prudan, Doctoral Dissertation (St. Petersburg State Electrotechnical Univ., St. Petersburg, 2002).
5. A. Prudan, A. Kozyrev, A. Zemtsov, *et al.*, in *Proceedings of the 15th International Symposium on Integrated Ferroelectrics (ISIF 2003), Colorado Springs, 2003.*
6. O. G. Vendik and S. P. Zubko, J. Appl. Phys. **82**, 4475 (1997).
7. O. G. Vendik, S. P. Zubko, and M. A. Nikol'ski, J. Appl. Phys. **92**, 7448 (2002).
8. O. G. Vendik, M. A. Nikol'ski, and S. P. Zubko, J. Appl. Phys. (2003) (in press).
9. O. G. Vendik, S. P. Zubko, and M. A. Nikol'skiĭ, Zh. Tekh. Fiz. **69** (4), 1 (1999) [Tech. Phys. **44**, 349 (1999)].
10. O. G. Vendik and M. A. Nikol'skiĭ, Pis'ma Zh. Tekh. Fiz. **29** (5), 20 (2003) [Tech. Phys. Lett. **29**, 184 (2003)].

Translated by P. Pozdeev

Technical Physics Letters, Vol. 29, No. 9, 2003, pp. 732–735. Translated from Pis'ma v Zhurnal Tekhnicheskoĭ Fiziki, Vol. 29, No. 17, 2003, pp. 62–71.

Separating a Weak Periodic Component from a Nonstationary Time Series

L. M. Martyushev*, E. G. Aksel'rod, and A. P. Sergeev

Institute of Industrial Ecology, Ural Division, Russian Academy of Sciences, Yekaterinburg, Russia

** e-mail: mlm@ecko.uran.ru*

Received March 25, 2003

Abstract—Various approaches to separating a weak periodic component from a noisy nonstationary time series are considered in the case when aprioric information about useful signal is unavailable and multiply repeated measurements are impossible. The proposed methods have been used for studying the time variation of the mass of a dendritic crystal of ammonium chloride growing from an aqueous solution. It is established that the kinetic curves obtained for growth rates above 20 μm/s exhibit low-frequency oscillations with a period of about 3 s.

The problem of separating a periodic component from a very noisy nonstationary time series is still not completely solved despite the extensive literature on this subject [1–4]. The most significant difficulties are encountered in two cases: (i) when the experiment cannot be multiply repeated and (ii) when aprioric information is available neither about the periodic component nor about the functional type of the trends (this information has to be extracted in the course of investigation). In such cases, the signal to noise ratio becomes a very significant parameter.

Should there appear the possibility of multiply repeating the experiment and/or obtaining some preliminary information about the useful signal, the separation and analysis of the signal component of interest are always possible. In the former case, the signal to noise ratio increases as the square root of the number of observations; and in the latter case, the useful signal can always be separated by using specially selected filters.

Thus, of special interest is the most complicated case, when there is a single nonstationary time series and no aprioric information is available about the signal. This study is devoted to an analysis of such situations, which are typical of real physical experiments. The paper consists of two parts: in the first of these, we will consider some model generated time series; in the second part, we will analyze the results of particular experiments with the growth of dendritic crystals from solution.

Let us consider a noisy S-shaped curve (Fig. 1) for which it is necessary to establish whether a hidden periodicity is present or absent. This shape is taken, first, for the sake of definiteness and, second, because it is frequently encountered in various evolution and kinetic processes. The periodic component is characterized by the amplitude (A), shape, number (n), and duration (T) of pulses. The latter parameter is conveniently normalized to the total number of points N in the time series. Our task is only to reveal the periodicity (and determine the period) rather than to describe the shape of this periodic signal. For certainty, we will consider rectangular periodic pulses and assume the noise to be additive and Gaussian with zero mean and a given mean square deviation (sd).

We have analyzed two cases corresponding to $n = 3$ and $T/N = 1/10$ (1) or $1/100$ (2). It was necessary to determine the limiting ratio A/sd for which the presence of a periodic component can still be detected. Evidently, an increase in n will decrease the possible limiting ratio. Selecting such a small n value, we attempt to assess the most unfavorable situation with a very small possible number of periods in the given time series.

Case 1: $n = 3$, $T/N = 1/10$; N = 1000; frequency, 0.003. For $A/sd \le 2$, it is impossible to visually deter-

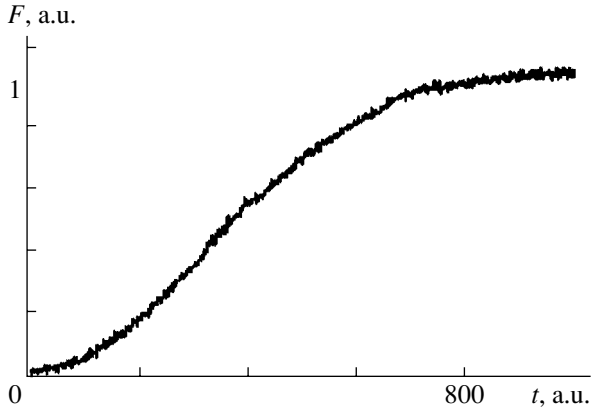

Fig. 1. A model curve of F versus relative time t obtained by imposing a Gaussian noise (with a zero mean and a finite dispersion sd) and rectangular pulses ($n = 3$, $T/N = 1/10$, $N = 1000$, $A/sd = 1.5$) onto a Weibull distribution.

1063-7850/03/2909-0732$24.00 © 2003 MAIK "Nauka/Interperiodica"

mine whether a periodic feature is present on the experimental curve (Fig. 1). Oscillations on such curves can be revealed by various techniques [3, 4].

(a) Spectral transformation of a nonstationary series and of the time series upon differentiation (Fig. 2a). As can be seen, these methods reveal nothing. It should be noted that the results of model calculations for $A/sd > 2$ (slightly distinguishable oscillations) showed that these direct methods reveal the presence of a periodic component with good precision. It was also found that the best results are obtained using a spectral window of the Blackman type, while preliminary differentiation frequently does not improve the result.

(b) Subtraction of trends of three different types. The trends were selected using the special program package TableCurve2D. Preference was given to the trends possessing a sufficiently large correlation coefficient r^2. Figure 2b shows the results of spectral transformations obtained upon subtraction of two different trends (with one of the maximum r^2 values) from the nonstationary time series of Fig. 1. As can be seen, the results obtained using various trends are significantly different. In the first case, there is a maximum peak corresponding to a frequency of 0.0019, while the second pattern is rather close to the noise spectrum. Note that, according to the results of TableCurve2D calculations, the Weibull trend used for the construction of a curve (Fig. 1) has $r^2 = 0.9989$. An analysis of the results of numerous calculations showed that, using various regression dependences (adequately describing the initial time series) as subtracted trends, it is possible to come to various conclusions concerning the fluctuating component of a signal of the type depicted in Fig. 1 (from noisy behavior to a periodic character with strongly different frequencies).

(c) Based on the data reported in [5], we also attempted to apply the currently popular wavelet transform using a special module of the MATLAB program package. We have tested several types of the most widely used wavelets (including those of Morlet, Mexican hat, and some other types) and tried different degrees of detalization. However, the results of these model calculations showed that wavelet techniques are ineffective in separating periodicity in the problems under consideration.

(d) Using the moving average method for reducing the time series to a stationary form encounters the same difficulties as in (1b). Smoothing over too small a number of points, we risk subtracting a possible periodicity together with the nonstationary component; on the other hand, increasing the number of such points above a certain threshold can artificially introduce special frequencies.

Nevertheless, this approach allowed us to construct a simple and readily implemented (on a program level) method (called Σ method), which allows a periodic component to be separated from a time series of the type depicted in Fig. 1. According to this method, one has to repeatedly calculate the residues upon subtraction (from the initial time series) of the trend found by the moving average method with sequentially varied number of the smoothening points. Then an amplitude spectrum (or an autocorrelation function) is calculated for each series of residues and the spectra (normalized to maximum) are added. The resulting sum is essentially a probability of finding one or another frequency in the time series under consideration.

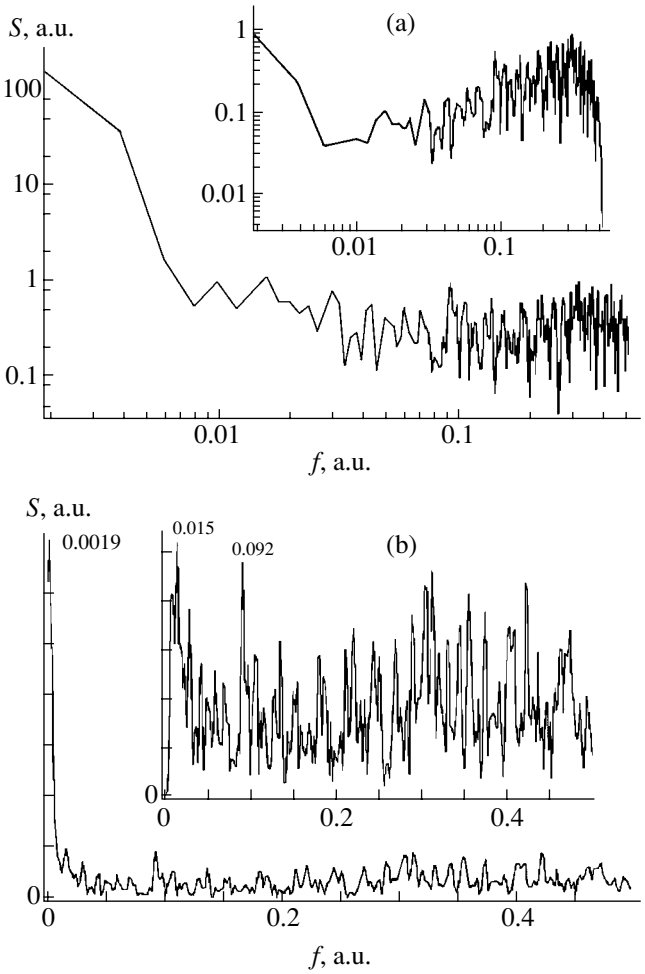

Fig. 2. The results of a spectral analysis of the curve presented in Fig. 1. The transformation was performed over 512 points using a spectral window of the Blackman type for (a) nondifferentiated and differentiated (inset) time series and (b) residues upon subtraction of the trend $\ln F = a + bt^{1.5} + c\ln t$ (where a, b, and c are the parameters of a regression curve; $r^2 = 0.9984$) and the residues upon subtraction of a polynomial of the 20th power (inset, $r^2 = 0.9992$).

Obviously, it is the absence of any preliminary information about the period of the oscillating component that makes it necessary to use this procedure with accumulation. Figure 3 shows the corresponding total autocorrelation function for a time series of the type depicted in Fig. 1; this function was calculated using the moving averages calculated for 50–200 points. The

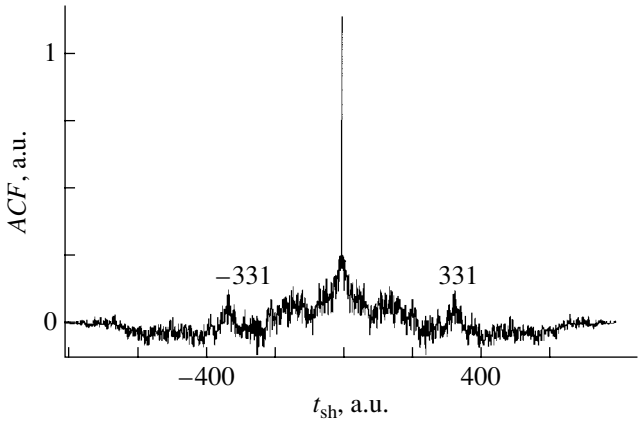

Fig. 3. Total autocorrelation function (*ACF*) versus shear time t_{sh} calculated for the model curve presented in Fig. 1.

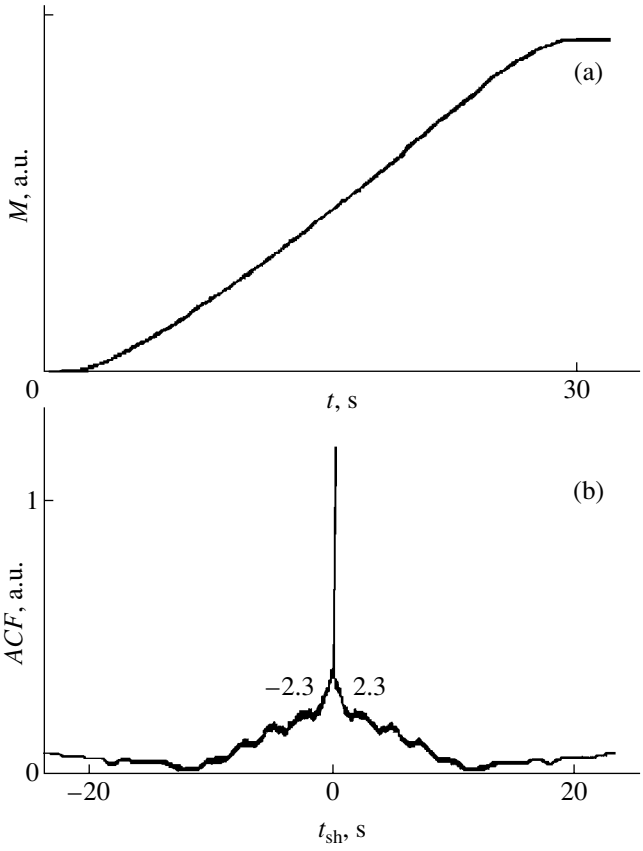

Fig. 4. The results of experiments on the dendrite growth: (a) dendrite weight *M* versus time; (b) total autocorrelation function (*ACF*) versus shear time.

difference between the two nearest peaks amounts to 331 and, hence, the relative error of the frequency determination is below 1%. Therefore, this method is capable of revealing the hidden periodicity of a nonstationary signal.

However, the results of numerous calculations performed for signals of the type depicted in Fig. 1 showed that, within the framework of this method, conclusions concerning the presence of periodicity can be obtained only with a certain probability. This is related to the fact that the model calculations employ random Gaussian noise with a dispersion virtually equal to the signal amplitude. Conclusions based on the calculations performed for several dozen model signals were as follows: for $A/sd = 2$, 1.7, 1.5, and 1.2, the probabilities of correctly separating the hidden periodicity and determining the period are 1, 0.80, 0.78, and 0.50. Thus, the quality of predictions based on the Σ method sharply decreases for the A/sd ratios below 1.5.

Our investigations showed that the probability of revealing a hidden periodic signal can be increased using two methods: (i) instrumental increase in the signal discretization (provided that this does not decrease the signal to noise ratio); (ii) use of the Σ method for the analysis of several sample sets taken from the unit signal, followed by the summation of all the total autocorrelation functions (or spectra). Useful information is also obtained by calculating various correlation functions between the residues determined for various sample sets by averaging over various numbers of points.

As an example, we present the result obtained by simultaneously using methods (a) and (b). Here, we studied the time series with $n = 3$ and $T/N = 1/10$, but the number of discretization points was increased from 1000 to 10000. Using this series, we formed sample sets of two types: (i) five time series, each of 1000 points and (ii) 50 series, each of 100 points (with equal intervals between points). The final result was as follows: for $A/sd = 1.5$ and 1, the probability of correct periodicity determination was 0.91 and 0.62, respectively. As A/sd decreases below unity, the probability of correct prediction for the time series under consideration exhibits a sharp drop (to 0.30 for $A/sd = 0.8$).

Case 2: $n = 3$, $T/N = 1/100$; $N = 1000$). For $A/sd \leq 2.5$, it is impossible to visually determine whether a periodic feature is present or not on the model curve. Here, use of all the above techniques, including the Σ method, did not provide reliable results. Our model calculations led to a conclusion that only increasing discretization of the signal can reveal the hidden periodicity (for $T/N = 1/100$ and N increased to 10000, the signal with $A/sd = 2.5$ is revealed with a probability of 1.00). Thus, detecting small-amplitude signals of short duration encounters considerable difficulties.

The above results were used for the analysis of experimental data on the growth kinetics for a separate dendritic crystal of ammonium chloride in an aqueous solution. The investigation was aimed at finding a nonrandom periodic component on the nonstationary curve of the dendrite weight versus time. The experimental techniques were described in detail elsewhere [6, 7]. Preliminary statistical analysis of the kinetic curves [6, 7] by methods (a)–(d) revealed the presence of a nonrandom periodic component. However, as noted above, the accuracy of these methods is not always sufficiently

high. In order to quantitatively refine the results obtained in [6, 7], we have performed an additional investigation.

The experimental system scheme was modified as compared to that described in [6, 7]: first, we used an electronic scheme possessing higher noise immunity for the signal detection and amplification; second, we employed a new data acquisition module (ADC: Lcard-1250). As a result, the signal discretization was increased by several orders of magnitude without loss in the experimental accuracy. We have obtained several kinetic curves similar to that presented in Fig. 4a, representing typical S-shaped curves with a total duration not exceeding one minute (and discretization over 66 152 points). An important feature of the system studied is the impossibility of multiply repeating the experiment with unchanged parameters. All the time series referred to different dendritic crystals. For this reason, statistical analysis was performed independently for each case.

The periodic components were revealed by the Σ method. Figure 4b shows a typical total autocorrelation function. The form of this curve is indicative of the presence of a nonaccidental periodic component in the time series under consideration. Based on the results of processing of all the experimental curves by the Σ method, it is possible to ascertain that the kinetic curve of dendrite weight versus time contains a nonrandom periodic component with a period of 2.8 ± 0.8 s. This value, being approximately one-third of that reported previously, agrees much better with the theoretical estimates [6, 7]. According to another interesting result obtained upon statistical data processing, the oscillating component of the kinetic curves depends on the dendrite growth rate. The nonrandom oscillations are most reliably revealed for a growth rate of 20–30 μs. For samples grown at lower rates, the maxima on the curves of the type depicted in Fig. 4b are either less pronounced or absent. Therefore, determining oscillations on the kinetic curves of slowly growing dendrites requires additional investigation.

REFERENCES

1. L. A. Vaĭnshteĭn and V. D. Zubakov, *Signal Extraction from the Background of Random Disturbances* (Sov. Radio, Moscow, 1960).
2. B. R. Levin, *Theoretical Grounds of Statistical Radio Engineering* (Sov. Radio, Moscow, 1975), Vol. 2.
3. Yu. N. Tyurin and A. A. Makarov, *Statistical Data Analysis with PC* (INFRA, Moscow, 1998).
4. *Computer Processing of Experimental Data*, Ed. by S. Minami (Radio i Svyaz', Moscow, 1999).
5. V. P. D'yakonov, *Wavelets: from Theory to Practice* (SOLON-R, Moscow, 2002).
6. E. G. Aksel'rod, L. M. Martyushev, and E. V. Levkina, Pis'ma Zh. Tekh. Fiz. **25** (20), 64 (1999) [Tech. Phys. Lett. **25**, 830 (1999)].
7. E. G. Axelrod, L. M. Martiouchev, and Y. V. Lyovkina, Phys. Status Solidi A **182**, 687 (2000).

Translated by P. Pozdeev

Technical Physics Letters, Vol. 29, No. 9, 2003, pp. 736–738. Translated from Pis'ma v Zhurnal Tekhnicheskoĭ Fiziki, Vol. 29, No. 17, 2003, pp. 72–77.

Bifurcation Phenomena with Additive Increase in the Oscillation Period in a System with One and a Half Degrees of Freedom

N. A. Maksimov and S. V. Savel'ev

Institute of Radio Engineering and Electronics, Russian Academy of Sciences, Fryazino, Moscow oblast, Russia
e-mail: savelyev@ms.ire.rssi.ru

Received March 13, 2003

Abstract—The results of numerical calculations show that a system with inertia exhibits a sequence of oscillatory bifurcations in accordance with the natural scale law. It is established that the sequence of bifurcation values of the inertia parameter obey a convergence law; the corresponding moments are determined. © *2003 MAIK "Nauka/Interperiodica".*

Featuring rich dynamics, systems with inertia have been extensively studied (see, e.g., [1–5]). In these systems, which exhibit regular and complicated dynamics, evolution of the autooscillation process depends both on the connection of the inertial chain and on the type of dynamic characteristics of the nonlinear amplification element. In particular, a system with one and a half degrees of freedom (representing a modified oscillator with inertia) [1, 2] demonstrates a sequence of period-doubling bifurcations on the transition to chaos.

Previously [3], an autooscillation system was experimentally studied in which the transition to chaos took place as a result of sequential increase in the oscillation period according to the natural scale law. However, such a scenario was never studied by methods of numerical simulation.

We have studied by numerical method a system with inertia described by the equations

$$\begin{aligned} \dot{X} &= Y + (m_1 - m_2)X - XZ, \quad X \le q, \\ \dot{X} &= Y - m_2 X - qZ, \quad X > q, \\ \dot{Y} &= -X, \\ \dot{Z} &= -gZ + gF(X)X^2, \end{aligned} \tag{1}$$

where $F(X)$ is the Heaviside function; m_1, m_2, q, and g are the parameters of excitation, dissipation, limitation, and inertia, respectively. System (1) differs from the aforementioned modified oscillator with inertia by the shape of the dynamic characteristic of a nonlinear amplifier, which has a linear region at $X \le q$ and exhibits saturation for $X > q$. The fourth equation in system (1) describes an inertial half-period converter. Therefore, the system dynamics is determined by two mechanisms of limitation of the autooscillations. The first mechanism is noninertial and is related to the nonlinearity of the amplifier characteristic. The second mechanism is inertial and is related to the influence of an output voltage of the inertial converter on the slope of the nonlinear amplifier characteristic.

Evolution of the oscillatory process in system (1) is clearly illustrated by a fragment of the bifurcation diagram (Fig. 1) showing a change in the maximum values $[X]$ of the oscillation process $X(t)$ versus adiabatically changed parameter g for $m_1 = 1.6$; $m_2 = 0.1$, and $q = 0.05$. A small change in the $[X]$ value on the bifurcation diagram corresponds to regular dynamics of the system, while the random scatter of points represents chaotic dynamics. As the inertia parameter varies, the system exhibits a series of bifurcations. In the interval $g \in [0.57; 0.65]$, the system dynamics is characterized by a stable limiting cycle of period T_0. The interval of $g \in [0.56; 0.57]$ corresponds to chaotic oscillations. The point at $g = 0.56$ corresponds to a bifurcation,

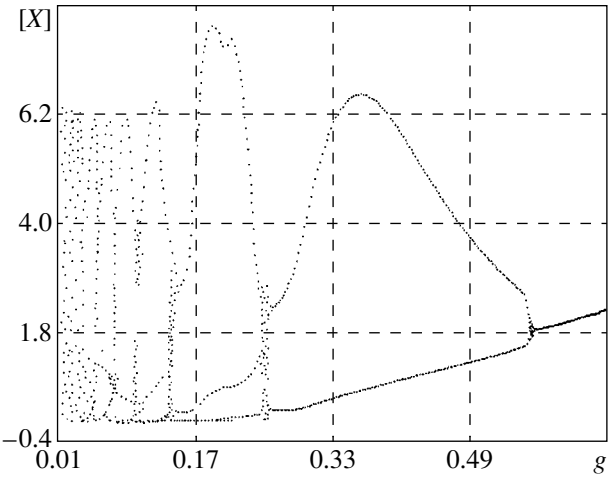

Fig. 1. A fragment of the bifurcation diagram.

1063-7850/03/2909-0736$24.00 © 2003 MAIK "Nauka/Interperiodica"

where the system dynamics exhibits period doubling with a limiting cycle of period $2T_0$ taking place in the interval of $g \in [0.26; 0.56]$. Upon reaching the value of $g = 0.24$, the system behavior corresponds to motion over a stable cycle of period $3T_0$. The zones of double and triple period are separated by the region of chaotic oscillations at $g \in [0.24; 0.26]$. Further decrease in the inertia parameter is accompanied by changes in the system state through a sequence of stable limiting cycles with the oscillation period increasing by unity. The zones of stable states with the periods nT_0 and $(n + 1)T_0$ are separated by the regions of chaotic oscillations. In the course of sequential bifurcations, the distances between critical values of parameter decrease so that the zones of chaotic oscillations appear more and more frequently.

The above bifurcation scenario of oscillations with the additive increase in the oscillation period by unity allows us to expect that the sequence of bifurcation values of the inertia parameter g_n converges. This implies that the sequence g_n obeys a convergence law of the type

$$g_k - g_n \sim n^{\gamma}, \tag{2}$$

where g_k and g_n are bifurcation values of the parameter g, γ is a constant quantity, and $n = 1, 2, \ldots$. Relations of the type (2) were established for a sequence of two-dimensional tores (see, e.g., [4, 5]). Therefore, it would be of interest to study the law of convergence for a sequence of limiting cycles in a system with one and a half degrees of freedom.

In order to determine the scale-invariant properties, we have revealed n terms in the sequence of stable cycles of system (1) with fixed bifurcation values of the parameter g_n. The results of numerical calculations showed that the convergence law was obeyed with a good precision, as evidenced by the graphic verification of the scale-invariant properties for g_n (see Fig. 2, curves *1–3* constructed for $m_1 = 1.8$, 1.6, and 1.4, respectively). The statistical significance of the results was confirmed by the linear correlation coefficients determined using least squares for the relation

$$Q = A + \gamma\Theta, \tag{3}$$

where $Q = \ln(g_k - g_n)$, $\Theta = \ln n$, and A and γ are constant quantities. Estimates for the sequence of multiple stable cycles and the corresponding inertia parameter g_n lead to the conclusion that the system obeys a convergence law with constant $\gamma = -3.75 \pm 0.17$. Using the similarity law (2), it is possible to calculate the accumulation point of the g_n sequence. For the above parameters, this point corresponds to $g_c = 0.008 \pm 0.001$.

The mechanism of the transition to chaotic oscillations is illustrated by fragments of the projections of a strange attractor in the phase space of the system onto the planes (X, Y) and (X, Z) for the values $g < g_c$ (see Figs. 3a and 3b, respectively, where arrows indicate the motion of an imaging point in the phase space. An analysis of Fig. 3 shows that the form of an attractor in

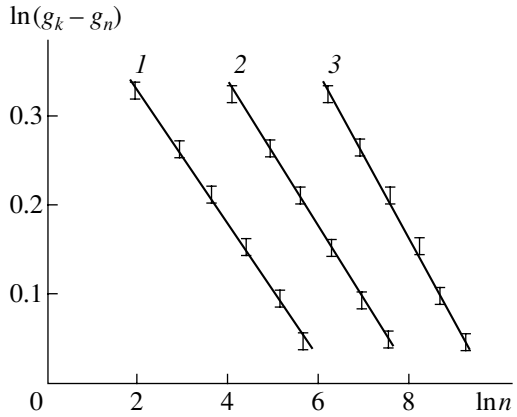

Fig. 2. Verification of the convergence law.

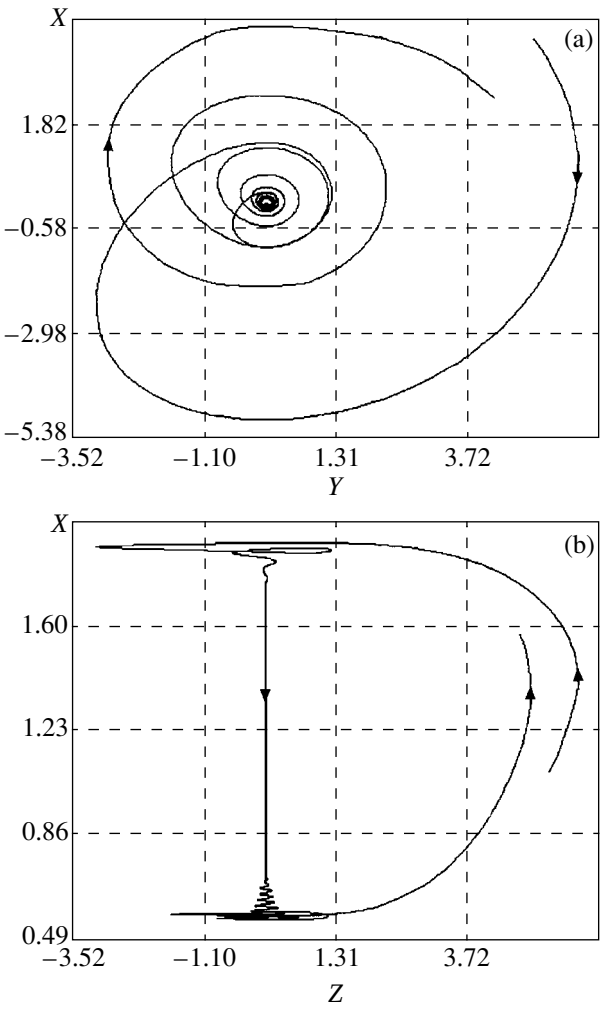

Fig. 3. Fragments of the projections of a strange attractor of the system onto the (X, Y) and (X, Z) planes in the phase space.

phase space is determined by a double saddle–focus loop with a characteristic transient motion along the saddle separatrix. The phase space of the system features a double attractor of the Shil'nikov type [6] comprising a stable focus and unstable saddle or unstable focus and stable saddle motions.

The above analysis shows that a global chaotization of oscillations in the system studied is preceded by a sequence of bifurcations according to the natural scale law, whereby the zones of stable motion alternate with the zones of chaotic motion. The sequence of bifurcation values of the inertia parameter obeys a similarity law. The mechanism of chaotization is related to the loss of stability at a double saddle–focus loop.

Acknowledgments. This study was supported by the Russian Foundation for Basic Research, project nos. 01-02-17529 and 01-07-90349.

REFERENCES

1. V. S. Anishchenko, V. V. Astakhov, and T. E. Letchford, Zh. Tekh. Fiz. **53**, 152 (1983) [Sov. Phys. Tech. Phys. **28**, 91 (1983)].
2. V. S. Anishchenko, Pis'ma Zh. Tekh. Fiz. **10**, 629 (1984) [Sov. Tech. Phys. Lett. **10**, 266 (1984)].
3. N. A. Maksimov and V. Ya. Kislov, Pis'ma Zh. Tekh. Fiz. **9**, 979 (1983) [Sov. Tech. Phys. Lett. **9**, 421 (1983)].
4. Yu. I. Neĭmark and P. S. Landa, *Stochastic and Chaotic Oscillations* (Nauka, Moscow, 1987; Kluwer, Dordrecht, 1992).
5. A. S. Dmitriev and V. Ya. Kislov, *Stochastic Oscillations in Radiophysics and Electronics* (Nauka, Moscow, 1989).
6. L. P. Shil'nikov, *Problems of Nonlinear and Turbulent Processes in Physics* (Naukova Dumka, Kiev, 1985), pp. 118–124.

Translated by P. Pozdeev

Technical Physics Letters, Vol. 29, No. 9, 2003, pp. 739–742. Translated from Pis'ma v Zhurnal Tekhnicheskoĭ Fiziki, Vol. 29, No. 17, 2003, pp. 78–85.

The Effect of Postgrowth Annealing on the Structure and Optical Properties of Multilayer Ge/Si Heterostructures

A. A. Tonkikh[a,b,c], V. G. Talalaev[c], N. D. Zakharov[c], G. E. Cirlin[a,b,c,*], V. M. Ustinov[b], and P. Werner[c]

[a] *Institute of Analytical Instrument Building, Russian Academy of Sciences, St. Petersburg, Russia*

[b] *Ioffe Physicotechnical Institute, Russian Academy of Sciences, St. Petersburg, 194021 Russia*

[c] *Max Planck Institut für Mikrostrukturphysik, Halle, Germany*

* *e-mail: cirlin@ioffe.rssi.ru*

Received April 9, 2003

Abstract—The effect of the postgrowth laser and thermal annealing on the structure and optical properties of multilayer heterostructures comprising quantum dots of germanium in a silicon matrix has been studied by photoluminescence (PL) and transmission electron microscopy (TEM). The PL spectra of annealed samples reveal a decrease of emission from the quantum dots and display a new emission band as compared to the initial spectra. The TEM measurements show that this effect is related to smearing of the Ge–Si interface and to the appearance of a regular rectangular network of dislocations on the surface of the annealed structure. © *2003 MAIK "Nauka/Interperiodica".*

Introduction. Silicon still occupies leading positions in the market of materials for microelectronic devices. However, use of this semiconductor in optoelectronics is limited because of relatively low luminescence efficiency. Nevertheless, combining silicon microelectronic technologies with the optical data transmission facilities in the same microchip is an urgent task drawing considerable research effort, primarily in the field of silicon-based light-emitting devices (SLEDs).

Previously, two groups of researchers [1, 2] reported on an intense photoluminescence (PL) in the region of 1.5 μm for the heterostructure comprising germanium quantum dots (QDs) in a silicon matrix. Recently, we studied the nature of room-temperature PL in multilayer Ge/Si(100) structures with germanium QDs [3].

This study was aimed at determining the effect of the postgrowth laser and thermal annealing on the structure and optical properties of multilayer Si/Ge heterostructures comprising 20 layers of germanium QDs in a silicon matrix.

Experiment. The heterostructures were grown in a Riber SIVA 45 setup (France) by MBE on 5-inch *p*-Si(100) wafers (OKMETIC, Sweden). The substrates were chemically pretreated using a procedure described in detail elsewhere [4]. During the MBE growth, the atomic fluxes of Si and Ge were generated by electron-beam evaporators, while a constant deposition rate was monitored and controlled using a feedback system with two mass spectrometers tuned to m/z = 28 (Si) and 74 (Ge). The samples were selectively doped with antimony evaporated from an effusion source. The residual pressure during MBE growth did not exceed 5×10^{-10} Torr. The state of the sample surface was monitored *in situ* by reflection high-energy electron diffraction (RHEED). The sample structures comprised a 100-nm-thick buffer layer of silicon, followed by 20-layer Ge(0.8 nm)/Si(5 nm) superlattice doped with antimony. The substrate temperature during the entire growth process was maintained constant (T_{sub} = 600°C). The MBE rates of Si and Ge layers were 0.05 and 0.015 nm/s, respectively.

After extraction from vacuum, the wafers were cut into several parts, which were subject to the procedures of laser and thermal annealing. The series studied included nine samples annealed at various temperatures, one laser-annealed sample, and one control (unannealed) sample. Thermal annealing was performed at 700, 800, and 900°C for 10, 20, or 30 min in argon at atmospheric pressure. The laser annealing was performed with a focused beam of an Ar^+ laser operating at an output power density of 150 kW/cm^2. The photoluminescence spectra were also excited by the Ar^+ laser at λ = 488 nm and measured using a 50-cm monochromator and a cooled Ge photodetector (Edinburgh Instruments, UK). Electron microscopy (TEM) measurements in transmission mode were performed on a JEM 4010 instrument.

1063-7850/03/2909-0739$24.00

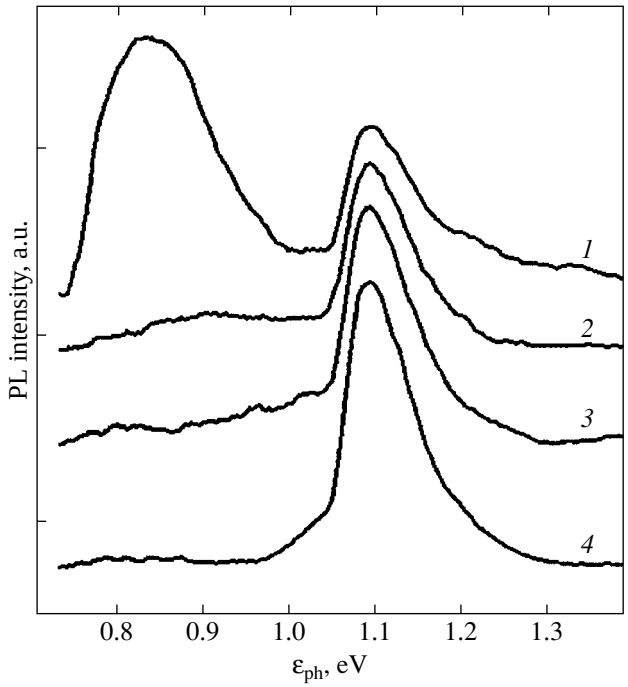

Fig. 1. Typical PL spectra of a multilayer Ge/Si(100) heterostructure (*1*) before annealing and upon a 10-min thermal annealing at T = 700 (*2*), 800 (*3*), and 900°C (*4*).

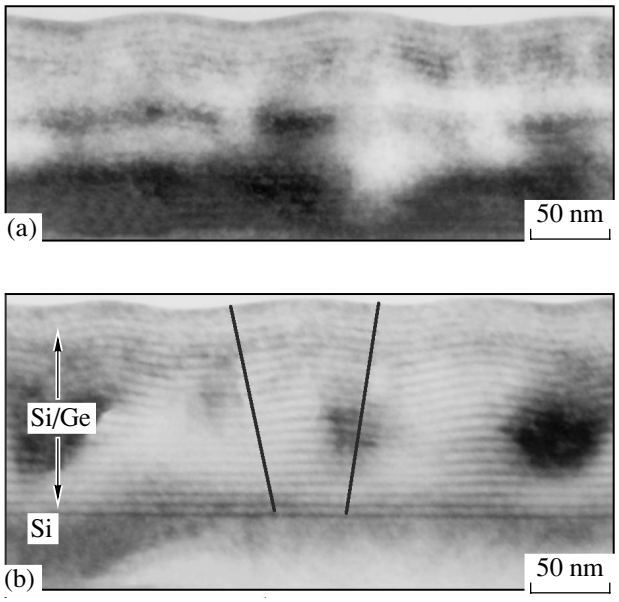

Fig. 2. TEM images of the cross section of Ge/Si(100) heterostructures (a) before unannealing and (b) after thermal annealing for 30 min at 900°C (lines bound one of the columns of germanium QDs).

Results and discussion. Figure 1 shows the room-temperature PL spectra of the samples studied. The spectrum of sample 1 (unannealed control) exhibits two bands. The first of these (about 1.1 eV) corresponds to transitions in the silicon matrix involving transverse optical phonons. The mechanism responsible for the second band at 0.8–0.9 eV was described in our previous paper [3], where it was demonstrated that vertically correlated germanium QDs provide for the localization of holes, while the silicon layers in these stacks form a miniband for electrons. The quasidirect optical transitions between localized holes and quasifree electrons account for the PL at 0.8–0.9 eV. As can be seen from Fig. 1, this band is virtually missing from the spectra of annealed samples 2–4, being very small even in sample 2 annealed at a temperature of 700°C for a minimum time of 10 min. The character of the PL spectra remains unchanged upon annealing at higher temperatures for a longer time.

In order to elucidate the factors responsible for this degradation of the PL spectrum, we studied the TEM images obtained in the plane and in the cross section of the samples. Figure 2 compares the cross sections of a sample before and after thermal annealing. While the unannealed structure exhibits rather sharp heteroboundaries between Ge and Si layers, the annealing leads to strong smearing of these boundaries. The smearing of heteroboundaries is explained by thermostimulated mutual diffusion of Ge and Si. As a result, the superlattice of germanium QDs and silicon layers either ceases to exist or strongly changes the profile, which leads to a decrease in the barrier height, degeneracy of the miniband for electrons, and delocalization of holes. Thus, the emission line corresponding to the quasidirect transition virtually disappears from the PL spectrum [3].

Another interesting effect is revealed by TEM images of the sample surface. As can be seen from Fig. 3, both annealed and unannealed samples exhibit a cellular structure, but the annealing leads to the appearance of a regular rectangular network of dislocations with characteristic dimensions 1.5×2.75 μm. The emergence of dislocations is related to a change in the mechanism of elastic stress relaxation upon annealing. In the unannealed structure, the stresses relax at the expense of germanium QD column formation and/or surface corrugation. In the annealed structure, the accumulated stresses can relax via two scenarios: (i) the smearing of heteroboundaries due to the mutual diffusion of germanium and silicon and (ii) the formation of misfit dislocations related to the lattice mismatch between silicon and germanium. The type of stress relaxation is probably determined by the rate of annealing. Rapid and virtually inertialess annealing was provided by exposure to focused laser radiation at 488 nm and a power density of 150 kW/cm^2.

Figure 4 compares the PL spectra of unannealed sample 1 to those of the laser-annealed samples 2–4 measured at various excitation densities. As can be seen from these data, the spectra of all samples exhibit two peaks, but the positions of these peaks are different for annealed and unannealed structures. In the spectrum of

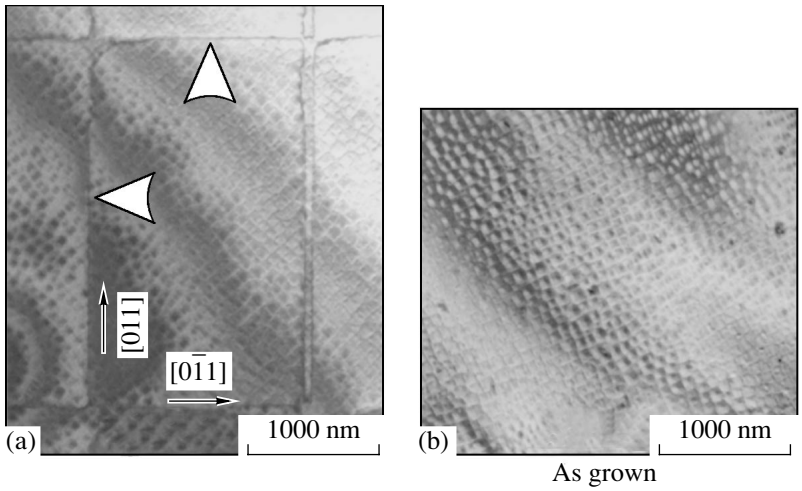

Fig. 3. TEM images of the surface of Ge/Si(100) heterostructures: (a) after thermal annealing for 30 min at 900°C (triangles indicate the sides of a dislocation network); (b) unannealed sample.

sample 1, the short-wavelength peak corresponds to the transitions in silicon matrix involving transverse optical phonons. In the spectra of annealed samples, the short-wavelength peak is related, in our opinion, to the dislocation luminescence [5]. The long-wavelength peaks in the spectra of annealed and unannealed samples are apparently of the same nature, while the small shift toward shorter wavelengths (9 meV) is explained by changes in the size and shape of the Si/Ge superlattice as a result of the laser annealing. As can be seen, the intensity of the short-wavelength peak in the PL spectrum grows with the excitation density. This is probably explained by the increasing role of the dislocation luminescence. A change in the excitation density does not affect the energy position of this emission component.

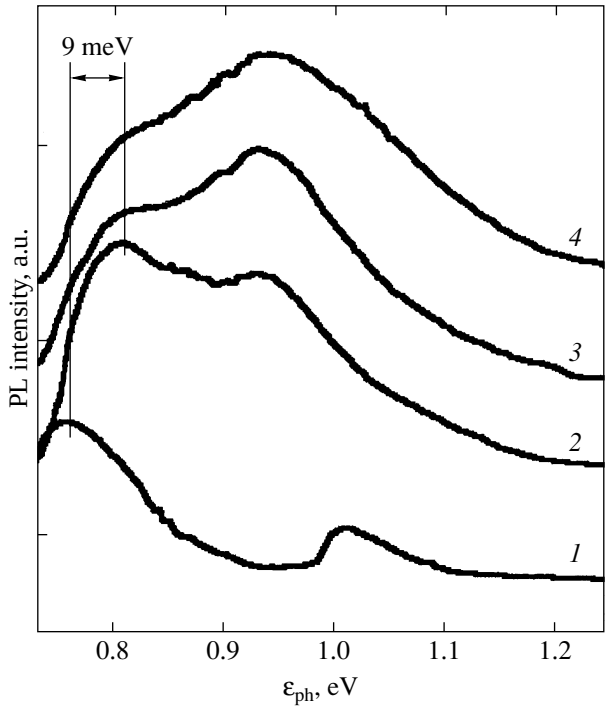

Fig. 4. Normalized PL spectra of a Ge/Si(100) heterostructure (*1*) before annealing and (*2–4*) after laser annealing, measured with various excitation power densities $W = 5$ (*1*), 3 W/cm^2 (*2*), 0.3 (*3*), and 15 kW/cm^2 (*4*).

It should be noted that the stress relaxation by the dislocation mechanism is of independent interest, since the dislocation network decreases stresses in the Si/Ge heterostructure, while the proximity of lattice parameters of the surface layer to those of germanium makes such structures promising "virtual substrates" for the obtaining of LEDs, based on $A^{III}B^{V}$ semiconductor compounds of the Ga(Al,In)As type, on silicon substrates. In addition, the nodes of the regular dislocation network may serve as the centers of nucleation for nanodimensional clusters, thus probably providing for the ordered arrangement of such clusters.

Conclusions. Thus, we have established that thermal annealing of a multilayer Si/Ge heterostructure leads to disappearance of the PL peaks corresponding to emission from the Si/Ge superlattice, while laser annealing significantly modifies the shape of the PL spectrum. This effect is probability related (i) to a change in the composition profile of the superlattice as a result of mutual diffusion of silicon and germanium and (ii) to the appearance of a regular dislocation network. The results of our investigation show that high-temperature growth of such structures is hindered by the significant influence of the kinetic processes on the behavior of Ge atoms in silicon matrix, which lead to the formation of misfit dislocations, mixing of the material, and smearing of heteroboundaries.

Acknowledgments. This study was supported in part by the Ministry of Industry, Science, and Technology of the Russian Federation.

One of the authors (G.E.C.) is grateful to the Alexander von Humboldt Foundation for support.

REFERENCES

1. H. Sunamura, N. Usami, Y. Shiraki, and S. Fukatsu, Appl. Phys. Lett. **66**, 3024 (1995).
2. O. G. Schmidt, U. Denker, K. Eberl, *et al.*, Appl. Phys. Lett. **77**, 2509 (2000).
3. G. E. Cirlin, V. G. Talalaev, N. D. Zakharov, *et al.*, Phys. Status Solidi B **232**, R1 (2002).
4. G. E. Cirlin, P. Werner, U. Gösele, *et al.*, Pis'ma Zh. Tekh. Fiz. **27** (1), 31 (2001) [Tech. Phys. Lett. **27**, 14 (2001)].
5. V. G. Shengurov, P. Svetlov, V. Yu. Chalkov, *et al.*, Fiz. Tekh. Poluprovodn. (St. Petersburg) **36**, 662 (2002) [Semiconductors **36**, 625 (2002)].

Translated by P. Pozdeev

Technical Physics Letters, Vol. 29, No. 9, 2003, pp. 743–747. Translated from Pis'ma v Zhurnal Tekhnicheskoĭ Fiziki, Vol. 29, No. 17, 2003, pp. 86–94.

Anomalous Propagation of Elastic Waves through a Boundary between Liquid and Magnetoacoustic Material

M. M. Karpuk, D. A. Kostyuk, Yu. A. Kuzavko, and V. G. Shavrov

Politechnica Koszalinska, Raclavitskego 4, 75-620 Koszalin, Poland

Brest State Technical University, Brest, Belarus

Institute of Radio Engineering and Electronics, Russian Academy of Sciences, Fryazino, Moscow oblast, Russia

Revised manuscript received April 3, 2003

Abstract—We consider a longitudinal acoustic wave incident onto a plane boundary between a liquid and a magnetoacoustic medium representing an antiferromagnetic material with anisotropy of the easy plane type, occurring in the vicinity of an orientational phase transition with respect to magnetic field. The directions of propagation and the amplitudes of reflected and transmitted longitudinal and transverse waves are determined. The possibility of an effective field control for the refraction angle and the wave type transformation is demonstrated. Beginning with a certain critical angle of incidence, the longitudinal and, eventually, the transverse waves in the magnetic medium become inhomogeneous and slide along the interface. If the magnetic material is sufficiently close to the phase transition point, the waves can be reirradiated into the liquid medium. *© 2003 MAIK "Nauka/Interperiodica".*

When an elastic wave passes through a boundary between liquid and solid, there appear a reflected wave and two transmitted waves, the longitudinal (*LA*) and transverse (*TA*) ones (since only longitudinal waves can exist in the liquid [1]). At the same time, it is known that a magnetically ordered material in the vicinity of a point of orientational phase transition exhibit an increase in the magnetoelastic interaction that leads to a strong renormalization of the velocities of elastic waves [2]. Materials featuring this effect will be referred to as magnetoacoustic materials (MAMs). These include, in particular, antiferromagnetic materials with anisotropy of the easy plane (AFEP) type occurring in the vicinity of an orientational phase transition (OPT) with respect to magnetic field **H** applied in the basis (*xy*) plane of the crystal (**H** || **y**, the OPT point corresponds to $H = 0$). For example, the experimentally observed decrease in the transverse velocity of sound in AFEP-type crystals of hematite α-Fe_2O_3 amounted to 50% [3]. Previously [4], we studied the reflection of magnetoacoustic waves (MAWs) from the free surface of an AFEP type material and demonstrated the possibility of an effective field control for the refraction angle and the wave type transformation coefficient.

Consider a wave (LA_1) propagating from liquid medium 1 ($y > 0$) into MAM 2 ($y < 0$), making an angle α with the normal to the interface ($y = 0$) between the two media. Upon reflection, the incident wave transforms into LA_1 with the same angle of reflection, while the wave entering the second medium is transformed into MAWs LA_2 and TA_2 with the refraction angles β and γ, respectively.

In this consideration, the spin system can be explicitly ignored for the frequencies $\omega \ll \omega_{me} = \varepsilon_{me}/\hbar$, where $\varepsilon_{me} = g\sqrt{2H_E H_{me}}$ is the magnetoelastic gap in the spin wave spectrum, g is the gyromagnetic ratio, $\varepsilon_{1\mathbf{k}} = \sqrt{\Theta_N^2(ak)^2 + \varepsilon_M^2 + \varepsilon_{me}^2}$ is the low-frequency magnon energy, $\varepsilon_M = g\sqrt{H(H + H_D)}$ is the magnetic part of the gap, $\zeta = \varepsilon_{me}^2/\varepsilon_{1\mathbf{k}}^2$ is the magnetoelastic coupling parameter, H_E is the effective exchange field, H_D is the Dzyaloshinski field, H_{me} is the magnetostriction field, Θ_N is the Néel temperature, **k** is the wave vector, and a is the crustal lattice parameter. The magnetic material under consideration, possessing isotropic elastic and magnetoelastic properties, exhibits an anisotropy of the dynamic elastic moduli ("softening" of the elastic modulus c_{xyxy}) in the vicinity of the orientational phase transition. In particular, for hematite we have $H_E = 9.2 \times 10^6$ Oe, $H_D = 2.2 \times 10^4$ Oe, $H_{me} = 0.63$ Oe, and $\omega_{me} = 34$ GHz, so that the approximation adopted is satisfied in the entire experimental range of ultrasonic frequencies.

Below, we use the following expressions for the velocities of transverse and longitudinal wave veloci-

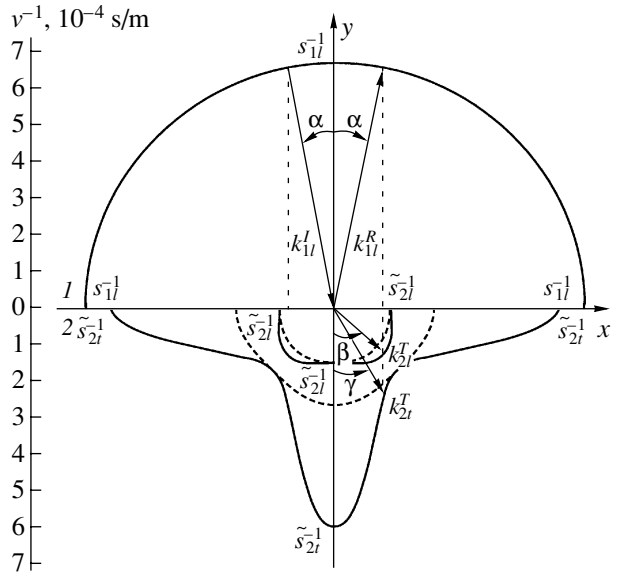

Fig. 1. Geometric construction of the wave vectors of the incident, reflected, and transmitted waves at the water–hematite interface. Solid and dashed curves correspond to H = 100 and 2000 Oe, respectively.

ties with allowance for the magnetoelastic coupling [5]:

$$\tilde{s}_{2t} = \sqrt{\frac{\mu_2}{\rho_2}(1-\zeta\cos^2 2\alpha)},$$
$$\tilde{s}_{2l} = \sqrt{\frac{\lambda_2+2\mu_2}{\rho_2}(1-n\zeta\sin^2 2\alpha)}, \quad (1)$$

where ρ_2 is the density, $n = \dfrac{\mu_2}{\lambda_2+2\mu_2} = \dfrac{s_{2t}^2}{s_{2l}^2}$, and λ_2 and μ_2 are the Lamé coefficients of the MAM studied. For hematite, s_{2t} = 4200 m/s, s_{2l} = 6760 m/s, ρ_2 = 5290 kg/m^3, and n = 0.386; for water, s_{1l} = 1500 m/s and ρ_1 = 1000 kg/m^3.

For the given direction, polarization, and amplitude of the incident wave and the known elastic properties of the media, we have to determine the directions of propagation, polarizations, and amplitudes of the reflected and transmitter waves. This problem is mathematically formulated by writing the equations of wave propagation in both media with the corresponding boundary conditions at the interface [1],

$$T^I_{l,yy} + T^R_{l,yy} = T^T_{t,yy} + T^T_{l,yy}, \quad u^I_{l,iy} + u^R_{l,iy} = u^T_{t,iy} + u^T_{l,iy}, \quad (2)$$

reflecting the continuity of elastic displacements u_i and normal components of the mechanical stresses T_{yy} (i = x, y). Here and below, the superscripts I, R, and T indicate the incident (longitudinal), reflected (LA_1), and transmitted (LA_2 and TA_2) waves.

In the case of plane harmonic incident, reflected, and transmitted (refracted) waves, the elastic displacements are as follows:

$$\begin{pmatrix} u^I_{1l,x} \\ u^I_{1l,y} \end{pmatrix} = u^I_{1l0}\begin{pmatrix} \sin\alpha \\ -\cos\alpha \end{pmatrix} \times \exp[i(k^I_{1l}x\sin\alpha - k^I_{1l}y\cos\alpha - \omega^I_{1l}t)],$$

$$\begin{pmatrix} u^R_{1l,x} \\ u^R_{1l,y} \end{pmatrix} = u^R_{1l0}\begin{pmatrix} \sin\alpha \\ \cos\alpha \end{pmatrix} \times \exp[i(k^R_{1l}x\sin\alpha + k^R_{1l}y\cos\alpha - \omega^R_{1l}t)],$$

$$\begin{pmatrix} u^T_{2t,x} \\ u^T_{2t,y} \end{pmatrix} = u^T_{2t0}\begin{pmatrix} \cos\gamma \\ \sin\gamma \end{pmatrix} \times \exp[i(k^T_{2t}x\sin\gamma - k^T_{2t}y\cos\gamma - \omega^T_{2t}t)], \quad (3)$$

$$\begin{pmatrix} u^T_{2l,x} \\ u^T_{2l,y} \end{pmatrix} = u^T_{2l0}\begin{pmatrix} \sin\beta \\ -\cos\beta \end{pmatrix} \times \exp[i(k^T_{2l}x\sin\beta - k^T_{2l}y\cos\beta - \omega^T_{2l}t)],$$

where u_0 and ω are the wave amplitudes and frequencies, respectively. According to the boundary conditions (2), at any time t we have $\omega^I_{1l} = \omega^R_{1l} = \omega^T_{2t} = \omega^T_{2l} = \omega$ and at any point in the y = 0 plane we have $k^I_{1l,x} = k^R_{1l,x} = k^T_{2t,x} = k^T_{2l,x} = k_x$. For the above conditions, the directions of wave propagation are determined by the relations

$$\frac{\sin\alpha}{s_{1l}} = \frac{\sin\gamma}{\tilde{s}_{2t}(\gamma)} = \frac{\sin\beta}{\tilde{s}_{2l}(\beta)} \quad (4)$$

and can be found graphically by constructing the surfaces of inverse phase velocities of the corresponding waves as depicted in Fig. 1. Equations (4) yield the following expressions for the refraction angles of waves LA_2 and TA_2 in the second medium:

$$\sin^2\beta = \frac{4\zeta n\sin^2\alpha + b - \sqrt{(4\zeta n\sin^2\alpha + b)^2 - 16\zeta n\sin^4\alpha}}{8\zeta n\sin^2\alpha}, \quad (5)$$

$$= \frac{\sin^2\gamma}{\dfrac{4\zeta\sin^2\alpha - c + \sqrt{(4\zeta\sin^2\alpha - c)^2 - 16\zeta(1-\zeta)\sin^4\alpha}}{8\zeta\sin^2\alpha}}, \quad (6)$$

where $b = \dfrac{s_{1l}^2}{s_{2l}^2}$ and $c = \dfrac{s_{1l}^2}{s_{2t}^2}$. Upon the limiting transition $\zeta \longrightarrow 0$, formulas (5) and (6) convert into the conventional Snell's law. These considerations were used to select the signs of the square roots in formulas (5) and (6). It should be noted that, for $\zeta > 1/(4n)$ ($\zeta \approx 0.648$ and $H = 283$ Oe for the water–hematite interface), the surface of the inverse phase velocity exhibits a concavity leading to the appearance of the second solution for the angle of refraction β for the longitudinal wave (5) with the sign "+" at the square root. This solution corresponds to a refracted longitudinal wave with a group velocity directed toward the interface [6].

Liquids are virtually always characterized by $s_{1l} < s_{2t}$, s_{2l} and an analysis of formulas (4)–(6) shows that there are two critical angles of incidence, α_{1cr} and α_{2cr}, such that the MAW LA_2 for $\alpha > \alpha_{1cr} = \arcsin b^{1/2}$ LA_2 propagates along the interface; then, for $\alpha > \alpha_{2cr} = \arcsin[c/(1-\zeta)]^{1/2}$, the same is observed for the MAW TA_2. Therefore, the threshold angle of the total internal reflection for LA_1 at $\alpha > \alpha_{2cr}$ is controlled by the external magnetic field [7].

Figure 2 shows the plots of refraction angles β and γ versus the incident angle α constructed according to formulas (5) and (6) for various degrees of proximity to the OPT point. As can be seen, variation of the magnetic field H provides for an effective control of the angle of refraction, especially for the transverse MAW propagating in MAM, the velocity of which tends to zero at the OPT point. Note also that, for the angle of incidence $\alpha = \arcsin\sqrt{e/2} \approx 15°$ (when $\gamma = 45°$), the angle of refraction for TA_2 is independent of the field, while that for LA_2 can vary within broad limits.

Substituting expressions (3) into the boundary conditions (2), we determine the amplitude reflection coefficient of the incident wave LA_1,

$$R_{ll} = \frac{u_{1l0}^R}{u_{1l0}^I} = \frac{A-B}{A+B}, \quad (7)$$

and the amplitude transformation coefficients for the refracted waves LA_2 and TA_2,

$$T_{ll} = \frac{u_{2l0}^T}{u_{1l0}^I} = \frac{C}{A+B}, \quad T_{lt} = \frac{u_{2t}^T}{u_{1l0}^I} = \frac{D}{A+B}, \quad (8)$$

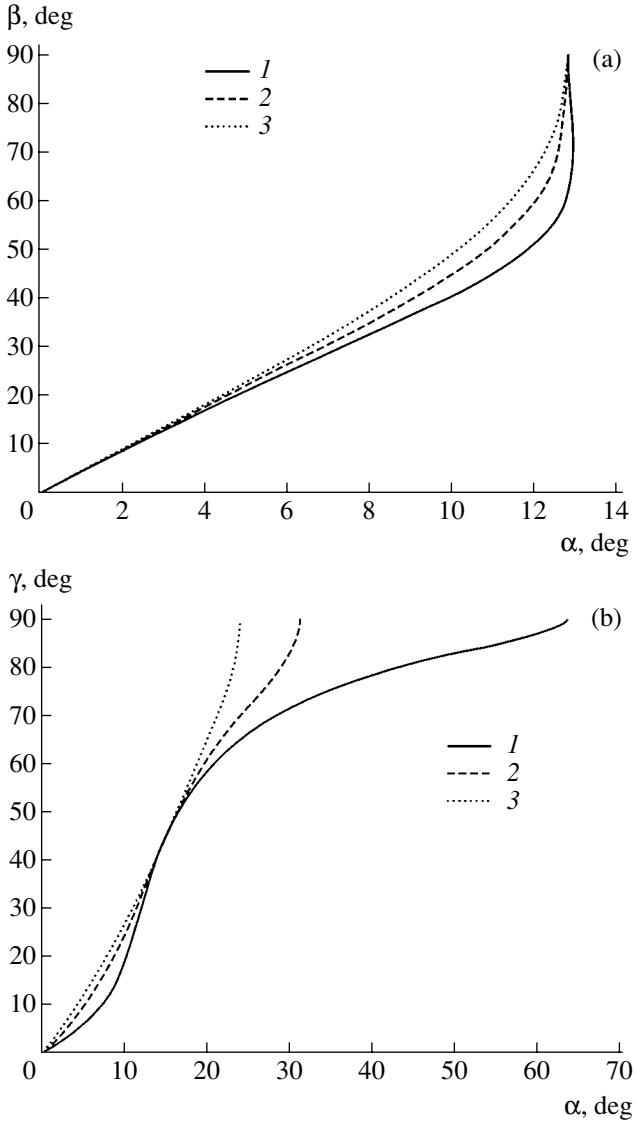

Fig. 2. Plots of the angles of refraction (a) β (for the MAW LA_2) and (b) γ (for the MAW TA_2) versus the angle of the LA_1 wave incidence α onto the water–hematite interface at $H = 100$ Oe ($\zeta = 0.840$) (*1*), 500 Oe ($\zeta = 0.507$) (*2*), and 2000 Oe ($\zeta = 0.194$) (*3*).

where

$$A = [(\lambda_2 + 2\mu_2\cos^2\beta)\tilde{s}_{2l}^{-1}\cos\gamma - \mu_2\tilde{s}_{2t}^{-1}\sin 2\gamma\sin\beta]\cos\alpha,$$

$$B = \lambda_1 s_{1l}^{-1}(\sin\beta\sin\gamma + \cos\beta\cos\gamma) + \mu_2\tilde{s}_{2t}^{-1}\sin\alpha\cos\beta\sin 2\gamma - (\lambda_2 + 2\mu_2\cos^2\beta)\tilde{s}_{2l}^{-1}\sin\alpha\sin\gamma],$$

$$C = 2\lambda_1 s_{1l}^{-1}\cos\alpha\cos\gamma + \mu_2\tilde{s}_{2t}^{-1}\sin 2\gamma\sin 2\alpha,$$

$$D = -2\lambda_1 s_{1l}^{-1}\cos\alpha\sin\beta + (\lambda_2 + \mu_2\cos^2\beta)\tilde{s}_{2l}^{-1}\sin 2\alpha.$$

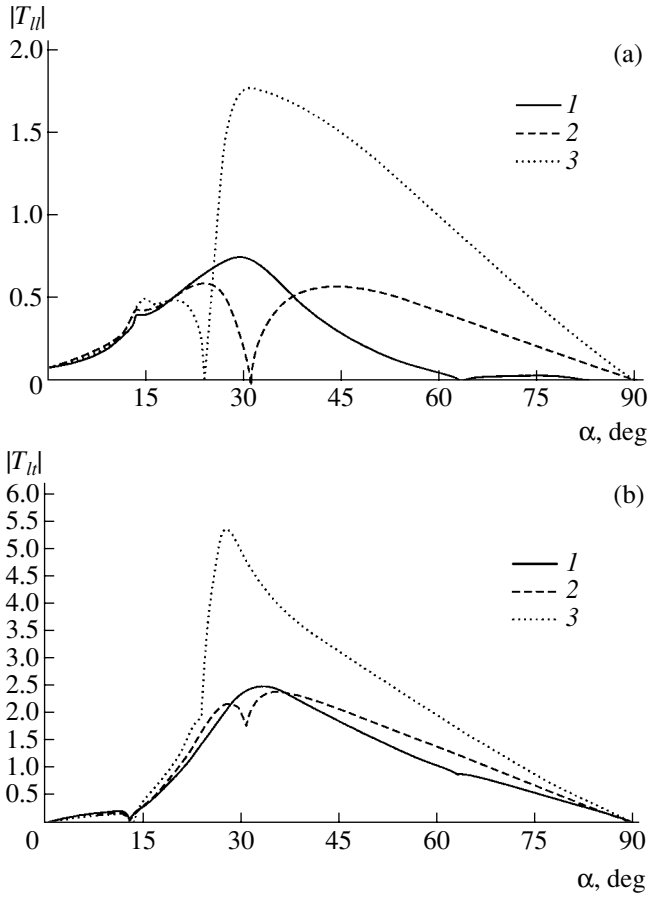

Fig. 3. Plots of the absolute values of the coefficients of the *LA* wave (a) transmission T_{ll} and (b) transformation T_{lt} (into TA_2 wave) versus the angle of the LA_1 wave incidence α onto the water–hematite interface at H = 100 Oe (ζ = 0.840) (*1*), 500 Oe (ζ = 0.507) (*2*), and 2000 Oe (ζ = 0.194) (*3*).

For $\alpha > \alpha_{1cr}$, the MAW LA_2 propagating along the interface becomes inhomogeneous. For this wave, the velocity $\tilde{s}'_{2l}$ and the penetration depth Λ_{2l} ($u_{2l} \sim e^{y/\Lambda_{2l}}$) in the MAM begin to depend on the incident angle α:

$$\tilde{s}'_{2l} = \frac{s_{1l}}{\sin\alpha}, \quad \Lambda_{2l} = \frac{s_{1l}}{\omega\sqrt{\sin^2\alpha - b}}. \tag{9}$$

For $\alpha > \alpha_{2cr}$, the MAW TA_2 also propagates along the interface and becomes inhomogeneous. For this wave, the velocity $\tilde{s}'_{2t}$ is given by the corresponding formula (9) with substitution $s_{2l} \longrightarrow s_{2t}$ and

$$\Lambda_{2t} = \frac{s_{1l}s_{2t}\sqrt{1 - \zeta\cos^2 2\gamma}}{\omega s_{2l}\sqrt{\sin^2\alpha - b}}. \tag{10}$$

An analysis of expressions (5) and (6) shows that, because of a strong deformation of the inverse phase velocity surface in the MAM, there is a certain threshold ζ* such that for ζ > ζ* the system exhibits a new effect, whereby the sliding wave is reirradiated into the volume of liquid. The corresponding critical angle $\alpha_{cr} = \arcsin\sqrt{\frac{b}{4\chi(1-\chi)}}$ (where $\chi = (\zeta n)^{1/2}$) depends on the degree of proximity to the OPT point. It is easy to show that the minimum value of α_{cr} corresponds to χ = 0.5, whereby ζ = 1/(4*n*) and $\alpha_{cr} = \arcsin(b^{1/2})$. Thus, in all cases $\alpha_{cr1} \le \alpha_{cr} \le \alpha_{cr1}$. For ζ* = [2 – *b* – 2(1 – *b*)$^{1/2}$]/4, we obtain $\alpha_{cr} = 90°$ and, as the magnetoelastic coupling parameter ζ increases further, the critical angle decreases (to attain ζ = 1 a value of $\alpha_{cr} = 19.8°$ for the water–hematite interface). For $\alpha = \alpha_{cr}$, the expression under the radical in formula (5) is zero and for $\alpha > \alpha_{cr}$ it is negative, so that sinβ formally becomes complex. Physically, this implies that the sliding wave goes from the interface toward the volume of liquid and exhibits damping, which increases with a distance from the interface. Note that this damping is nondissipative and characterizes the structure of a new oscillatory process taking place in the vicinity of the interface.

Figure 3 shows the plots of T_{ll} and T_{lt} versus incident angle α calculated using formulas (7) and (8) fir the water–hematite system. According to these calculations, $\alpha = \alpha_{1cr} = 14.2°$ yields β = 90° for the MAW LA_2 and $\alpha = \alpha_{2cr} = 24.1°$ (ζ = 0) yields γ = 90° for the MAW TA_2. Note that, for $\alpha \approx 90°$, there is a sharp increase in the reflected wave amplitude. This is explained by inhomogeneity of the LA_2 and TA_2 waves in the region of $\alpha > \alpha_{1cr}$ related to the wave energy localization immediately at the interface. In the interval of incident angles $\alpha_{cr1} \le \alpha \le \alpha_{cr}$, there is a decrease in the coefficients of reflection R_{ll}, transmission T_{ll}, and transformation T_{lt} related to the pumping of energy from LA_1 to the transmitted wave with reirradiation into the liquid volume. Thus, a strongly anisotropic elasticity of the crystal induced by the magnetoelastic interaction in the MAM (hematite) in the vicinity of the OPT accounts for the anomalous total internal reflection of the incident LA_1 wave, the appearance of sliding and reirradiated boundary waves, and their magnetic-field-controlled critical behavior. Experimental observation of these phenomena in MAMs is quite possible, in contrast to the impossibility of detecting such effects in usual acoustical crystals possessing insufficiently high anisotropy.

Acknowledgments. This study was supported in part by the Foundation for Basic Research of the Republic of Belarus and by the Russian Foundation for

Basic Research (project nos. T02M-137, F02-076R, and 02-02-81030Bel2002-a).

REFERENCES

1. E. Dieulesaint and D. Royer, *Elastic Waves in Solids* (Wiley, New York, 1981; Nauka, Moscow, 1982).
2. E. A. Turov and V. G. Shavrov, Usp. Fiz. Nauk **140**, 429 (1983) [Sov. Phys. Usp. **26**, 593 (1983)].
3. E. A. Andryushchak, N. N. Evtikhiev, S. A. Pogozhev, and V. L. Preobrazhenskiĭ, Akust. Zh. **27**, 170 (1981) [Sov. Phys. Acoust. **27**, 93 (1981)].
4. Yu. A. Kuzavko and V. G. Shavrov, Akust. Zh. **39**, 1088 (1993) [Acoust. Phys. **39**, 572 (1993)].
5. Yu. Kuzavko, H. Roth, and V. Golovko, in *Proceedings of the Workshop on Design Methodologies for Signal Processing, Zakopane, 1996*, pp. 131–135.
6. M. K. Balakirev and I. A. Gilinskiĭ, *Waves in Piezoelectric Crystals* (Nauka, Novosibirsk, 1982).
7. Y. A. Kuzavko and M. M. Karpuk, in *Book of Abstracts of the 17th International Congress on Acoustics, Rome, 2001*.

Translated by P. Pozdeev

Technical Physics Letters, Vol. 29, No. 9, 2003, pp. 748–749. Translated from Pis'ma v Zhurnal Tekhnicheskoĭ Fiziki, Vol. 29, No. 18, 2003, pp. 1–5.

Effect of Gamma Radiation on the Characteristics of Gallium Nitride HEMT Heterostructures

A. M. Kurakin

Institute of Semiconductor Physics, National Academy of Sciences of Ukraine, Kiev, Ukraine
e-mail: Andrey.Kurakin@mail.ru

Received April 1, 2003

Abstract—The influence of gamma radiation from a Co^{60} source on some characteristics of AlGaN/GaN HEMT heterostructures has been studied. The dose dependence of the total source and drain resistances is determined using a modified graphical-analytical method for calculation of the characteristic resistances of HEMTs. The contacts exhibit a significant radiation-stimulated degradation, which detrimentally affects the transistor operation and may account for the observed decrease in HEMT characteristics such as the saturation current and the transconductance. © *2003 MAIK "Nauka/Interperiodica".*

Taking into account that semiconductor materials belonging to group III nitrides are serious competitors to GaAs and SiC in devices of high-temperature and ultrahigh-power microwave electronics, it is very important to study degradation of the former materials under the action of ionizing radiation. Such investigations are of interest both from the standpoint of determining the defect structure of such materials and as a method of evaluating the reliability of device operation.

This study is devoted to high electron mobility transistors (HEMTs) based on nominally undoped heterostructures of the AlGaN/GaN type comprising a 23-nm-thick $Al_{0.33}Ga_{0.67}N$ barrier layer, a 1100-nm-thick GaN buffer layer, and a 40-nm-thick $Al_{0.14}Ga_{0.86}N$ nucleation layer grown on a sapphire substrate. The transistors had a channel width of 200, 250, 300, and 400 μm; the gate, with a length variable between 150 and 350 nm, was spaced from the drain and source by 1 and 2 μm, respectively. The room-temperature charge carrier density and mobility in the channel were 1.05×10^{13} cm^{-2} and 1250 cm^2/(V s), respectively.

The samples were irradiated at room temperature by gamma radiation from a Co^{60} source at an intensity of ~100 P/s and a total dose of up to 10^8 rad. The sample temperature during the exposure did not exceed 40°C. The parameters of transistors were determined by measuring their current–voltage characteristics within several hours after each exposure.

The resistance of a completely open HEMT channel and the total source–drain resistance of the Schottky gate transistor can be determined using a graphical-analytical method [1], according to which the above resistances of transistors are calculated based on the experimentally measured drain–gate characteristics. Although the original method offers a convenient means of experimental data processing, the procedure has to be modified so as to make it applicable to some important modern devices, including HEMTs. The changes primarily involve the analytical expression for the characteristic resistance of the transistor channel.

Consider an analytical expression for the current–voltage characteristic of HEMT [2],

$$\frac{IL_{\text{eff}}}{A} = \left(V_G - V_{\text{off}} - \frac{I}{AE_C}\right)(V_{DS} - I(R_S + R_D)) - \frac{1}{2}\{(V_{DS} - IR_D)^2 - I^2R_S^2\}, \quad (1)$$

where I is the device current, L_{eff} is the effective width of the depletion region, $A = \mu\varepsilon W/(d + \Delta d)$, μ is the carrier mobility in the channel, ε is the barrier permittivity, d is the barrier layer thickness, W is the channel width, Δd is the effective thickness of a two-dimensional electron gas (2DEG) region, V_G is the gate voltage, V_{off} is the channel blocking voltage, E_C is the critical electric field strength, V_{DS} is the drain–source voltage, and R_D and R_S are the drain and source contact resistances, respectively.

Using relation (1), it is possible to find the derivative dI/dV_{DS} and, after some transformations, an expression for the total HEMT resistance in the approximation of $2(V_G - V_{\text{off}}) \gg V_{DS}$:

$$R_{\text{tot}} = \frac{L}{A(V_G - V_{\text{off}} - V_{DS})} + (R_S + R_D)\left(1 + \frac{V_{DS}}{2(V_G - V_{\text{off}} - V_{DS})}\right). \quad (2)$$

Within the framework of this study, the total HEMT resistances were determined using the experimentally measured current–voltage characteristics. The source and drain resistances before and after gamma irradiation of the samples were calculated using formula (2).

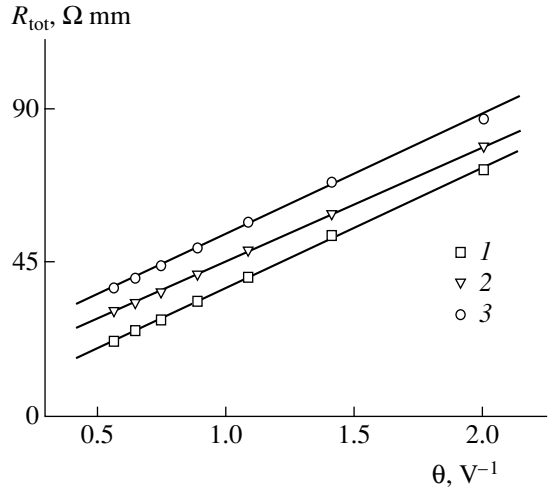

Fig. 1. Typical plots of the total resistance versus parameter θ for a HEMT heterostructure (*1*) before gamma irradiation and (*2*, *3*) after irradiated to a total dose of 10^6 and 10^8 rad, respectively.

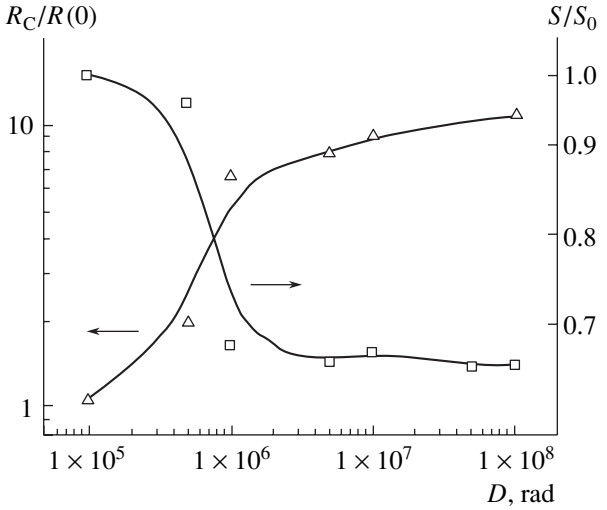

Fig. 2. Plots of the relative contact resistance and the transconductance versus total gamma irradiation dose for an AlGaN/GaN based HEMT heterostructure with a channel width of W = 200 μm and a gate length of L_G = 0.25 μm.

Figure 1 shows typical plots of the total resistance of a HEMT structure versus parameter $\theta = 1/(V_G - V_{off} - V_{DS})$ for V_{DS} = 0.1 V. The linearity of these plots indicates that the approximate relation (2) adequately describes a change in the total HEMT resistance with the gate voltage.

The proposed graphical-analytical method gives somewhat overstated values of the contact resistances. Indeed, the values calculated for a HEMT structure with W = 200 μm and L_G = 0.25 μm before and after irradiation to a total dose of 10^6 rad (1.6 and 10.4 Ω mm, respectively) exceed the values measured using the TLM patterns with W = 150 μm (1.2 and 6.9 Ω mm, respectively), which can be explained by a nonzero contribution of the ohmic resistance of the transistor base.

It has to be noted that the contact resistances of the HEMT structures studied exhibit significant degradation even at relatively low doses of gamma irradiation (~10^6 rad). Despite this, the HEMT samples retained the ability to operate up to a total dose of 10^8 rad, which agrees with the results reported in [3]. Correlations observed in behavior of the dose dependences of the total contact resistance and the transconductance (Fig. 2) show that data obtained using the proposed method correctly reflect changes in the contact resistances in the course of the radiation-stimulated degradation of the HEMT structure.

Thus, the results of this investigation indicate that the graphical-analytical method of calculation of the characteristic resistances has good prospects for application to determining the reliability of the contacts of HEMT transistors and evaluating their characteristic resistances. As is known, the properties of contacts determine the noise characteristics of devices and, according to the general theory of HEMTs [2], the transconductance depends on the total contact resistance. Taking into account a significant degradation of the ohmic contacts of the HEMT source and drain, it can be ascertained that the quality of source and drain contacts determines to a considerable extent the reliability of HEMT operation under the conditions of continuous gamma irradiation.

Acknowledgments. The author is grateful to Prof. R.V. Konakova and Prof. A.E. Belyaev for making this investigation possible.

REFERENCES

1. S. G. Morozov, N. S. Spiridonov, and A. D. Tuz, Élektron. Tekh., Ser. Élektron. SVCh, No. 2, 100 (1987).
2. *Molecular Beam Epitaxy and Heterostructures*, Ed. by L. L. Chang and K. Ploog (Martimus Nishoff, Amsterdam, 1985; Mir, Moscow, 1989).
3. S. A. Vitusevich, N. Klein, A. E. Belyaev, *et al.*, Phys. Status Solidi A **195**, 101 (2003).

Translated by P. Pozdeev

Technical Physics Letters, Vol. 29, No. 9, 2003, pp. 750–751. Translated from Pis'ma v Zhurnal Tekhnicheskoĭ Fiziki, Vol. 29, No. 18, 2003, pp. 6–10.

Static and Pulsed Pressures Measured Using Electrically Conducting Rubbers

J. N. Aneli, V. P. Kortkhondzhiya, and M. M. Bolotashvili

Institute of Machine Mechanics, Academy of Sciences of Georgia, Tbilisi, Georgia

e-mail: georgeng@ip.osgf.ge

Received January 14, 2003; in final form, March 17, 2003

Abstract—A method of measuring static and pulsed pressures using electrically conducting rubber sensors is proposed. The method is based on a change in the volume resistivity of a filled rubber under the action of external pressure. The pressure-induced change in resistance of the rubber sensor is proportional to the applied pressure and can be measured by a bridge circuit. Using this method, it is possible to evaluate the degree of homogeneity of the pressure distribution over a solid surface. This is achieved by distributing rubber sensors over the given surface. *© 2003 MAIK "Nauka/Interperiodica".*

Presently, various methods (mechanical, electrical, magnetic, etc.) are used for measuring pressures in both static and dynamic regimes [1]. However, most of these methods require complicated equipment. Widely used strain gauges based on metal alloys [2], while possessing many advantages, still have a common drawback of relatively low sensitivity (typically about 2–2.5) limiting the field of possible applications. In addition, metal strain gauges are characterized by low corrosion resistance, hindering their operation in aggressive media. Alternative strain gauges based on piezoelectric crystals are also capable of measuring both static and pulsed pressures [3] and possess a high sensitivity. However, a significant disadvantage of these devices is related to the following fact. A pressure pulse (with a duration on the order of several milli- or microseconds) applied to one face of the crystal gives rise to an acoustic wave that propagates in the crystal, reflects from the opposite face, and returns back. This leads to considerable distortion of the useful signal as a result of superposition of the incident and reflected waves. In most cases, the pressure in such systems is measured using an auxiliary device that leads to certain technical problems. Thus, the measurement of pressures by means of piezoelectric crystals requires special equipment and highly qualified operators.

As is known [4], a dielectric rubber containing electrically conducting fillers (technical carbon, graphite, metal powders) at a concentration above a certain limit (corresponding to the so-called percolation phase transition of the dielectric–conductor type [5]) becomes electrically conducting. As the content of such a filler increases, the conductivity grows up to a certain limiting value. As a rule, electrically conducting rubbers are sensitive to deformation. The level of this sensitivity can be controlled by selecting the type of components, by varying their content, and by using various physical factors influencing the material structure formation [6].

In this paper, we propose a new method of measuring static and pulsed pressures using electrically conducting rubber sensors.

The experiments were performed with electrically conducting composites based on a silicon rubber of the SKTV grade filled with a technical carbon (MPE-100V grade). By varying the filler concentration and the vulcanization conditions, we obtained a series of conducting rubbers with the following characteristics:

Volume resistivity ρ_v, Ω cm	0.5–5
Temperature coefficient of resistance, K^{-1}	0.004
Strain gauge factor	2–40
Modulus of elasticity, MPa	2–6
Creep, %	0.8–1
Strain range, %	10^{-5}–10^{-2}

The rubbers were characterized by a low level of noises and residual phenomena under cyclic loading conditions.

Using the synthesized conducting rubbers, we manufactured samples in the form of disks with a diameter of 10–20 mm and a thickness of up to 2 mm. The disks were coated with a thin metal layer from both sides by deposition in vacuum. For the pressure measurements, a metallized rubber sample was placed onto a ground flat metal plate, a copper disk of the same diameter was placed above, and this element was connected to a measuring bridge circuit. The element was excited by an acoustic wave, the pressure of which caused variations in the electric resistance of the rubber. These variations lead to corresponding changes (proportional to the value of deformation) in the voltage drop across the

1063-7850/03/2909-0750$24.00

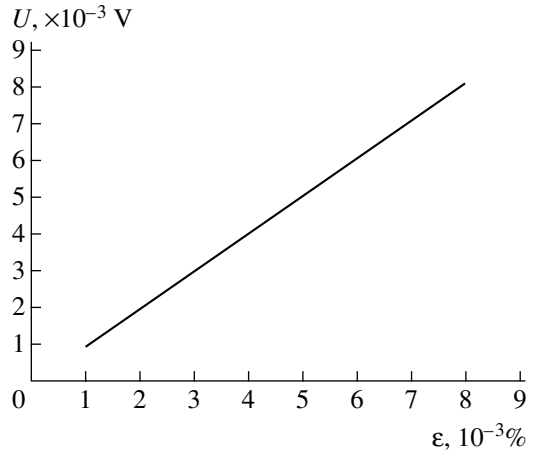

Fig. 1. A plot of the output voltage versus strain for a conducting rubber sensor (ρ_v = 4.2 Ω cm).

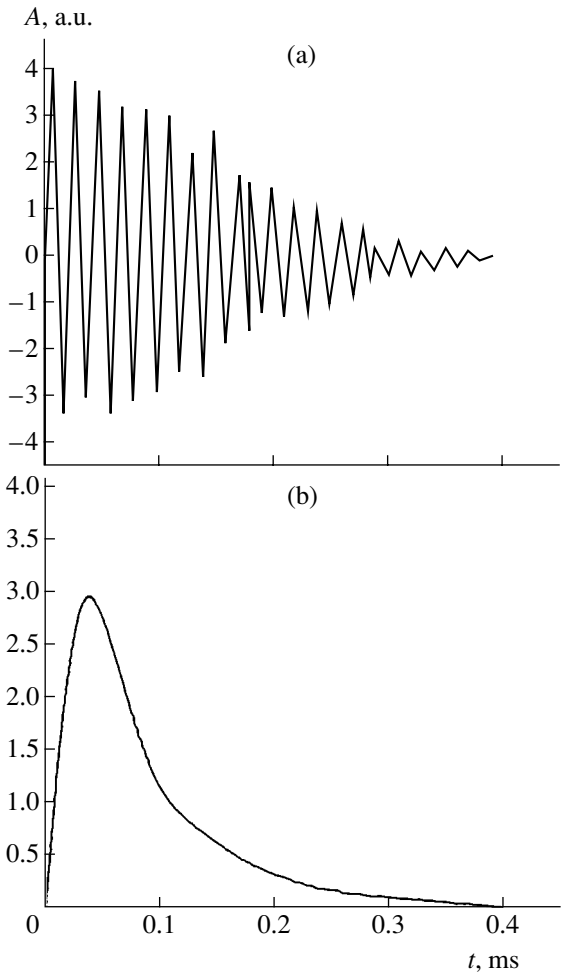

Fig. 2. Typical oscillograms of the pressure pulse amplitude measured with (a) a commercial crystal strain gauge and (b) a conducting rubber sensor.

rubber disk, which are measured by the bridge and displayed by an oscillograph.

Figure 1 shows a plot of the output voltage versus mechanical load (strain amplitude) for a rubber-based pressure sensor. As can be seen, the plot is linear, which is very important for a strain gauge.

In order to assess the efficacy of measuring pulsed pressures by means of electrically conducting rubber sensors, we performed comparative experiments using such sensors and commercial strain gauges. Figure 2 shows typical oscillograms reflecting variations of the pressure pulse amplitude. As can be seen from these patterns, the output signal of a rubber sensor exhibits a monotonic decrease with time, while the signal of the strain gauge is lost in the interfering signals. A series of measurements showed that the peak on the oscillogram of the signal from the rubber sensor is directly proportional to the pressure produced by the incident shock wave.

Using the strain gauges with electrically conducting rubber sensors, it is possible to perform large-scale measurements for determining the degree of homogeneity of the pressure distribution over a flat solid surface. For this purpose, the rubber sensors are distributed over this surface and their output leads are connected to a multichannel measuring system (e.g., analog-to-digital converter linked to a computer). The signal from each sensor being proportional to the pressure acting upon the corresponding area, the pattern of signals measured from all sensors will reflect the distribution of pressure over the given surface.

REFERENCES

1. A. M. Turichin, *Electrical Measurements of Nonelectrical Quantities* (Énergiya, Moscow, 1966).
2. G. Ya. Pochtovik and A. B. Zlochevskiĭ, *Building Constructions: Test Methods and Facilities* (Vysshaya Shkola, Moscow, 1973).
3. *Plasma Physics and Thermonuclear Research*, Ed. by M. Leontovich (Pergamon Press, Oxford, 1959; Izd. Akad. Nauk SSSR, Moscow, 1958), Vol. 1.
4. V. E. Gul and L. Z. Shenfil, *Conducting Polymer Compositions* (Khimiya, Moscow, 1984).
5. F. L. Shklovskiĭ and M. E. Éfros, *Physics of Doped Semiconductors* (Nauka, Moscow, 1976).
6. J. N. Aneli, L. M. Khananashvili, and G. E. Zaikov, *Structuring and Conductivity of Polymer Composites* (Nova Science, New York, 1998).

Translated by P. Pozdeev

Technical Physics Letters, Vol. 29, No. 9, 2003, pp. 752–753. Translated from Pis'ma v Zhurnal Tekhnicheskoĭ Fiziki, Vol. 29, No. 18, 2003, pp. 11–15.

New Stationary Structures in an Acoustically Active Medium

V. G. Makaryan and N. E. Molevich*

Samara State Aerospace University, Samara, Russia

**e-mail: molevich@mb.ssau.ru*

Received March 31, 2003

Abstract—We have studied for the first time the solutions of an equation describing the evolution of an acoustic perturbation with arbitrary spectral composition in a nonequilibrium medium with negative viscosity. The corresponding stationary structures are analytically and numerically determined. A condition of instability for perturbations of the step type is found. It is shown that a stationary shock wave pulse can exist in an acoustically active medium of this kind. © *2003 MAIK "Nauka/Interperiodica".*

As is known, thermodynamically nonequilibrium media such as a vibrationally excited gas, nonisothermal plasma, or chemically active mixtures may exhibit inversion of the second (volume) viscosity coefficient [1]. A medium possessing negative viscosity is acoustically active. Such media can feature stationary structures substantially different from the shock wave structures of the step type with a monotonic front. Until now, these structures have been studied using nonlinear equations obtained in the second- or third-order gasdynamic approximation separately for the low- and high-frequency perturbations. Examples are offered by the Kuramoto–Sivashinsky equation or the modified Korteweg–de Vries–Burgers equation with nonlinear viscosity (obtained in a low- frequency approximation) and by the Burgers equation with a source and integral dispersion (high-frequency approximation). A disadvantage of this approach is the impossibility of describing the nonstationary evolution of perturbations with arbitrary spectrum using the above equations. Moreover, the spectrum of stationary structures described by these equations is broader than their domain of applicability.

Previously [2], an equation was obtained,

$$C_{V\infty}\tau_0\left(v_{tt} - u_\infty^2 v_{xx} - u_\infty \Psi_\infty v_{xx}^2 - \frac{\mu_\infty}{\rho_0} v_{xxt}\right)_t + C_{V0}\left(v_{tt} - u_0^2 v_{xx} - u_0 \Psi_0 v_{xx}^2 - \frac{\mu_0}{\rho_0} v_{xxt}\right) = 0, \quad (1)$$

that described (to within the second-order terms in the amplitude) the nonlinear evolution of an acoustic perturbation with arbitrary spectrum in a nonequilibrium gas featuring a relaxation process of the type

$$\frac{dE}{dt} = \frac{E_{\text{eq}} - E}{\tau} + Q.$$

In the case of a vibrationally excited gas, E is the energy of the vibrational degrees of freedom, E_{eq} is the corresponding equilibrium value, τ is the vibrational relaxation time, and Q is the power of a pumping source maintaining thermodynamic nonequilibrium in the system. In Eq. (1), $u_\infty = \sqrt{C_{P\infty}T_0/C_{V\infty}m}$ and $u_0 = \sqrt{C_{P0}T_0/C_{V0}m}$ are the high- and low-frequency sound velocities, respectively; $C_{V0} = C_{V\infty} + C_K + S\tau_T$ and $C_{P0} = C_{P\infty} + C_K + S(\tau_T + 1)$ are the stationary (low-frequency) heat capacities of the vibrationally-excited gas at a constant volume and pressure, respectively [1] ($C_{V\infty}$ and $C_{P\infty}$ are the corresponding high-frequency values); T_0, ρ_0, and τ_0 are the unperturbed gas temperature, density, and relaxation time, respectively; m is the molecular mass; $S = Q\tau_0/T_0$ is the degree of nonequlibrium of the medium; $C_K = (dE_e/dT)_{T=T_0}$ is the equilibrium vibrational heat capacity; $\tau_T = \partial\ln\tau_0/\partial\ln T_0$; $\Psi_\infty = (\gamma_\infty + 1)/2$ is the high-frequency quadratic nonlinearity coefficient; Ψ_0 is the low-frequency quadratic nonlinearity coefficient depending on the degree of nonequilibrium S (for $S = 0$, this coefficient has a simple form of $\Psi_0 = (\gamma_0 + 1)/2$ [1]); $\gamma_\infty = C_{P\infty}/C_{V\infty}$; $\gamma_0 = C_{P0}/C_{V0}$; $\mu_\infty = 4\eta/3 + \chi m(1/C_{V\infty} - 1/C_{P\infty})$ and $\mu_0 = 4\eta/3 + \chi m(1/C_{V0} - 1/C_{P0})$ are the high- and low-frequency viscosity–thermal conductivity coefficients, respectively. Equation (1) was obtained in the approximation of small dispersion, that is, for $\tilde{m} = (u_\infty^2 - u_0^2)/u_\infty^2 \sim \theta \ll 1$.

For the waves traveling in the same direction ($\tilde{v} = v/u_\infty$, $\zeta = (x - u_\infty t)/u_\infty\tau_0$, $y = \theta t/\tau_0$, $\theta \ll 1$), Eq. (1) acquires the following form:

$$\left(\tilde{v}_y + \frac{\Psi_\infty}{2}\tilde{v}_\zeta^2 - \tilde{\mu}_\infty \tilde{v}_{\zeta\zeta}\right)_\zeta - \frac{C_{V0}}{C_{V\infty}}\left(\tilde{v}_y - \frac{C_{V0}}{C_{V\infty}}\tilde{\zeta}\tilde{v}_\zeta + \frac{\Psi_0}{2}\tilde{v}_\zeta^2 - \tilde{\mu}_0\tilde{v}_{\zeta\zeta}\right) = 0, \quad (2)$$

1063-7850/03/2909-0752$24.00 © 2003 MAIK "Nauka/Interperiodica"

where $\tilde{\mu} = \mu/2\tau u_\infty^2 \rho_0$, $\tilde{\xi} = C_{V\infty}\tilde{m}/2C_{V0}$ is the dimensionless coefficient of second viscosity. For $S = 0$, Eq. (2) coincides with the well-known relaxation equation [3] (except that the latter equation does not take into account the difference between μ_0, Ψ_0 and μ_∞, Ψ_∞). Note also that, in the low- and high-frequency approximations, Eq. (2) readily yields the Kuramoto–Sivashinsky equation and the Burgers equation with a source.

In this study, we used numerical and analytical methods to obtain solutions of Eq. (2) that are valid in an arbitrary spectral range. We consider a medium with negative total viscosity coefficient, $\tilde{\mu}_\Sigma = \tilde{\xi} + \tilde{\mu}_0 < 0$, and assume that $C_{V0} > 0$, $\Psi_0 > 0$, and $\Psi_\infty > \Psi_0$. The initial perturbation had the form a step of amplitude $\tilde{v}_1$. For $\tilde{v}_1 > \tilde{v}_{cr}$, the perturbation exhibits a monotonic growth behind the step (Fig. 1, curve *1*). At $\tilde{\mu}_\infty \ll 1$, the critical velocity is $\tilde{v}_{cr} \approx 2|\tilde{\mu}_\Sigma|C_{V0}/(\Psi_\infty - \Psi_0)C_{V\infty}$. Such a rounded front is typical of relaxing media with $\tilde{\mu}_\Sigma > 0$ and predominating nonlinear effects [3]. In the case of $\tilde{v}'_{cr} < \tilde{v}_1 < \tilde{v}_{cr}$, where $\tilde{v}'_{cr} = 2|\tilde{\mu}_\Sigma|C_{V0}/C_{V\infty}(2\Psi_\infty - \Psi_0)$, the step transforms into a stationary structure as depicted in Fig. 1 (curve *2*). For $\tilde{v}_1 < \tilde{v}'_{cr}$, the step becomes unstable and decays into a periodic sequence of stationary pulses. The pulse shape is depicted in Fig. 2.

The aforementioned stationary structures can also be obtained upon solving Eq. (2) in an automodel ($z = \zeta - W\tilde{y}$) form:

$$\tilde{v}_{zz} + \tilde{v}_z\left[\left(\frac{W}{\tilde{\mu}_\infty} - \frac{C_{V0}\tilde{\mu}_0}{C_{V\infty}\tilde{\mu}_\infty}\right) - \frac{\Psi_\infty}{\tilde{\mu}_\infty}\tilde{v}\right]$$

$$+ \frac{C_{V0}}{\tilde{\mu}_\infty C_{V\infty}}\left[-(W + 0.5\tilde{m})\tilde{v} + \frac{\Psi_0}{2}\tilde{v}^2\right] = 0.$$

For example, the stationary pulse in Fig. 2 corresponds to the motion along a separatrix on the ($\tilde{v}_z$, $\tilde{v}$) phase plane. For $|\tilde{\mu}_\Sigma|/\tilde{\mu}_\infty \gg 1$, the pulse has a leading shock wave front with a width of $\sim C_{V\infty}\tilde{\mu}_\infty(2\Psi_\infty - \Psi_0)/2C_{V0}|\tilde{\mu}_\Sigma|\Psi_\infty$ and a trailing front exponentially decaying with an decrement of $\sim C_{V0}\Psi_0/2C_{V\infty}\Psi_\infty$. With neglect of the $\tilde{\mu}_\infty$ value, the pulse amplitude and propagation velocity are as follows:

$$\tilde{v}_{im} = \frac{4|\tilde{\mu}_\Sigma|C_{V0}}{C_{V\infty}(2\Psi_\infty - \Psi_0)}, \quad W_{im} = -\frac{C_{V\infty}\Psi_\infty\tilde{m} + C_{V0}\Psi_0\tilde{\mu}_0}{C_{V\infty}(2\Psi_\infty - \Psi_0)}.$$

Thus, we have predicted for the first time that a small perturbation of the step type with an amplitude of $\tilde{v}_1 < \tilde{v}'_{cr}$, which propagates in an acoustically active medium with negative total viscosity $\tilde{\mu}_\Sigma$, can exhibit a decay into stationary shock wave pulses. The stationary structures (Figs. 1 and 2) are characterized by a broad spectrum and cannot be described in terms of the low- and high-frequency approximations used previously.

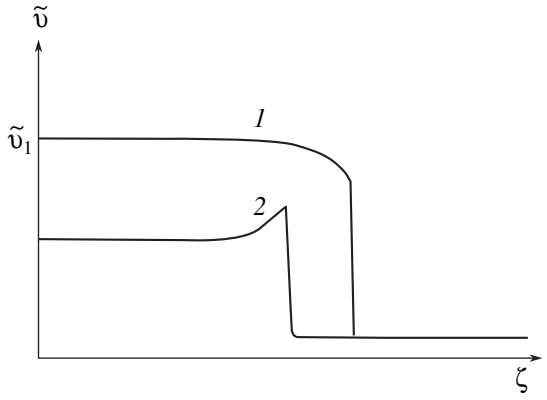

Fig. 1. Stationary structures in a relaxing gas medium (see the text for explanations).

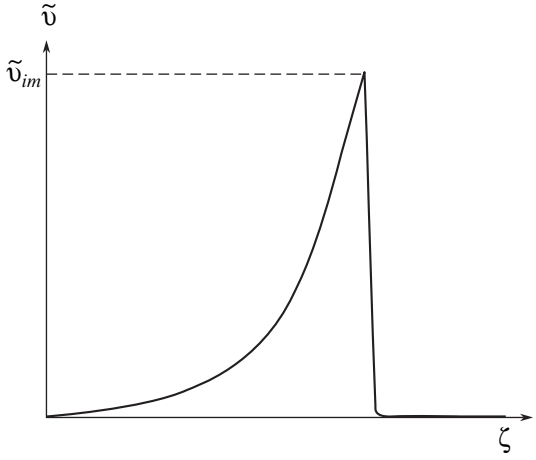

Fig. 2. A stationary shock wave pulse.

REFERENCES

1. N. E. Molevich and A. N. Oraevskiĭ, Tr. Fiz. Inst. Akad. Nauk **222**, 45 (1992).
2. N. E. Molevich, Sib. Fiz.-Tekh. Zh., No. 1, 133 (1991).
3. G. A. Ostroumov, *Fundamentals of Nonlinear Acoustics* (Leningr. Gos. Univ., Leningrad, 1967).

Translated by P. Pozdeev

Technical Physics Letters, Vol. 29, No. 9, 2003, pp. 754–756. Translated from Pis'ma v Zhurnal Tekhnicheskoĭ Fiziki, Vol. 29, No. 18, 2003, pp. 16–21.

Repeated Contraction of Longitudinal and Energy-Tense Repetitively Pulsed Discharges

V. M. Klimkin

Institute of Atmospheric Optics, Siberian Division, Russian Academy of Sciences, Tomsk, Russia

e-mail: lfmi@asd.tomsk.ru

Received March 17, 2003

Abstract—When a metal is placed immediately in the gas discharge channel of a repetitively pulsed metal vapor laser, a decrease in the channel resource is related to a repeated contraction effect (except the discharges in copper and gold vapor). It is concluded that the phenomenon of self-decontraction of repetitively pulsed discharges upon the introduction of a metal vapor (the Petrash effect) is a multicomponent process. *© 2003 MAIK "Nauka/Interperiodica".*

Energy-tense discharges. The development of laser technology, plasma chemistry, and other fields of application of electric discharges required extensive investigation of some nonequilibrium discharges in gases and gas mixtures. Begun about 1969, these investigations aimed primarily at finding methods for pumping high energies into the gas phase. The results of these investigations have been summarized in numerous reviews and monographs [1–5]. According to these data, the main problem encountered in creating nonequilibrium gas discharge systems is related to the instability of discharges [6]. The instability usually implies contraction of a nonequlibrium discharge into a filament, pinching (additional contraction under the action of a magnetic field), and development of a spark or an arc. Physical conditions in a plasma of contracted discharges are close to equilibrium and, hence, are unfavorable for the excitation of lasers and for some other applications involving electric discharges in gases (plasma chemistry, plasma surface processing, etc.).

Almost simultaneously (about 1971), the development of pulsed gas lasers operating on metal vapors has led to a remarkable result, whereby an average power of about 2 kW (per meter of the gas discharge gap length) was introduced into the gas phase (comprising a mixture of metal vapors and inert gases) in a longitudinal nonequlibrium repetitively pulsed discharge without gas circulation [7]. The main feature of this discharge is the passage from a deep contraction in pure inert gases (initial contraction) to the self-decontraction in the presence of a metal vapor [8–12]. It was suggested to call this unique phenomenon the Petrash effect [11, 12].

However, the researchers and technologists engaged in the physics of metal vapor lasers, despite a long history (both before 1971 and since then) and extensive investigation of physical processes in repetitively pulsed discharge plasmas, for a long time did not pay any special attention to the phenomenon of high energy intensity and stability of the discharge discovered in 1971. Nevertheless, the following discharge parameters have been achieved in various experiments with metal vapor lasers: excited medium volume, 18 liters [13]; pulse repetition frequency, 350 kHz [14]; discharge duration in a single pulse, 150 μs [15]; discharge duration at 10 kHz, 1 μs [16]; gas pressure, 5 atm [17]; average laser output power (for one active element), 450 W [13]; average power introduced into discharge (for one active element), 45 kW [13].

Presently, repetitively pulsed discharges in mixtures of metal vapors with inert gases are the most energy-intensive and stable discharge systems (the discharge exhibits no contraction at a temperature difference of up to 2000 K between the discharge axis and the near-wall region).

Limited resource of gas discharge tubes. One of the necessary conditions for obtaining nonequilibrium discharges in gases consists in preionization of a gas in the gas discharge volume. For discharges in excimer lasers, the threshold electron density in the preionization stage is 10^6–10^7 cm^{-3}. In repetitively pulsed discharges used for the excitation of metal vapor lasers, the residual density of electrons by the end of the interval between pulses is significantly greater, reaching 10^{12}–10^{13} cm^{-3}. Apparently, no preionization (in the commonly accepted sense) in the discharge gap is required under these conditions. Nevertheless, an analysis of the conditions necessary for the existence of repetitively pulsed discharges in metal vapor lasers shows that a certain process resembling plasma stabilization of the discharge still takes place.

Taking into account that no special investigations of nonequilibrium repetitively pulsed discharges have been reported, it was expedient to analyze the characteristics of discharges described in the papers devoted to the regime of repetitively pulsed generation in metal vapor lasers. This analysis showed that the discharge

channels of such lasers have significantly different working lifetimes depending on the properties of chemical elements introduced into discharge.

With respect to the lifetime of gas discharge channels, the chemical elements can be divided into three groups. Group A includes two elements, copper and gold. The mixtures of Cu or Au vapors with inert gases introduced into the discharge favor a repetitively pulsed excitation regime with a large lifetime of the discharge channel (>2000 h). This resource is close to the time of complete metal consumption in the working zone. Group B contains a number of elements for which only a short-time (1–10 h) repetitively pulsed discharge operation was observed so far. Group C includes gases (Kr, Xe, etc.) and some elements whose vapors (in mixtures with He and Ne) were never reported to feature decontracted repetitively pulsed discharges.

Taking into account that only two elements enter into group A, there is a problem of expanding the list of elements whose vapors are capable of maintaining a repetitively pulsed discharge regime for a sufficiently long period of time. Below we report the results of investigations showing that the limitation of the working lifetime of a repetitively pulsed discharge channel is caused by a rather unusual factor: repeated contraction of the discharge. This contraction results from coating of the internal surface of the gas discharge channels by a layer of the working metal.

Experimental observation of repeated discharge contraction. Typical observations of the phenomenon of repeated discharge contraction were performed as follows. Aging of the active element of a repetitively pulsed europium vapor laser was monitored by measuring the laser output power, pulsed discharge current, temperature, and side emission from the discharge.

The gas discharge cell comprised a BeO ceramic channel with a diameter of 1 cm and a length of 40 cm, filled with He and containing a weighted amount of Eu freely lying on the internal surface of the channel. After assembling the gas discharge cell and connecting it to a repetitively pulsed power supply unit, the average output power for lasing on a Eu^+ transition with λ = 1.0019 μm at a pulse repetition frequency of ν = 10 kHz usually amounted to 2–3 W. However, after a 2–3-h operation of the active element at a constant channel temperature (see upper curve in the figure), the power exhibited a monotonic decrease to a level of ~0.1 W and below, up to the complete breakdown of generation (see lower curve in the figure). Via windows in the side wall and in the edge of the cell, it was possible to observe dramatic changes in the character of discharge. The discharge transformed from homogeneous to that with running or standing striations and then contracted into a filament. The formation of striations and repeated contraction are indicative of the loss of discharge stability.

Examination of a disassembled cell revealed no failures in the components. However, repeated startup was possible only with a new discharge channel, after which the above scenario was repeated. An analysis of the results of several experiments showed that the internal surface of a used ceramic gas discharge channel disassembled upon operation for several hours, as well as the ground samples of ceramics from the channel are coated with a thin, virtually homogeneous metal film. The discharge cell reassembled upon removal of this layer by etching was capable of operating for another 1–3 h and so on. Being observed in repeated experiments with discharges in the vapors of europium, barium, and strontium, this phenomenon was definitely of a general character. At the same time, it was established that the used gas discharge channels operating in copper or gold vapors do not bear metal films.

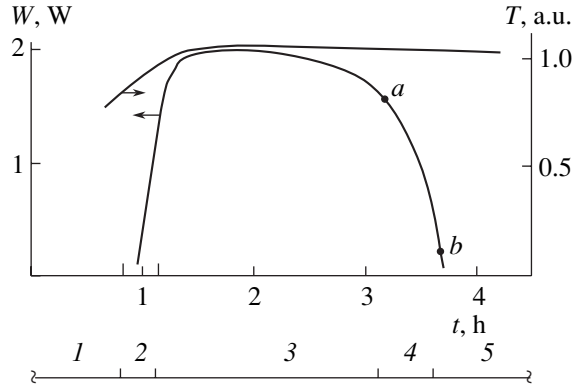

Typical time variation of the average laser output power (lower curve) and the channel temperature (upper curve) during a cycle of contraction of an energy-tense repetitively pulsed discharge in Eu vapor: (*1*) initial discharge contraction; (*2*) decontraction stage; (*3*) homogeneous discharge; (*4*) striation stage; (*5*) repeated discharge contraction. Points (*a*) and (*b*) indicate the moments of appearance of the running striations and the plasma filament, respectively.

Thus, it was experimentally established that an apparently insignificant phenomenon, whereby the discharge channel surface is covered with a thin film of the working metal, violates the Petrash decontraction effect observed upon introduction of a readily ionized additive (metal vapor) into the discharge and leads to repeated discharge contraction. Such metallization of the discharge channel wall is equivalent to switching off the system of preionization in the case of a volume gas discharge. It is possible to distinguish five stages in the process of discharge development (see figure).

The observed phenomenon, the loss of discharge stability as a result of metallization of the discharge channel walls, is indicative of the existence of an additional ionization in the gas discharge gap operating in the repetitively pulsed regime. Further investigation of this phenomenon can lead to the development of methods for controlling the state of a repetitively pulsed discharge. It is also evident that processes involved in the self-decontraction of repetitively pulsed discharges possess a multicomponent character. In repetitively

pulsed metal vapor lasers, the observed phenomena are directly related to the problems of increasing the working lifetime and scaling of the discharge channels.

Acknowledgments. The author is grateful to his colleagues V.E. Prokop'ev and V.G. Sokovikov for their help in conducting experiments.

REFERENCES

1. Yu. I. Bychkov, Yu. D. Korolev, and G. A. Mesyats, *Injection Electronics* (Nauka, Novosibirsk, 1982).
2. Yu. D. Korolev and G. A. Mesyats, *Autoemission and Explosive Processes in Gas Discharge* (Nauka, Novosibirsk, 1982).
3. E. P. Velikhov, V. Yu. Baranov, V. S. Letokhov, E. A. Ryabov, and A. N. Starostin, *Pulse CO_2 Lasers for Channel Separation* (Nauka, Moscow, 1987).
4. Yu. D. Korolev and G. A. Mesyats, *The Physics of Pulsed Gas Breakdown* (Nauka, Moscow, 1991).
5. G. A. Mesyats, V. V. Osipov, and V. F. Tarasenko, *Pulse Gas Lasers* (Nauka, Moscow, 1991).
6. *Gas Lasers*, Ed. by E. McDaniel and U. Nighan (Academic, New York, 1982; Mir, Moscow, 1986).
7. A. A. Isaev, M. A. Kazaryan, and G. G. Petrash, Pis'ma Zh. Éksp. Teor. Fiz. **16** (1), 40 (1972) [JETP Lett. **16**, 27 (1972)].
8. P. A. Bokhan and D. E. Zakrevskiĭ, Zh. Tekh. Fiz. **67** (4), 25 (1997) [Tech. Phys. **42**, 346 (1997)].
9. L. M. Bukshun, E. L. Latush, and M. F. Sem, Kvantovaya Élektron. (Moscow) **15**, 1762 (1988).
10. V. M. Klimkin, A. N. Mal'tsev, and L. V. Fadin, *Effective Gas-Discharge Metal-Vapor Lasers* (Inst. Opt. Atmos. Sib. Otd. Ross. Akad. Nauk, Tomsk, 1978), pp. 116–132.
11. V. M. Klimkin, Preprint IOA SO RAN (Institute of Atmospheric Optics, Siberian Division, Russian Academy of Sciences, Tomsk, 1999).
12. V. M. Klimkin, Proc. SPIE **4747**, 164 (2002).
13. C. Kanagai, N. Auki, N. Kobayasyi, and H. Kimura, in *Proceedings of the 6th International Symposium on Advanced Nuclear Energy Research, Mito, 1994*, p. 673.
14. D. V. Shiyanov, G. S. Evtushenko, A. V. Pavlinskiĭ, *et al.*, in *Proceedings of Symposium on Metal-Vapor Lasers, Rostov-on-Don, 2000*, p. 9.
15. P. A. Bokhan, V. M. Klimkin, and V. E. Prokop'ev, Kvantovaya Élektron. (Moscow), No. 2, 29 (1970).
16. P. A. Bokhan, V. M. Klimkin, V. E. Prokop'ev, and S. S. Monastyrev, Kvantovaya Élektron. (Moscow) **1**, 1365 (1974).
17. P. A. Bokhan and D. E. Zavrevsky, Proc. SPIE **2110**, 220 (1994).

Translated by P. Pozdeev

Technical Physics Letters, Vol. 29, No. 9, 2003, pp. 757–759. Translated from Pis'ma v Zhurnal Tekhnicheskoĭ Fiziki, Vol. 29, No. 18, 2003, pp. 22–28.

Light Wave Diffraction on Reflection Holograms in a Cubic Piezoelectric Crystal

V. V. Shepelevich[a, *], V. N. Navnyko[a], S. F. Nichiporko[a], S. M. Shandarov[b, **], and A. E. Mandel'[b]

[a]*Mozyr State Pedagogical University, Mozyr, Gomel oblast, Belarus*
[b]*Tomsk State University of Control Systems and Radioelectronics, Tomsk, Russia*
*e-mail: *vasshep@inbox.ru; **shand@stack.ru*

Received April 3, 2003

Abstract—Analytical expressions for the electric field strength in a signal wave formed during the interaction of opposite waves in a cubic photorefractive piezoelectric crystal are obtained in the given grating approximation. As a result of the optical activity of the medium, the amplification coefficient and the diffraction efficiency of a hologram in the $(\bar{1}\bar{1}\bar{1})$ cut crystals may exceed the analogous values for the $(00\bar{1})$ cut crystals. © *2003 MAIK "Nauka/Interperiodica".*

Photorefractive crystals are promising recording media for the writing of volume holograms, originally obtained and studied by Denisyuk [1, 2]. While the properties of transmission holograms in photorefractive crystals have been studied in sufficient detail, the reflection holograms received much less attention, although the diffraction efficiency of these holograms can be very high (tens of percent) even in a diffusion regime [3].

The reflection holograms in cubic photorefractive crystals possessing optical activity ($Bi_{12}SiO_{20}$, $Bi_{12}GeO_{20}$, $Bi_{12}TiO_{20}$) were reported in a number of papers (see, e.g., [4–9]). However, all these investigations either were restricted to the (001) cut crystals [4–7], used the undepleted pumping approximation [6, 7, 9], or ignored the piezoelectrical properties of the crystals studied [8].

This study was aimed at obtaining an analytical solution of the equations of coupled waves for a reflection hologram written in a photorefractive piezoelectric crystal of the 23 class with a large modulation depth of the holographic grating (i.e., beyond the undepleted pumping approximation, but within the given grating approximation).

Consider reference (*R*) and signal (*S*) waves propagating in opposite directions and exhibiting diffraction on a holographic phase grating of the reflection type written in a cubic, arbitrarily cut photorefractive piezoelectric crystal (Fig. 1). Let the working coordinate system be determined by the set of mutually orthogonal unit vectors ($\mathbf{e}_1$, $\mathbf{e}_2$, $\mathbf{e}_3$) and let a unit vector $\mathbf{e}$ determine a fixed direction in the crystal face, which coincides with the $\mathbf{e}_1$ vector direction. The basis sets ($\mathbf{e}_1$, $\mathbf{e}_R$, $\mathbf{n}_R$) and ($\mathbf{e}_1$, $\mathbf{e}_S$, $\mathbf{n}_S$) describe polarizations of the reference and signal waves, respectively, and vectors $\mathbf{n}_R$ and $\mathbf{n}_S$ indicate the directions of propagation of these waves. The angles ψ_R and ψ_S characterize the polarization of the reference and signal waves entering the crystal.

Using the standard procedure for solving a system of equations describing the coupled waves in gyrotropic media, we obtain relatively simple analytical

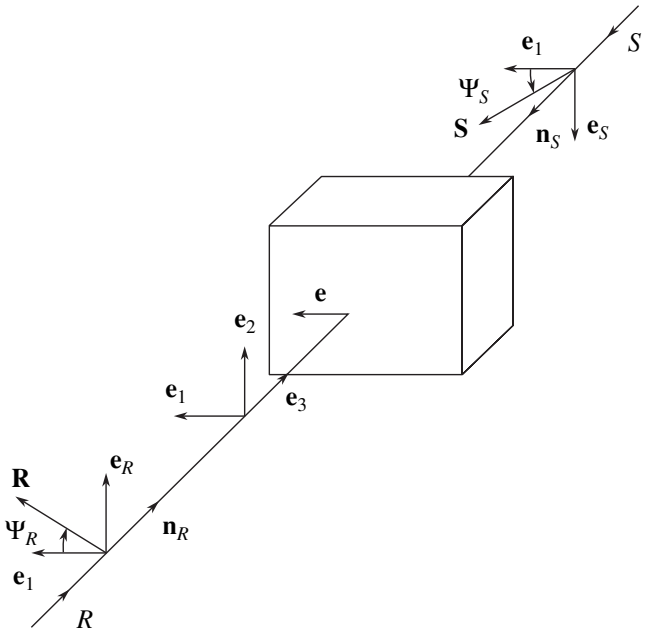

Fig. 1. Geometry of the interaction of a reference (*R*) and signal (*S*) light waves in a photorefractive crystal.

1063-7850/03/2909-0757$24.00 © 2003 MAIK "Nauka/Interperiodica"

expressions for the projections $S_{\parallel}^0$ and $S_{\perp}^0$ of the electric vector in the signal wave onto the $-\mathbf{e}_2$ and $\mathbf{e}_1$ directions, respectively, at the exit from the crystal:

$$S_{\parallel}^0 = \frac{1}{\Delta}\{AS_{\perp}^d + BS_{\parallel}^d + CR_{\perp}^0 + DR_{\parallel}^0\}, \quad (1)$$

$$S_{\perp}^0 = \frac{1}{\Delta}\{\tilde{A}S_{\parallel}^d + \tilde{B}S_{\perp}^d - CR_{\parallel}^0 + \tilde{D}R_{\perp}^0\}, \quad (2)$$

where

$$A = 4q\sinh(qd)(\kappa_2\sinh(\kappa_+ d) - \rho\cosh(\kappa_+ d)),$$

$$\tilde{A} = 4q\sinh(qd)(\kappa_2\sinh(\kappa_+ d) + \rho\cosh(\kappa_+ d)),$$

$$B = 4q(q\cosh(\kappa_+ d)\cosh(qd) - \kappa_-\sinh(\kappa_+ d)\sinh(qd)),$$

$$\tilde{B} = 4q(q\cosh(\kappa_+ d)\cosh(qd) + \kappa_-\sinh(\kappa_+ d)\sinh(qd)),$$

$$C = 2\kappa_2 q\sinh(2qd) - 4\rho\kappa_-\sinh^2(qd),$$

$$D = (2q^2\sinh(2\kappa_+ d) + 4\rho\kappa_2\sinh^2(qd) + 2\kappa_- q\sinh(2qd)),$$

$$\tilde{D} = (-2q^2\sinh(2\kappa_+ d) + 4\rho\kappa_2\sinh^2(qd) + 2\kappa_- q\sinh(2qd)),$$

$$\Delta = 2\kappa_-^2(\cosh(\kappa_+ d) + \cosh(2qd)) - 4\rho^2\cosh^2(\kappa_+ d) + 4\kappa_2^2(\cosh^2(qd) + \sinh^2(\kappa_+ d)),$$

$$q = \sqrt{\frac{(\kappa_3 - \kappa_1)^2}{4} + \kappa_2^2 - \rho^2},$$

$$\kappa_+ = \frac{\kappa_3 + \kappa_1}{2}, \quad \kappa_- = \frac{\kappa_3 - \kappa_1}{2},$$

$R_{\perp}^0$, $R_{\parallel}^0$, $S_{\perp}^d$, and $S_{\parallel}^d$ are the projections of the electric vector in the reference and signal wave onto the $\mathbf{e}_1$, $\mathbf{e}_R$, $\mathbf{e}_2$, and $\mathbf{e}_S$ directions, respectively, at the entrance into the crystal; $\kappa_1 = (\mathbf{e}_1\hat{\kappa}\,\mathbf{e}_1)$, $\kappa_2 = (\mathbf{e}_1\hat{\kappa}\,\mathbf{e}_2)$, $\kappa_3 = (\mathbf{e}_2\hat{\kappa}\,\mathbf{e}_2)$, and $\hat{\kappa} = -\frac{\pi n^3 E}{2\lambda}\hat{b}$; n is the refractive index; E is the electric field amplitude in the holographic grating; $\hat{b}$ is the change in the inverse dielectric permittivity tensor [10]; ρ is the optical rotatory power; and d is the crystal thickness.

Using solutions (1) and (2), one can readily obtain expressions for the signal wave amplification γ and the diffraction efficiency η of the hologram in crystals with the $(00\bar{1})$ ($\gamma_{(00\bar{1})}$ and $\eta_{(00\bar{1})}$) and $(\bar{1}\bar{1}\bar{1})$ ($\gamma_{(\bar{1}\bar{1}\bar{1})}$ and $\eta_{(\bar{1}\bar{1}\bar{1})}$) faces.

1. For the $(00\bar{1})$ cut crystal, $\mathbf{e} \parallel \mathbf{a}$:

$$\gamma_{(00\bar{1})} = \frac{I_S(0)}{I_S(d)} = \frac{1 + \Gamma\frac{\kappa_1^2}{\beta}\sin^2(\sqrt{\beta}d) - 2\sqrt{\Gamma}\frac{\kappa_1}{\sqrt{\beta}}\sin(\psi_R - \psi_S)\sin(\sqrt{\beta}d)}{\cos^2(\sqrt{\beta}d) + \frac{\kappa_1^2}{\beta}\sin^2(\sqrt{\beta}d)}, \quad (3)$$

$$\eta_{(00\bar{1})} = \frac{I_S(0)}{I_R(0)} = \frac{\sin^2(\sqrt{\beta}d)}{\frac{\rho^2}{\kappa_1^2} - \cos^2(\sqrt{\beta}d)}, \quad (4)$$

where $\beta = \rho^2 - \kappa_1^2$.

2. For the $(\bar{1}\bar{1}\bar{1})$ cut crystal, $\mathbf{e} \parallel (2\mathbf{c} - \mathbf{a} - \mathbf{b})/\sqrt{6}$:

$$\gamma_{(\bar{1}\bar{1}\bar{1})} = \frac{1}{\cosh^2(\kappa_2 d)} + \Gamma\tanh^2(\kappa_2 d) - 2\sqrt{\Gamma}\cos(\psi_R + \psi_S - \rho d)\frac{\tanh(\kappa_2 d)}{\cosh(\kappa_2 d)}, \quad (5)$$

$$\eta_{(\bar{1}\bar{1}\bar{1})} = \tanh^2(\kappa_2 d), \quad (6)$$

where $I_S(0)$ is the signal wave intensity at the crystal exit; $I_S(d)$ and $I_R(0)$ are the signal and reference wave intensities at the crystal exit, respectively; $\Gamma = I_R(0)/I_S(d)$; **a**, **b**, **c** are the unit vectors of the principal crystallographic directions.

In order to analyze the dependences of the effective amplification coefficient γ and the diffraction efficiency η of the hologram on the crystal thickness, we use the well-known polarization condition $\psi_R = -\psi_S + \rho d$ [4], which is valid for any thickness of the crystal. Under this very condition for the azimuth angles of polarization of the reference and signal waves, the value of κ reaches its maximum during the hologram recording. As can be readily seen, the amplification coefficient γ for the $(00\bar{1})$ cut crystal depends both on the polarization angle of the signal wave ($\psi_S = \psi_0$) and on the crystal thickness d, while the γ value for the $(\bar{1}\bar{1}\bar{1})$ orientation depends only on the crystal thickness. For both crystal cuts, the diffraction efficiency of the hologram is independent of the reading beam polarization.

Plots of the amplification coefficient γ and the diffraction efficiency η versus thickness d of an optically active $(00\bar{1})$ cut crystal exhibit a pronounced periodic character (Fig. 2). Under the condition that $\rho d = \pi k$ (where k is an integer), the energy exchange between the two light waves is absent (Fig. 2a, points *A* and *B*) and the diffraction efficiency is zero (Fig. 2b, points *F* and *G*). For the $(\bar{1}\bar{1}\bar{1})$ cut crystal, the plots of γ and η

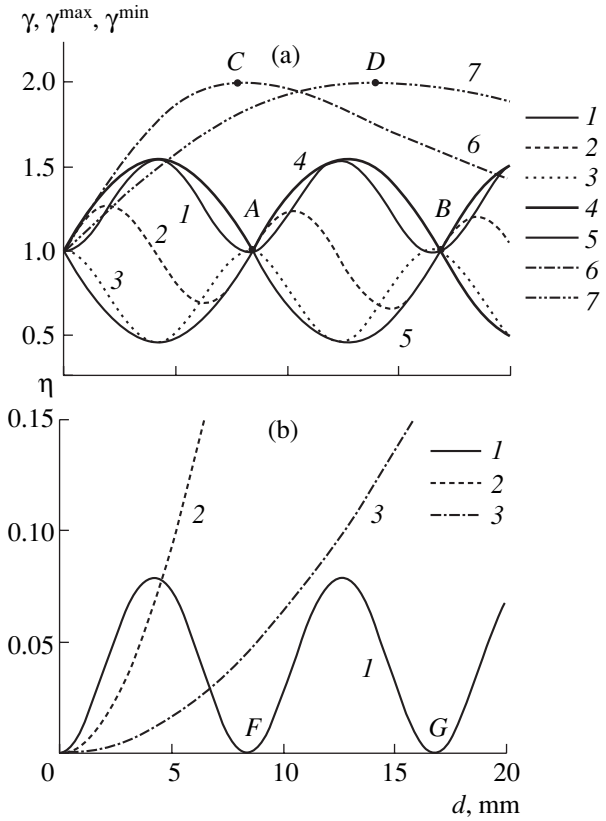

Fig. 2. (a) Plots of the effective signal wave amplification coefficient γ versus hologram thickness d: (*1–3*) $\gamma(d)$ for the $(00\bar{1})$ cut crystal and the initial polarization ψ_0 = 0, 45°, and 90°, respectively; (*4*) $\gamma^{max}(d)$ for the $(00\bar{1})$ cut crystal; (*5*) $\gamma^{min}(d)$ for the $(00\bar{1})$ cut crystal; (*6, 7*) $\gamma(d)$ for the $(\bar{1}\bar{1}\bar{1})$ cut crystal without and with allowance of the piezoelectric effect; (b) diffraction efficiency η versus hologram thickness d: (*1*) for the $(00\bar{1})$ cut crystal; (*2, 3*) for the $(\bar{1}\bar{1}\bar{1})$ cut crystal without and with allowance of the piezoelectric effect.

versus d are monotonic until reaching the points C and D, where the intensity is completely pumped from one wave to another. When the crystal thickness is close to $d = \pi k/\rho$, the values of $\gamma_{(\bar{1}\bar{1}\bar{1})}$ and $\eta_{(\bar{1}\bar{1}\bar{1})}$ always exceed the values of $\gamma_{(00\bar{1})}$ and $\eta_{(00\bar{1})}$, despite the fact that the coupling constant for the $(\bar{1}\bar{1}\bar{1})$ cut crystal (with neglect of the piezoelectric effect) is smaller (by $1/\sqrt{3}$) than the constant for the $(00\bar{1})$ cut crystal. As can also be seen from Fig. 2, both the amplification coefficient and the diffraction efficiency of the hologram in $(\bar{1}\bar{1}\bar{1})$ cut crystals of moderate thickness decrease under the action of the piezoelectric effect. The plots were constructed for a $Bi_{12}SiO_{20}$ crystal with the parameters reported in [10].

Conclusions. Analytical expressions for the electric vector components are obtained in the given grating approximation for a signal wave propagating through a cubic photorefractive piezoelectric crystal and interacting with the opposite wave. The amplification coefficient and the diffraction efficiency of a reflection hologram are determined for the $(00\bar{1})$ and $(\bar{1}\bar{1}\bar{1})$ cut crystals. Under certain conditions, the latter crystal orientation is preferred from the standpoint of obtaining both a high amplification coefficient and an optimum diffraction efficiency.

Acknowledgments. This study was performed within the framework of a joint Belarus–Russia project supported by the Foundation for Basic Research of the Republic of Belarus (project no. F02R-143) and by the Russian Foundation for Basic Research (project nos. F02P-143 and 02-02-81044).

REFERENCES

1. Yu. N. Denisyuk, Dokl. Akad. Nauk SSSR **144**, 1275 (1962) [Sov. Phys. Dokl. **7**, 543 (1962)].
2. Yu. N. Denisyuk, Opt. Spektrosk. **15**, 522 (1963).
3. G. Dovgalenko, G. Salamo, G. Duree, *et al.*, in *Proceedings of Topical Meeting on Photorefractive Materials: Effects and Devices (PR-95), Aspen Lodge at Estes Park, 1995*, pp. 295–298.
4. N. V. Kukhtarev, G. E. Dovgalenko, and V. N. Starkov, J. Appl. Phys. A **33**, 227 (1984).
5. E. M. Khramovich and V. V. Shepelevich, Izv. Akad. Nauk Resp. Bel., Ser. Fiz.-Mat., No. 2, 106 (1987).
6. S. Mallick, M. Miteva, and L. Nikolova, J. Opt. Soc. Am. B **14**, 1179 (1997).
7. M. Weber, E. Shamonina, K. H. Ringhofer, *et al.*, Opt. Mater. **18**, 119 (2001).
8. N. V. Kukhtarev, B. S. Chen, P. Venkateswarlu, *et al.*, Opt. Commun. **104**, 23 (1993).
9. A. G. Mart'yanov, S. M. Shandarov, and R. V. Litvinov, Fiz. Tverd. Tela (St. Petersburg) **44**, 1006 (2002) [Phys. Solid State **44**, 1050 (2002)].
10. S. M. Shandarov, V. V. Shepelevich, and N. D. Khat'kov, Opt. Spektrosk. **70**, 1068 (1991) [Opt. Spectrosc. **70**, 627 (1991)].

Translated by P. Pozdeev

Technical Physics Letters, Vol. 29, No. 9, 2003, pp. 760–763. Translated from Pis'ma v Zhurnal Tekhnicheskoĭ Fiziki, Vol. 29, No. 18, 2003, pp. 29–36.

K-Shell Ionization of a Quasirelativistic Hydrogenlike Atom upon Collision with a Relativistic Structural Multiply Charged Ion

V. I. Matveev*, E. S. Gusarevich, and I. N. Pashev

Pomorskiĭ State University, Arkhangelsk, Russia
Arkhangelsk State Technical University, Arkhangelsk, Russia
** e-mail: matveev.victor@pomorsu.ru*
Received March 11, 2003

Abstract—The differential and total ionization cross sections of a heavy hydrogenlike atom colliding with a relativistic structural heavy ion are calculated using a relativistic generalization of the method of solution matching and the eikonal approximation. By structural ions are implied partly stripped ions of heavy elements comprising a nucleus and a certain number of bound electrons partly compensating for the nuclear charge. The heavy target atom is described using quasirelativistic wave functions. It is shown that an allowance for relativistic effects in the heavy target atom leads to significant changes in the ionization cross sections as compared to those determined within the framework of a nonrelativistic description. © *2003 MAIK "Nauka/Interperiodica".*

Experimental investigations of collision processes involving heavy ions possessing high charges and energies frequently involve partly stripped ions (see, e.g., [1–7] and references therein). In the calculations schemes used to describe the process of excitation and ionization of target atoms, such ions are usually considered as point charges. A relatively small number of investigations were devoted to development of the calculation schemes describing partly stripped ions as finite-size charged particles with a certain electron structure. The strong field of the multiply charged ion hinders using the perturbation theory. For this reason, the ionization cross sections have usually been performed (see, e.g., [8, 9]) within the framework of the well-known method of classical trajectories. The quantum-mechanical description based on a sudden perturbation approximation attempted by Yudin [10, 11] only allowed the ionization probabilities to be determined within a limited interval of impact parameters.

Previously [12, 13], the energy losses in the collisions of relativistic structural heavy ions with light (nonrelativistic) atoms were calculated using the eikonal approximation. Recently [14], we used the same approach to calculate the cross sections of the single and double ionization of hydrogenlike and heliumlike atoms. The results obtained in [14] can be used for calculating the cross sections of the formation of single and double vacancies in the *K*-shells of only light atoms. In calculating the cross section of analogous inelastic processes in heavy atoms, it is necessary to take into account the relativistic character of the motion of electrons both in the bound states and in the continuum.

In this study, we have developed a nonperturbative method for calculating the ionization cross sections of heavy quasirelativistic hydrogenlike target atoms interacting with partly stripped relativistic multiply charged ions considered as extended charges. The proposed method is based on a relativistic generalization [15, 16] of the method of solution matching and the eikonal approximation and on their extension to the case of extended charges proposed previously [12, 17]. For illustration, the proposed method is applied to calculation of the total and differential ionization cross sections. It will be shown that an allowance for the relativistic effects leads to significant changes in the total and differential ionization cross sections as compared to those determined within the framework of a nonrelativistic description of the target. These changes are substantial only in the case of targets with large nuclear charges. It should be noted that we decline from discussing the processes of excitation and loss of electrons belonging to the projectile ions, which are now under extensive experimental and theoretical investigation (see, e.g., [2, 18]).

Consider a hydrogenlike atom at rest at the origin of coordinates. According to [15, 16], the differential cross section for the ionization of this atom, whereby it passes from the ground state $|0\rangle$ (with the energy E_0) into state $|\mathbf{k}\rangle$ in the continuum (with the momentum $\mathbf{k}$ and energy $E_\mathbf{k}$) upon collision with a relativistic ion possessing the nuclear charge Z and moving at the velocity $\mathbf{v}$ can be described in the eikonal approximation as (here and below, we use the atomic system of units where $\hbar = e = m_e = 1$, $\hbar$ being the Planck constant, e the electron charge, and m_e the electron mass)

1063-7850/03/2909-0760$24.00

$$d\sigma = \int d^2\mathbf{b}\left|\left\langle \mathbf{k}\left|\left[1-\exp\left(-\frac{i}{v}\int U dX\right)\right]\right|\gamma^{-1}S^2\exp\left\{i\frac{xv}{c^2}(E_\mathbf{k}-E_0)\right\}\right|0\right\rangle\right|^2 d^3\mathbf{k}. \quad (1)$$

In this relation, **b** is the impact parameter, $S^2 = \gamma(1 - \boldsymbol{\alpha}\boldsymbol{\beta})$, $\gamma = (1 - \boldsymbol{\beta}^2)^{-1/2}$, $\boldsymbol{\beta} = \mathbf{v}/c$, $\boldsymbol{\alpha}$ are the Dirac matrices. and c is the velocity of light in vacuum (the x axis is directed along the ion velocity).

The scattering Coulomb potential $U = U(X, \mathbf{b}; \mathbf{r})$ is considered as a function of both the ion coordinates $\mathbf{R} = (X, \mathbf{b})$ and the positions of the atomic electron $\mathbf{r} = (x, \mathbf{s})$, where **s** is the projection of **r** onto the plane of the impact parameter **b**. According to [12, 14], the eikonal phase in formula (1) can be represented as

$$-\frac{i}{v}\int U dX = i\mathbf{q}\mathbf{s},$$

where

$$\mathbf{q} = \frac{2Z^*}{vb}\left[1 + \frac{\nu}{1-\nu}\frac{b}{\lambda}K_1\left(\frac{b}{\lambda}\right)\right]\frac{\mathbf{b}}{b}.$$

Here, the vector **q** has an evident meaning of the momentum transfer to the atomic electron from a structural projectile ion with an impact parameter **b**, $K_1(x)$ is the Macdonald function, $Z^* = Z(1 - \nu)$ is the effective (apparent) ion charge, $\nu = N_i/Z$ is the relative number of electrons in the ion coat, N_i is the total number of electrons in the shells, λ is the screening parameter (or the effective ion radius). The latter quantity is given by the formula $\lambda = g\nu^{2/3}(1 - \nu/7)^{-1}Z^{-1/3}$ where $g \approx 0.48$ [19].

Formula (1) for the ionization cross section was derived [15, 16] based on a relativistic generalization of the eikonal approximation taking into account the relativistic character of motion for both the impinging ion and the target atom. However, the calculations performed previously (see, e.g., [14]) for the cross sections of ionization by impact of a structural heavy ion took into account only the relativistic motion of the projectile ion.

In this study, we allow for the relativistic effects in the target atom as well. For this calculation, the wave functions in the initial ($|0\rangle$) and final ($|\mathbf{k}\rangle$) states will represent (as in [20, 21]) the quasirelativistic wave functions determined according to Darwin [22–24]:

$$|0\rangle \equiv \Psi_{0,s}(\mathbf{r}) = N_0\left(1 - \frac{i}{2c}\boldsymbol{\alpha}\nabla\right)\phi_0(\mathbf{r})u_s,$$

$$|\mathbf{k}\rangle \equiv \Psi_{\mathbf{k},s'}(\mathbf{r}) = N_1\left(1 - \frac{i}{2c}\boldsymbol{\alpha}\nabla\right)\phi_\mathbf{k}(\mathbf{r})u_{s'},$$

$$\phi_\mathbf{k}(\mathbf{r}) = (2\pi)^{-3/2}\exp\left(\frac{\pi\xi}{2}\right)\Gamma(1 + i\xi) \quad (2)$$

$$\times \exp(i\mathbf{k}\mathbf{r})F(-i\xi, 1, -i(kr + \mathbf{k}\mathbf{r})),$$

$$\phi_0(\mathbf{r}) = \sqrt{Z_a^3/\pi}\exp(-Z_a r).$$

Here, ϕ_0 and $\phi_\mathbf{k}$ are the nonrelativistic wave functions of the ground state and continuum for a hydrogenlike atom with a nuclear charge Z_a, $\xi = Z_a/k$, $\Gamma(x)$ is the gamma function, $F(\alpha, \gamma, z)$ is the degenerate hypergeometric function, u_s is the bispinor of a resting electron with the spin projection s, and $N_1 = (1 + (k/2c)^2)^{-1/2}$ and $N_0 = (1 + (Z_a/2c)^2)^{-1/2}$ are the normalization factors (see, e.g., [20, 21]). Following [16, 17], we assume for the quasirelativistic atom that $\exp\{ixv(E_k - E_0)/c^2\} \approx 1$ and $\gamma^{-1}S^2 \approx 1$.

Using the method of solution matching [14–16], we obtain an expression for the differential cross section of electron emission with the energy ε_k in the following form:

$$\frac{d\sigma}{d\varepsilon_k} = 8\pi\frac{Z^{*2}}{\mathbf{v}^2}\lambda_k k\left(\ln\frac{2Z_a\alpha_k\mathbf{v}^2\gamma}{\eta Z^*\omega_k} - \frac{\beta^2}{2}\right). \quad (3)$$

Here, $\eta = \exp B = 1.781$, $B = 0.5772$ is the Euler constant, $\omega_k = \varepsilon_k - \varepsilon_0$, $\varepsilon_k = k^2/2$, and $\varepsilon_0 = -Z_a^2/2$. The quantities λ_k and α_k are given by the formulas (cf. [14, 15])

$$\lambda_k = \frac{1}{3}(N_1N_0)^2\int|\langle\phi_\mathbf{k}|\mathbf{r}|\phi_0\rangle|^2 d\Omega_\mathbf{k},$$

$$\alpha_k = \lim_{b_0\to\infty}\frac{Z^*}{\mathbf{v}Z_a b_0}$$

$$\times\exp\left\{\frac{1}{\lambda_k}\frac{\mathbf{v}^2}{8\pi Z^{*2}}(N_1N_0)^2\int_0^{b_0}2\pi b db\int d\Omega_\mathbf{k}|\langle\phi_\mathbf{k}|\exp(i\mathbf{q}\mathbf{r})|\phi_0\rangle|^2\right\},$$

where $\Omega_\mathbf{k}$ is the solid angle of the momentum vector **k** of the emitted electron. In the formulas for λ_k and α_k, the integration is performed over all $\Omega_\mathbf{k}$.

We have used formula (3) to calculate the differential cross section (spectrum) of electron emission from a hydrogenlike atom of molybdenum Mo^{41+} colliding with a relativistic uranium ion U^{50+}. The results of this calculation are presented in Fig. 1. For evaluating the contribution of relativistic effects to the differential ionization cross section of a heavy hydrogenlike atom, it is convenient to introduce a relative correction $\chi = [(d\sigma/d\varepsilon_k)_n - (d\sigma/d\varepsilon_k)_r]/(d\sigma/d\varepsilon_k)_n = 1 - (N_0N_1)^2$, where indices n and r indicate the nonrelativistic and relativistic descriptions, respectively. Thus, the correction χ in the quasirelativistic approach is given by a simple formula depending only on the nuclear charge Z_a of the target and on the emitted electron energy ε_k. At the same time, the correction is independent of the energy

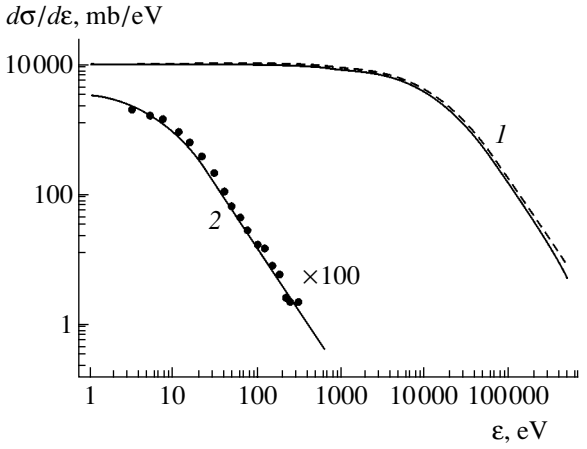

Fig. 1. Plots of the ionization cross section versus the emitted electron energy ε: (*1*) for a structural U^{50+} ion (projectile) with an energy of 10000 MeV/nucleon colliding with a hydrogenlike Mo^{41+} target atom (solid and dashed curves correspond to a quasirelativistic and nonrelativistic descriptions of the target, respectively); (*2*) for a stripped C^{6+} ion with an energy of 2.5 MeV/nucleon colliding with a hydrogen atom (solid curve shows the results of calculations, black circles represent the experimental data [25]; both calculated and experimental values are multiplied by a factor of 100).

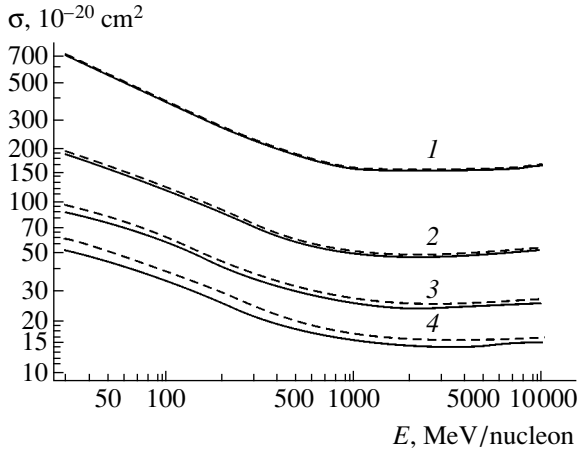

Fig. 2. Plots of the total ionization cross section for various hydrogenlike target atoms versus the energy of the impinging U^{50+} ion (solid and dashed curves correspond to a quasirelativistic and nonrelativistic descriptions of the target, respectively): (*1*) Mg^{11+} (Z_a = 12); (*2*) Ti^{21+} (Z_a = 22); (*3*) Ge^{31+} (Z_a = 32); (*4*) Mo^{41+} (Z_a = 42).

and charge of the impinging ion. As the emitted electron energy grows, the correction increases. For example, in a Mo^{41+} target, χ = 2.31% and 11.1% for the electron energies ε_k = 100 eV and 100 keV, respectively. Unfortunately, no experimental data are available on the electron spectra for the *K*-shell ionization of heavy hydrogenlike atoms by structural heavy relativistic ions in the range of energies and charges under consideration. For this reason, we illustrate the results obtained using the proposed method in the case of insignificant relativistic effects in the target. For this purpose, Fig. 1 shows the electron emission spectrum calculated using formula (3) for a hydrogen atom colliding with stripped carbon ions in comparison to the experimental data reported in [25].

The total ionization cross section of a hydrogenlike heavy target is obtained by integrating expression (3) over the entire interval of energies of the emitted electron. According to the method of solution matching [14, 15], this is equivalent to calculation of the following values:

$$\lambda_i = \int_0^\infty \lambda_k k^2 dk, \quad \omega_i = \exp\left\{\frac{1}{\lambda_i}\int_0^\infty k^2 \lambda_k \ln\omega_k dk\right\},$$
$$\alpha_i = \exp\left\{\frac{1}{\lambda_i}\int_0^\infty k^2 \lambda_k \ln\alpha_k dk\right\}. \qquad (4)$$

In these terms, the total ionization cross section is expressed as

$$\sigma = 8\pi\frac{Z^{*2}}{\mathbf{v}^2}\lambda_i\left(\ln\frac{2Z_a\alpha_i\mathbf{v}^2\gamma}{\eta Z^*\omega_i} - \frac{\beta^2}{2}\right). \qquad (5)$$

Figure 2 gives an example of using formula (5) for calculating the total ionization cross section of a hydrogenlike target atom as a function of the energy of impinging U^{50+} ions for several values of the nuclear charge of the target. As can be seen from these data, allowance for relativistic effects in the target leads to a decrease in the total ionization cross section as com-

The relative contribution η of the relativistic effects determined as a function of the energy *E* [MeV/nucleon] of a relativistic structural ion U^{50+} colliding with hydrogenlike atoms of Mg^{11+} (Z_a = 12), Ti^{21+} (Z_a = 22), Ge^{31+} (Z_a = 32) and Mo^{41+} (Z_a = 42)

E, MeV/n	50	100	500	1000	5000	10000	50000	100000
η, % (Z_a = 12)	1.5	1.4	1.1	1.0	0.9	0.9	0.8	0.7
η, % (Z_a = 22)	4.6	3.9	3.0	2.8	2.5	2.4	2.2	2.1
η, % (Z_a = 32)	8.2	6.9	5.4	5.0	4.6	4.4	4.1	4.0
η, % (Z_a = 42)	12.0	10.1	8.1	7.6	7.0	6.8	6.4	6.2

pared to that obtained in the nonrelativistic description. The relative contributions of the relativistic effects determined as $\eta = [\sigma_n - \sigma_r]/\sigma_n$ are given in the table, where indices *n* and *r* refer to the nonrelativistic and relativistic descriptions of the target, respectively. In accordance with formulas (4) and (5), the values of η depend on the characteristics of both the target and the projectile.

Acknowledgments. This study was supported by the Russian Foundation for Basic Research (project no. 01-02-17047) and by the Ministry of Education of the Russian Federation (project no. E02-3.2-512).

REFERENCES

1. H. F. Krause, C. R. Vane, S. Datz, *et al.*, Phys. Rev. A **63**, 032711 (2001).
2. T. Ludziejewski, Th. Stohlker, D. C. Ionescu, *et al.*, Phys. Rev. A **61**, 052706 (2000).
3. E. Wells, I. Ben-Itzhak, K. D. Carnes, *et al.*, Phys. Rev. A **60**, 3734 (1999).
4. M. Tschersich, R. Drozdowski, M. Busch, *et al.*, J. Phys. B **32**, 5556 (1999).
5. M. B. Shah and H. B. Gilbody, J. Phys. B **16**, L449 (1983).
6. J. H. McGuire, A. Mueller, B. Schuch, *et al.*, Phys. Rev. A **35**, 2479 (1987).
7. H. Berg, J. Ullrich, E. Bernstein, *et al.*, J. Phys. B **25**, 3655 (1992).
8. M. Purkait, A. Dhara, S. Sounda, *et al.*, J. Phys. B **34**, 755 (2001).
9. C. Illescas, B. Pons, and A. Riera, Phys. Rev. A **63**, 062722 (2001).
10. G. L. Yudin, Dokl. Akad. Nauk SSSR **282**, 874 (1985) [Sov. Phys. Dokl. **30**, 488 (1985)].
11. G. L. Yudin, Zh. Tekh. Fiz. **55**, 9 (1985) [Sov. Phys. Tech. Phys. **30**, 4 (1985)].
12. V. I. Matveev, Zh. Éksp. Teor. Fiz. **121**, 260 (2002) [JETP **94**, 217 (2002)].
13. V. I. Matveev, Zh. Tekh. Fiz. **72** (5), 10 (2002) [Tech. Phys. **47**, 523 (2002)].
14. V. I. Matveev and E. S. Gusarevich, Zh. Éksp. Teor. Fiz. **123**, 42 (2003) [JETP **96**, 34 (2003)].
15. V. I. Matveev and Kh. Yu. Rakhimov, Zh. Éksp. Teor. Fiz. **114**, 1646 (1998) [JETP **87**, 891 (1998)].
16. V. I. Matveev, D. U. Matrasulov, and Kh. Y. Rakhimov, J. Phys. B **32**, 3849 (1999).
17. V. I. Matveev and D. U. Matrasulov, J. Phys. B **33**, 2721 (2000).
18. A. B. Voitkiv, C. Muller, and N. Grun, Phys. Rev. A **66**, 062701 (2000).
19. W. Brandt and M. Kitagawa, Phys. Rev. B **25**, 5631 (1982).
20. R. Anholt, Phys. Rev. A **19**, 1004 (1979).
21. D. M. Davidovic, B. L. Moiseivitsch, and P. H. Norrington, J. Phys. B **11**, 847 (1978).
22. C. G. Darwin, Proc. R. Soc. London, Ser. A **118**, 654 (1928).
23. J. Eichler and W. E. Meyrhoft, *Relativistic Atomic Collisions* (Academic, New York, 1995).
24. V. B. Berestetskii, E. M. Lifshitz, and L. P. Pitaevskii, *Course of Theoretical Physics*, Vol. 4: *Quantum Electrodynamics* (Nauka, Moscow, 1989; Pergamon, New York, 1982).
25. L. C. Tribedi, P. Richard, L. Gulyás, *et al.*, Phys. Scr. **T80**, 333 (1999).

Translated by P. Pozdeev

Technical Physics Letters, Vol. 29, No. 9, 2003, pp. 764–767. Translated from Pis'ma v Zhurnal Tekhnicheskoĭ Fiziki, Vol. 29, No. 18, 2003, pp. 37–45.

The Properties of Modes in Microstructured Optical Fibers in the Vicinity of Critical Conditions

A. B. Sotsky and L. I. Sotskaya

Institute of Applied Optics, National Academy of Sciences of Belarus, Mogilev, Belarus

e-mail: ipo@physics.belpak.mogilev.by

Received January 8, 2003; in final form, April 21, 2003

Abstract—A new method based on the analysis of integral equations is proposed for calculating the properties of microstructured optical fibers (MOFs) and used for the analysis of modes in MOFs in the vicinity of critical conditions. Slow leaky modes are found that can influence the MOF transmission. © *2003 MAIK "Nauka/Interperiodica".*

In recent years, much effort has been devoted to the study of microstructured optical fibers (MOFs) formed by systems of capillaries. The interest in these MOFs is related to their unique nonlinear, polarization, and dispersive properties [1]. A number of theoretical methods have been developed for the analysis of modes existing in such MOFs [2–9]. Among these methods, of special interest is the numerical multipole method [5–7], which takes into account the vector character of the problem, allows for a finite number of holes in the fiber cross section, and is capable of describing the leaky modes. This technique employs expansions of the longitudinal electromagnetic field components with respect to cylindrical harmonics, the amplitudes of which are determined from the conditions of continuity of the tangential field components at the hole boundaries. Unfortunately, this approach is rather complicated.

Below, we describe an alternative method for the calculation of modes in MOFs with a finite number of holes in the cross section. The new method is based on an analysis of the exact integral equations describing transverse magnetic field components in the region of holes and allows the vector waveguide problem to be solved by numerical techniques. The proposed method is applied to two models: (i) a MOF formed by systems of air channels in a homogeneous material and (ii) a MOF comprising a fiber rod surrounded by air channels. The main attention is devoted to elucidating the properties of modes in MOFs of the second type in the vicinity of critical conditions.

Let us consider the widely used model of a MOF with the cross section comprising n round holes surrounded by a homogeneous medium with the permittivity ε_s. The holes have the radii a_l and are filled by media with the permittivities ε_l ($l = 1, 2, \ldots, n$). For such a MOF oriented along the 0z axis, the transverse magnetic field components of the eigenmodes and leaky modes (varying with the time as $\exp(i\omega t)$) satisfy the integral equations [10]

$$H_j(x, y) = \frac{i}{4}\int_{-\infty}^{\infty} dx' \int_{-\infty}^{\infty} H_0^{(2)}(k_b r) f_j(x', y') dy', \qquad (1)$$

where $j = x$ or y, $H_0^{(2)}(k_b r)$ is the Hankel function, $k_b = \sqrt{k_0^2\varepsilon_s - \beta^2}$, $k_0 = 2\pi\lambda_0^{-1}$ is the free-space wavenumber, β is the mode propagation constant, $r = \sqrt{(x'-x)^2 + (y'-y)^2}$,

$$f_j = E\frac{\partial\varepsilon}{\partial\xi_j} - k_0^2\Delta\varepsilon H_j, \quad E = \frac{1}{\varepsilon}\left(\frac{\partial H_y}{\partial x} - \frac{\partial H_x}{\partial y}\right),$$

$$\xi_x = -y, \quad \xi_y = x, \quad \Delta\varepsilon = \varepsilon(x, y) - \varepsilon_s,$$

and $\varepsilon(x, y)$ is the permittivity of the space.

Let us write the functions $H_j(x, y)$ in the lth hole ($l = 1, 2, \ldots, n$) in the form of a series

$$H_j = \sum_{\nu=-\infty}^{\infty} C_{l\nu}^{(j)} J_\nu(\kappa_l\rho)\exp(i\nu\varphi), \qquad (2)$$

where $J_\nu(\kappa_l\rho)$ are the Bessel functions, $\kappa_l = \sqrt{k_0^2\varepsilon_l - \beta^2}$, and φ and ρ are the polar coordinates. Using an addition formula for the cylindrical functions [11], Eqs. (1) in the lth hole can be written as

$$H_x + (-1)^p iH_y = H_x + (-1)^p iH_y + \delta H_{lp}, \qquad (3)$$

where $p = 0$ or 1,

$$\delta H_{lp} = \sum_{\nu=-\infty}^{\infty} U_{l\nu}^{(p)} J_\nu(k_b\rho)\exp(i\nu\varphi),$$

$$U_{l\nu}^{(p)} = R_{1\nu}^{lp} A_\nu^{lp} + R_{2\nu}^{lp} A_{\nu+\sigma}^{lq} + \sum_{k\neq l}\sum_{\mu=-\infty}^{\infty} (G_{\mu-\nu}^{(k)} S_{1\mu}^{kp} A_\mu^{kp} + G_{\mu-\nu-\sigma}^{(k)} S_{2\mu-\sigma}^{kp} A_\mu^{kq}),$$

$$R_{1\nu}^{l0} = 0.25i\pi a_l\kappa_l[H_\nu^{(2)}(k_b a_l)(\varepsilon_s\varepsilon_l^{-1}J_{\nu-1}(\kappa_l a_l) + J_{\nu+1}(\kappa_l a_l)) - k_b\kappa_l^{-1}J_\nu(\kappa_l a_l)(H_{\nu-1}^{(2)}(k_b a_l) - H_{\nu+1}^{(2)}(k_b a_l))],$$

$$R_{2\nu}^{l0} = 0.25i\pi a_l\kappa_l(\varepsilon_s\varepsilon_l^{-1} - 1)H_\nu^{(2)}(k_b a_l)J_{\nu-1}(\kappa_l a_l),$$

$$R_{k\nu}^{l1} = R_{k\nu}^{l0} + 0.5i\pi\nu(1-\varepsilon_s\varepsilon_l^{-1})H_\nu^{(2)}(k_b a_l)J_\nu(\kappa_l a_l),$$

$$S_{l\nu}^{kp} = [H_\nu^{(2)}(k_b a_k)]^{-1}[J_\nu(k_b a_k)R_{l\nu}^{kp} + (2-l)J_\nu(\kappa_k a_k)],$$

$$A_\nu^{lp} = C_{l\nu}^{(x)} + (-1)^p iC_{l\nu}^{(y)}, \quad G_\nu^k = H_{-\nu}^{(2)}(k_b\rho_k)\exp(i\nu\varphi_k),$$

$$q = 1-p, \quad \sigma = 2(p-q),$$

and ρ_k and φ_k are the coordinates of the center of the kth hole. Relations (3) lead to the conditions $U_{l\nu}^{(p)} = 0$ representing an infinite system of algebraic equations with unknown coefficients $C_{l\nu}^{(x),(y)}$. The validity of these equations in the holes means compensation of the waves satisfying the Helmholtz equation

$$\nabla_x^2\delta H_{lp} + \nabla_y^2\delta H_{lp} + (k_0^2\varepsilon_s - \beta^2)\delta H_{lp} = 0.$$

This result is analogous to the Ewald–Oseen extinction theorem [12].

For the practical calculation of MOFs, let us retain in expansions (2) only the terms with $|\nu| \le m$, which is equivalent to solving Eqs. (1) by the method of quadratures [13]. In this approximation, conditions $U_{l\nu}^{(p)} = 0$ form a system of $2n(2m+1)$ homogeneous algebraic equations. The complex parameter β is determined from the condition that the system determinant is zero and can be calculated by means of the contour integration [14]. Then, the mode field is restored using Eqs. (1), (2), and the relations $H_z = (i\beta)^{-1}(\nabla_x H_x + \nabla_y H_y)$, $\mathbf{E} = (i\omega\varepsilon)^{-1}\nabla\times\mathbf{H}$ (following from the Maxwell equations).

In order to verify the proposed method, we have calculated the dispersion relations for the fundamental degenerate leaky H_x and H_y modes (the notation indicating the main magnetic field component) for the MOFs modeled by a hexagonal system of holes representing identical air-filled channels in a fused quartz matrix (Fig. 1). The results were compared to those obtained by the multipole method [7, Fig. 3]. All curves

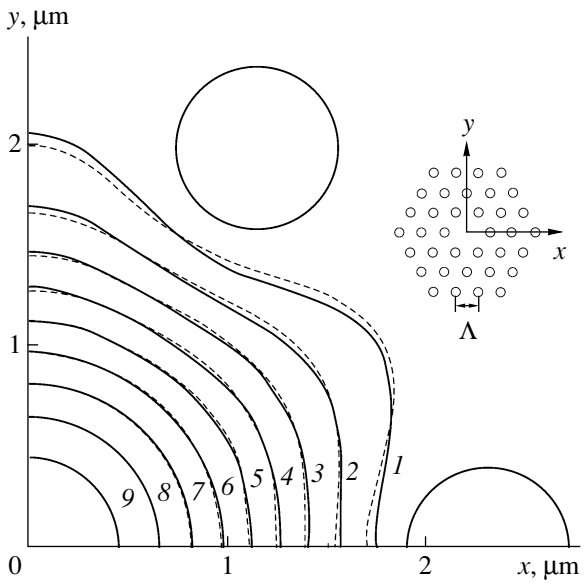

Fig. 1. The cross section quadrant of a MOF formed by three hexagonal rings of air-filled channels (inset) in a fused quartz matrix, showing the isolines of intensity for the H_x (solid curves) and H_y (dashed curves) leaky modes with $S_z(S_{z\,\max})^{-1} = 0.1$ (*1*), 0.2 (*2*), …, 0.9 (*9*).

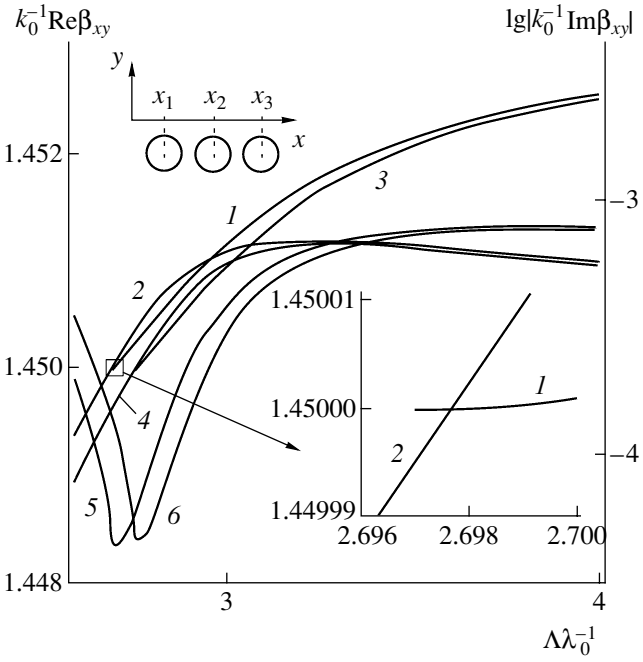

Fig. 2. The results of model calculations for a MOF with the central fiber rod and two air-filled channels (inset). The curves of (*1*, *2*) $\mathrm{Re}\beta_x(\Lambda)$, (*3*, *4*) $\mathrm{Re}\beta_y(\Lambda)$, (*5*) $\mathrm{Im}\beta_x(\Lambda)$, and (*6*) $\mathrm{Im}\beta_y(\Lambda)$ were calculated for $y_1 = y_2 = y_3$, $x_2 - x_1 = x_3 - x_2 = \Lambda$ (x_i, y_i are the coordinates of the ith hole center); $a_1 = a_2 = a_3 = 1.3\lambda_0$; $\varepsilon_1 = \varepsilon_3 = 1$, $\varepsilon_2 = (1.462)^2$, and $\varepsilon_s = (1.45)^2$. Curves *1* and *3* refer to the eigenmodes ($\mathrm{Re}k_b = 0$, $\mathrm{Im}k_b < 0$) and curves *2*, *4–6* refer to the leaky modes ($\mathrm{Re}k_b > 0$, $\mathrm{Im}k_b > 0$).

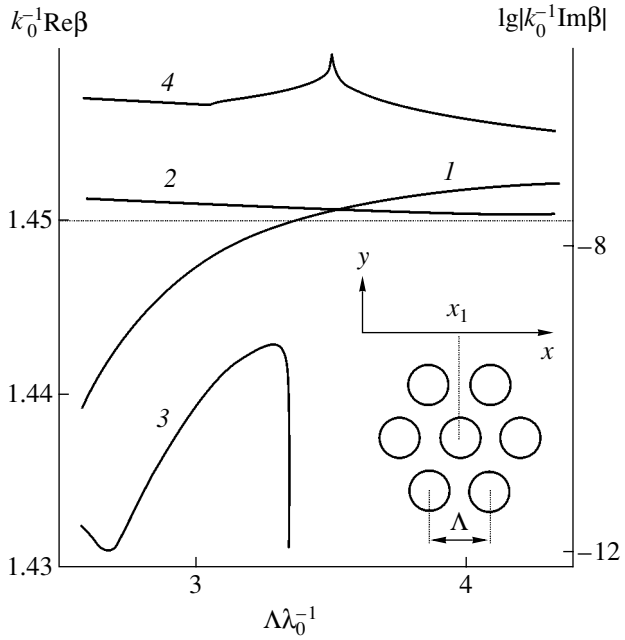

Fig. 3. The results of model calculations for a MOF with the central fiber rod and six air-filled channels forming a hexagonal ring (inset). The curves of (*1*, *2*) $\mathrm{Re}\beta(\Lambda)$ and (*3*, *4*) $\mathrm{Im}\beta(\Lambda)$ were calculated for $a_1 = a_2 = \ldots = a_7 = 1.3\lambda_0$; $\varepsilon_s = (1.45)^2$; $\varepsilon_1 = (1.462)^2$ (central hole); and $\varepsilon_2 = \varepsilon_3 = \ldots = \varepsilon_6 = 1$. Curves *1* and *3* refer to the fundamental eigenmode and fast leaky mode, respectively; curves *2* and *4* refer to the slow leaky mode.

obtained using the latter method coincide (to within the drawing scale) with our results.

It should be noted that, for the number of hexagonal rings $n_r = 3$ ($n = 36$) considered in [7] (Fig. 1), the modes can exhibit strong damping caused by leakage. In particular, the given n_r and $m \geq 8$, $\Lambda = 2.3$ μm (Λ is the distance between centers of the neighboring holes, see the inset in Fig. 1), $a_l = 0.175\Lambda$, $\varepsilon_l = 1$ ($l = 1, 2, \ldots, n$), $\lambda_0 = 1.0336$ μm, and $\varepsilon_s = (1.45)^2$ yield $k_0^{-1}\beta = 1.440529932 - i5.335 \times 10^{-7}$, which corresponds to a damping factor of 28.17 dB/m. In connection with this, we have studied the possibility of reducing the damping by increasing n_r. For the MOFs with $n_r = 5$ ($n = 90$) and $n_r = 7$ ($n = 168$), we obtain $k_0^{-1}\beta = 1.440530233 - i8.577 \times 10^{-10}$ (4.529×10^{-2} dB/m) and $k_0^{-1}\beta = 1.440530234 - i1.414 \times 10^{-12}$ (7.466×10^{-5} dB/m), respectively. It is interesting to note that the values of $\mathrm{Re}\beta$ for all n_r are almost identical, which is explained by good localization of the mode energy. This is evidenced by Fig. 1, showing quadrants of the symmetric distributions of the longitudinal component of the Poynting vector S_z calculated for the parameters indicated above (in the given scale, the patterns corresponding to $n_r = 3.5$ and 7 are indistinguishable).

According to the above results, obtaining acceptable mode damping in the model under consideration requires using MOFs with a large number of air-filled channels. In connection with this, it was of interest to study MOFs of a simpler design, comprising a central fiber rod surrounded by a relatively small number of air-filled channels. Such MOFs can guide the eigenmodes (rather than leaky modes), while still possessing interesting dispersion and polarization properties [5]. Let us consider the previously unstudied properties of the modes in such MOFs in the vicinity of critical conditions. Since Eqs. (1) are formulated in the internal regions of holes, calculations within the framework of the approach described above are performed without difficulties.

Figure 2 presents the results of calculations of the modes in a MOF with two air-filled channels, which obeys the condition (required in some applications [15]) that $\beta_x \neq \beta_y$, where β_x and β_y are the propagation constants of the H_x and H_y modes, respectively. This MOF can guide two (H_x and H_y) eigenmodes, which exhibit the cutoff at $\Lambda\lambda_0^{-1} = 2.69697$ and 2.75795 for $k_b \longrightarrow 0$ (corresponding to the termination of curves *1* and *3* in Fig. 2). Thus, the MOF under consideration is characterized by single mode and single polarization in the interval of $2.69697 < \Lambda\lambda_0^{-1} < 2.75795$. However, this MOF can also guide the leaky H_x and H_y modes. For $\Lambda\lambda_0^{-1} > 2.69768$ and $\Lambda\lambda_0^{-1} > 2.75855$, respectively, these modes (in contrast to the usual leaky modes [16, 17]) are slow ($\mathrm{Re}\beta_{x,y} > k_0\sqrt{\varepsilon_s}$). Over an extended interval of Λ, the real parts of the propagation constants of these modes are close to those of the eigenmodes (Fig. 2). Under these conditions, microscopic bendings of the fiber may cause an effective energy exchange between the modes, thus leading to significant damping of the radiation [16]. This mechanism of losses probably accounts for the low quality of experimental MOFs of the type under consideration [15].

The MOFs with a hexagonal ring of air-filled channels guiding the fundamental doubly degenerate modes exhibit different properties. According to Fig. 3, showing data for a particular MOF of this type, the fundamental eigenmodes exhibit a continuous transition to a fast ($\mathrm{Re}\beta < k_0\sqrt{\varepsilon_s}$) leaky mode at $\Lambda\lambda_0^{-1} = 3.34031$. At the same time, this MOF can guide a slow leaky mode possessing maximum damping under the conditions of phase synchronism with the eigenmode (Fig. 3). In the absence of such synchronism, an effective energy exchange between the slow leaky mode and eigenmodes can be provided by using a diffraction grating with an appropriate period formed in the MOF core. Such experiments were recently reported in [1].

In conclusion, it should be noted that, according to the results of calculations, the properties of MOFs of the types considered in this paper can be significantly

modified by changing the parameters of the structures. However, the main qualitative features established above, such as the existence of slow leaky modes, are retained. Allowance for these modes may be significant, for example, in designing highly sensitive optical sensors.

REFERENCES

1. C. Kerbage and B. J. Eggleton, Opt. Photonics News **13** (9), 38 (2002).
2. T. M. Monro, D. J. Richardson, N. G. R. Broderick, *et al.*, J. Lightwave Technol. **17**, 1093 (1999).
3. D. Mogilevtsev, T. A. Birks, and P. S. J. Russel, J. Lightwave Technol. **17**, 2078 (1999).
4. A. Ferrando, E. Silvestre, J. J. Miret, *et al.*, Opt. Lett. **24** (1), 276 (1999).
5. Z. Zhu and T. G. Brown, Opt. Commun. **206**, 333 (2002).
6. T. P. White, B. T. Kuhlmey, R. C. McPhedran, *et al.*, J. Opt. Soc. Am. B **19**, 2322 (2002).
7. B. T. Kuhlmey, T. P. White, G. Renversez, *et al.*, J. Opt. Soc. Am. B **19**, 2331 (2002).
8. A. V. Belov and E. M. Dianov, Kvantovaya Élektron. (Moscow) **32**, 641 (2002).
9. Z. Zhu and T. G. Brown, Opt. Express **10**, 853 (2002).
10. A. B. Sotsky and L. I. Sotskaya, Opt. Spektrosk. **88**, 465 (2000) [Opt. Spectrosc. **88**, 415 (2000)].
11. *Handbook of Mathematical Functions*, Ed. by M. Abramowitz and I. A. Stegun (National Bureau of Standards, Washington, 1964; Nauka, Moscow, 1979).
12. M. Born and E. Wolf, *Principles of Optics*, 4th ed. (Pergamon Press, Oxford, 1969; Nauka, Moscow, 1973).
13. V. I. Krylov, V. V. Bobkov, and P. I. Monastyrnyĭ, *Computational Methods* (Nauka, Moscow, 1977), Vol. 2.
14. A. B. Sotsky, Dokl. Akad. Nauk Belarusi **45** (3), 19 (2001).
15. K. Hayata, M. Eguchi, M. Koshiba, *et al.*, J. Lightwave Technol. **4**, 1090 (1986).
16. A. W. Snyder and J. D. Love, *Optical Fiber Theory* (Chapman and Hall, London, 1983; Radio i Svyaz', Moscow, 1987).
17. L. A. Vaĭnshteĭn, *Electromagnetic Waves* (Radio i Svyaz', Moscow, 1988).

Translated by P. Pozdeev

Technical Physics Letters, Vol. 29, No. 9, 2003, pp. 768–770. Translated from Pis'ma v Zhurnal Tekhnicheskoĭ Fiziki, Vol. 29, No. 18, 2003, pp. 46–53.

Nonlinear Electrocapillary Waves on a Charged Surface of the Ideal Liquid

D. F. Belonozhko and A. I. Grigor'ev*

Yaroslavl State University, Yaroslavl, Russia

**e-mail: grig@uniyar.ac.ru*

Received April 21, 2003

Abstract—An analytical expression for the profile of a plane wave traveling over a charged surface of the ideal incompressible liquid under the action of surface tension and gravity is obtained in the second order of smallness with respect to the wave motion amplitude. An analysis of this expression shows that, for a certain fixed value of the surface charge density (subcritical from the standpoint of realization of the Tonks–Frenkel instability), the wave profiles are qualitatively different from those of nonlinear capillary-gravitational waves existing on the uncharged liquid surface (for this reason, the obtained wave branch can be called electrocapillary). © *2003 MAIK "Nauka/Interperiodica".*

Introduction. Despite the long history and considerable achievements of investigations into periodic capillary-gravitational waves of finite amplitude on the surface of the ideal incompressible liquid [1, 2], the number of papers devoted to nonlinear waves on the charged surface of an electrically conducting liquid is still rather restricted. These investigations [3–5] were mostly aimed at obtaining solutions in the form of solitary waves, while questions pertaining to the periodic capillary-gravitational waves and the role of surface charging in the formation of their profiles remained unstudied.

The present study is devoted to these questions. Our aim is to determine a stationary profile of the periodic capillary-gravitational traveling wave remaining unchanged in the course of the wave propagation. The problem will be solved in the second order of smallness with respect to the wave amplitude (the latter assumed to be small relative to the wavelength). Note that a purely sinusoidal wave profile is not stationary in this approximation [1, 2].

Formulation of the problem. Consider the ideal, incompressible electrically conducting liquid with the density ρ, the kinematic viscosity ν, and surface tension γ occupying the half-space $z \le 0$ and occurring under the action of a gravitational field $\mathbf{g}$. We use the cartesian coordinate system $0xyz$, in which the plane $z = 0$ coincides with the unperturbed liquid surface and the surface normal is parallel to the gravity force ($\mathbf{n}_z \| -\mathbf{g}$). The stationary profile of a nonlinear periodic capillary-gravitational wave with the wavelength λ traveling over the free liquid surface bearing the homogeneous surface charge density κ is described by the following system of equations:

$$z \le \xi: \Delta\varphi = 0; \quad p = -\rho g z - \rho\frac{\partial\Phi}{\partial t} - \frac{\rho}{2}(\mathrm{grad}\varphi)^2;$$

$$\xi > 0: \Delta\Phi = 0;$$

$$z = \xi: \frac{\partial\xi}{\partial t} + \frac{\partial\varphi}{\partial x}\frac{\partial\xi}{\partial x} = \frac{\partial\varphi}{\partial z};$$

$$p + \frac{(\nabla\Phi)^2}{8\pi} = -\gamma\frac{\partial^2\xi}{\partial x^2}\left(1 + \left(\frac{\partial\xi}{\partial x}\right)^2\right)^{-3/2}; \quad \Phi = 0;$$

$$z \longrightarrow \infty: \mathrm{grad}\Phi = -4\pi\kappa \cdot \mathbf{n}_z;$$

$$z \longrightarrow -\infty: \mathrm{grad}\varphi = 0.$$

Here, the wave profile $\xi = \xi(x, t)$ represents deviation of the free liquid surface from the equilibrium shape $z = 0$, $\varphi(\mathbf{r}, t)$ is the liquid velocity field potential, and $\Phi(\mathbf{r}, t)$ is the electric potential over the liquid surface.

Solution of the problem. By solving the above problem using the classical methods (developed in the theory of nonlinear periodic waves—see, e.g., [1, 6, 7]) in the second order of smallness with respect to the wave amplitude a (assumed to be small relative to the wavelength), we determine the shape of a nonlinear capillary-gravitational wave traveling over the liquid surface

$$\xi = a\cos(\omega t - kx) + a^2 k\Lambda\cos[2(\omega t - kx)];$$

$$\omega^2 = gk(1 + \alpha^2k^2 - \alpha kW); \quad W = \frac{4\pi\kappa^2}{\sqrt{\rho g\gamma}}; \qquad (1)$$

$$\Lambda = \frac{(1 + \alpha^2k^2 - 2\alpha kW)}{4(0.5 - \alpha^2k^2)}; \quad \alpha = \sqrt{\frac{\gamma}{\rho g}};$$

1063-7850/03/2909-0768$24.00

where α is the capillary constant and $k = 2\pi/\lambda$ is the wavenumber. The first term in solution (1) represents the well-known solution of the problem obtained in the approximation linear with respect to the amplitude. The amplitude a is considered as preset by appropriately selected initial conditions.

Results and discussion. Figure 1 shows the behavior of the dimensionless factor Λ determining the amplitude of the second-order correction in the wave profile (1), plotted as a function of the dimensionless wavenumber αk for various values of the Tonks–Frenkel parameter W.

As can be seen from expression (1), the amplitude coefficient Λ in the second term exhibits a resonance form: at $k = k_* = 1/\alpha\sqrt{2}$, the denominator of this term goes to zero and the second-order correction tends to infinity. For the uncharged liquid surface, this phenomenon was studied by Nayfeh [6]. In contrast to this case, the numerator of expression for Λ in our Eq. (1) contains a negative term with the parameter W. This dimensionless quantity characterizes stability of a charged liquid surface with respect to the pressure produced by the intrinsic surface charge: the Tonks–Frenkel instability is developed for $W \geq 2$ [8]. This implies that Λ can remain finite even when the denominator tends to zero, provided certain relations between the physical parameters hold.

The denominator of Λ tends to zero as $k \longrightarrow k_*$. However, for $W = W_* = 3/(2\sqrt{2}) \approx 1.06$, the numerator of Λ will also tend to zero during this limiting transition. Eventually, for $W = W_*$, the Λ value in the limit of $k \longrightarrow k_*$ behaves as uncertainty of the 0/0 type which, eliminated using the L'Hospital rule, yields $\Lambda = 1/8$. In this case, the plot of $\Lambda = \Lambda_*(\alpha k)$ becomes continuous (see dashed curve in Fig. 1).

Note that, irrespective of the W value, expansion (1) ceases to adequately represent the problem solution when k approaches k^*, since the correction quadratic in dimensionless amplitude a becomes greater than the term linear with respect to a. In connection with this, it would be interesting to estimate the role of viscosity, which is an important factor in resonance phenomena. The estimates will be obtained for water, which has $d = 0.27$ cm.

According to our previous results [9, 10], obtained for nonlinear waves on an uncharged liquid surface, the effect of viscosity on the wave profile in water becomes significant in the interval of $\alpha k \in D = (0.6; 07)$. At the boundaries of this interval, the amplitude of the second-order correction determined with neglect of viscosity is overstated by within several percent, but for $k \longrightarrow k_*$ this difference tends to infinity. Outside the above interval, the models of viscous and nonviscous water give quite consistent results. In this context, the following analysis will refer to the waves with $\alpha k \notin D$ for $W < 2$. The parts of the plots in Fig. 1 corresponding to the interval D are deprived of physical meaning because the initial model ignoring viscosity ceases to be valid in this region.

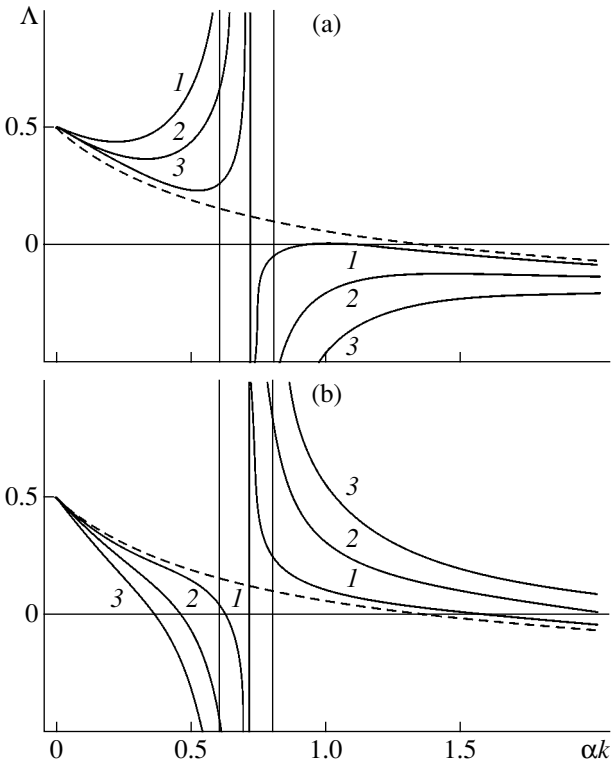

Fig. 1. Plots of the dimensionless factor Λ determining the amplitude of the second-order correction versus dimensionless wavenumber αk for various values of the surface charge density parameter W: (a) $W = W_* - 0.05$ (*1*), $W_* - 0.25$ (*2*), $W_* - 0.5$ (*3*); (b) $W = W_* + 0.05$ (*1*), $W_* + 0.25$ (*2*), $W_* + 0.5$ (*3*); dashed curve corresponds to $W = W_* = 3/(2\sqrt{2})$.

As can be seen from Fig. 1, physically reasonable parts of the $\Lambda = \Lambda(\alpha k)$ plots tend to the curves $\Lambda = \Lambda_*(\alpha k)$ in the limit of $W \longrightarrow W_*$. Therefore, the value of $W = W_*$ can be naturally considered as a threshold separating the wave motions of different types. At this point, the asymptotic value of Λ in the limit of $k \longrightarrow k_*$ changes sign. According to expression (1), the second-order correction to the linear part for $k \neq k_*$ tends to zero as $W \longrightarrow W_*$.

Figure 1a shows a family of the $\Lambda = \Lambda(\alpha k)$ curves constructed for various values of $W \leq W_*$. In this region of the Tonks–Frenkel parameter, the amplitude of the second-order correction as a function of the wavenumber behaves like that for the uncharged liquid surface: the wave motion is characterized by profiles with sharp vertices for the long waves ($k < k_*$) and with rounded vertices for the short waves ($k > k_*$) (for more details,

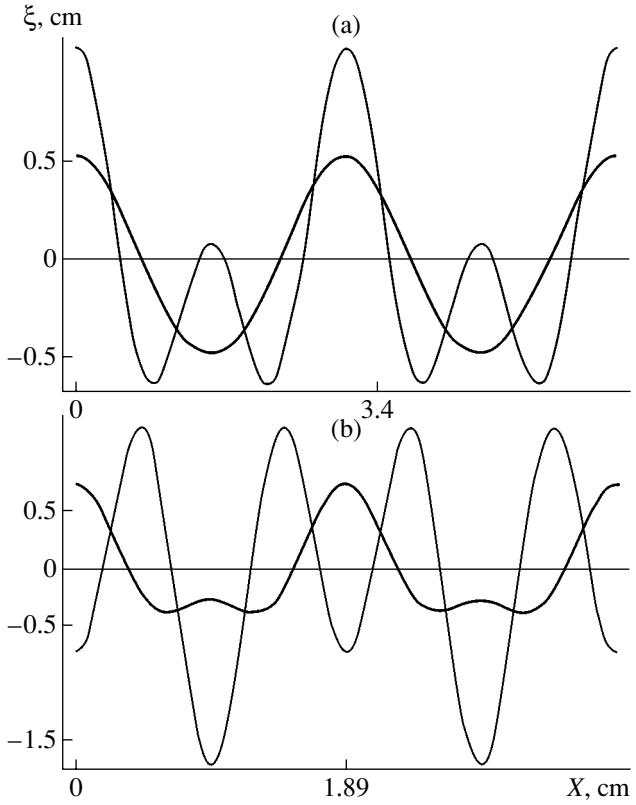

Fig. 2. Wave profiles on the uncharged ($W = 0$, thin solid curves) and charged ($W = 1.2$, thick solid curves) surface of water, calculated using formula (1) for the dimensionless wavenumbers $\alpha k = 0.5$ (a) and 0.9 (b).

see [6]). According to [6], this wave motion is naturally referred to as capillary-gravitational upon expansion to the case of waves on a charged surface.

Figure 1b presents the plots of $\Lambda = \Lambda(\alpha k)$ calculated for various values of Tonks–Frenkel parameter in the interval $W_* \le W < 2$. As can be seen, These curves are in a certain sense inverse to those depicted in Fig. 1a. Indeed, the right-hand (physically reliable) parts of the curves, corresponding to short waves, are positive within a rather large region to the right from point $k = k_*$ (rather than negative as the curves in Fig. 1a). The right-hand branch of curve *1* enters the region of negative Λ values at a sufficiently long distance from the point $k = k_*$. For this reason, the nonlinear waves corresponding to these curves can be interpreted as a new, previously undescribed type of periodic wave motion on the ideal liquid surface; the appearance of these waves is related to the presence of a surface charge.

Figure 2 shows profiles of the new waves in comparison to those on the uncharged liquid surface. As can be readily seen, the shapes of the capillary-gravitational waves on the charged and uncharged surfaces are significantly different. The new waves existing on the charged surface of the ideal incompressible liquid are naturally called electrocapillary-gravitational or simply electrocapillary (ignoring the gravitational effects weak in the wavelength range under consideration).

Conclusions. Nonlinear waves on a charged surface of the ideal incompressible electrically conducting liquid are qualitatively different from the nonlinear wave motion on the uncharged surface of the same liquid. The curvature of the vertices of the electrocapillary waves increases with the surface charge density (i.e., with increasing parameter W) for $W_* < W \longrightarrow 2$. It is interesting to note that this behavior is observed for subcritical (from the standpoint of realization of the Tonks–Frenkel instability) W values. To our knowledge, this effect has not yet reported, although the curvature of waves on an unstable charged liquid surfaces was studied rather extensively (see, e.g., [5, 11–15]). Another interesting result is that, for $W \longrightarrow W_*$, the electric charge becomes a factor decreasing the efficiency of the nonlinear interaction of waves on the free liquid surface, since the second-order term tends to zero.

Acknowledgments. This study was supported by the Russian Foundation for Basic Research, project no. 03-01-00760.

REFERENCES

1. J. J. Stoker, *Water Waves* (Wiley, New York, 1957; Inostrannaya Literatura, Moscow, 1959).
2. G. B. Whitham, *Linear and Nonlinear Waves* (Wiley, New York, 1974; Mir, Moscow, 1977).
3. A. I. Zhakin, Izv. Akad. Nauk SSSR, Mekh. Zhidk. Gaza **3**, 94 (1984).
4. A. Gonzalez and A. Castellanos, Phys. Rev. E **49**, 2935 (1994).
5. N. M. Zubarev, Zh. Éksp. Teor. Fiz. **116**, 1990 (1999) [JETP **89**, 1078 (1999)].
6. A. H. Nayfeh, J. Fluid Mech. **48**, 385 (1971).
7. A. H. Nayfeh, *Perturbation Methods* (Wiley, New York, 1973; Mir, Moscow, 1976).
8. Ya. I. Frenkel', Zh. Éksp. Teor. Fiz. **6**, 348 (1936).
9. D. F. Belonozhko, A. I. Grigor'ev, and S. O. Shiryaeva, Pis'ma Zh. Tekh. Fiz. **28** (19), 1 (2002) [Tech. Phys. Lett. **28**, 795 (2002)].
10. D. F. Belonozhko and A. I. Grigor'ev, Zh. Tekh. Fiz. **73** (4), 28 (2003) [Tech. Phys. **48**, 404 (2003)].
11. M. D. Gabovich, Usp. Fiz. Nauk **140**, 137 (1983) [Sov. Phys. Usp. **26**, 447 (1983)].
12. M. L. Aleksandrov, L. N. Gall', V. Ya. Ivanov, *et al.*, Izv. Akad. Nauk SSSR, Mekh. Zhidk. Gaza **6**, 165 (1983).
13. J. E. Allen, J. Phys. D **18**, 59 (1985).
14. S. I. Shevchenko, Zh. Tekh. Fiz. **60** (2), 54 (1990) [Sov. Phys. Tech. Phys. **35**, 167 (1990)].
15. A. I. Grigor'ev and S. O. Shiryaeva, Inzh.-Fiz. Zh. **60**, 632 (1991).

Translated by P. Pozdeev

Technical Physics Letters, Vol. 29, No. 9, 2003, pp. 771–774. Translated from Pis'ma v Zhurnal Tekhnicheskoĭ Fiziki, Vol. 29, No. 18, 2003, pp. 54–60.

Nonlinear Dynamics of a Plasma Torch Generated by a Laser Pulse of Large Width

G. A. Mesyats, V. V. Osipov, N. B. Volkov*, V. V. Platonov, and M. G. Ivanov

Institute of Electrophysics, Ural Division, Russian Academy of Sciences, Yekaterinburg, Russia

** e-mail: nbv@ami.uran.ru*

Received April 17, 2003

Abstract—Experimental data on the nonlinear dynamics of a plasma torch generated by a laser pulse of large width acting upon a graphite target are presented and discussed. The mushroom shape of the luminous region and the duration of emission observed in experiment are explained by the development of the Richtmyer–Meshkov instability at the carbon plasma–air interface and by the formation of nanoparticles in the plasma expanding into the buffer gas. © *2003 MAIK "Nauka/Interperiodica".*

In recent years, the extensive development of nanotechnology has stimulated the interest in physical processes involved in the synthesis of nanodimensional powders and the deposition of thin films with the aid of continuous and periodic pulsed lasers [1–3]. These processes are preceded by the formation of a plasma torch as a result of evaporation of the target material under the action of a focused laser beam. In some experiments [1, 4], conditions were established for which up to 97–100% of the target material in vapor form was transferred to the plasma torch. This is evidenced by the small size and spherical shape of nanoparticles in the synthesized powder [3]. Despite this, sufficiently homogeneous coatings are not obtained upon deposition of the laser-ablated material onto substrate surfaces in the atmosphere [4]. Another unexplained fact is that the average size of nanoparticles formed under the action of a periodic pulsed laser radiation is one-fourth of that obtained using a CW laser [1, 3]. In connection with these problems, it necessary to study the characteristics and dynamics of a plasma torch generated under the conditions of laser-induced evaporation.

This paper presents the results of experimental and theoretical investigation of the dynamics of a plasma torch generated by a focused beam of a periodic pulsed CO_2 laser of the LAERT type [3, 5], excited by a combined discharge, upon a flat target made of graphite or YSZ. The experiments were performed under the conditions close to those used for the synthesis of nanopowders [3] and the deposition of thin films in the atmosphere [4]. Multimode radiation of the LAERT CO_2 laser with an output beam cross section of 3×4 cm was focused on a flat target by a KCl lens with a focal length of 10 cm. The focal spot had an elliptical shape with the axial dimensions 0.6 and 0.7 mm. Laser pulses with a full width at half maximum (FWHM) of 200 μs was incident onto the target surface at angle of 45°. The emission from a laser-induced plasma torch was photographed by a high-speed photoregistrator of the VFU-1 type within a time interval between shots of 11 μs and an exposure period of ~1 μs.

Figure 1 shows a sequence of patterns of the emission from a plasma torch generated at a graphite target under the action of a laser radiation pulse. An analysis of this series reveals two important facts, which have to be considered in some detail.

(1) In the course of the process, a luminous region of the plasma torch acquires the typical mushroom shape and exhibits a complicated internal structure varying with time.

(2) The duration of emission from the plasma torch significantly exceeds the laser pulse width (FWHM). Here, it should be noted that emission from a plasma torch for a time significantly exceeding the laser pulse width was also observed during the formation of laser nanotubes by laser ablation of a graphite target [6].

As can be seen from Fig. 1, a bright column connecting cloud with the target exhibits a break at t = 328 μs that terminates energy supply to the cloud (see Fig. 1 for t = 343 μs). Thus, during the subsequent registration period (over ~100 μs, but actually much longer), the luminous cloud is independent of the physical processes occurring on the target surface. In order to find the reasons for this behavior of the plasma torch, let us obtain some estimates based on the published characteristics of graphite [7–10]: density, $\rho = 1.89 \times 10^3$ kg/m^3; cohesion (sublimation) energy, E_s = 5.9787×10 J/kg; atomic weight, A = 12; resistivity (averaged over the temperature interval from 300 to 3000 K), $\rho_e = 10.183 \times 10^{-6}$ Ω m. A real pulse of the laser radiation with a wavelength of $\lambda = 10.6$ μm, a circular frequency of $\omega = 1.77826 \times 10^{14}$ s^{-1}, and a total energy of E_L = 1.5 J will be replaced by a rectangular

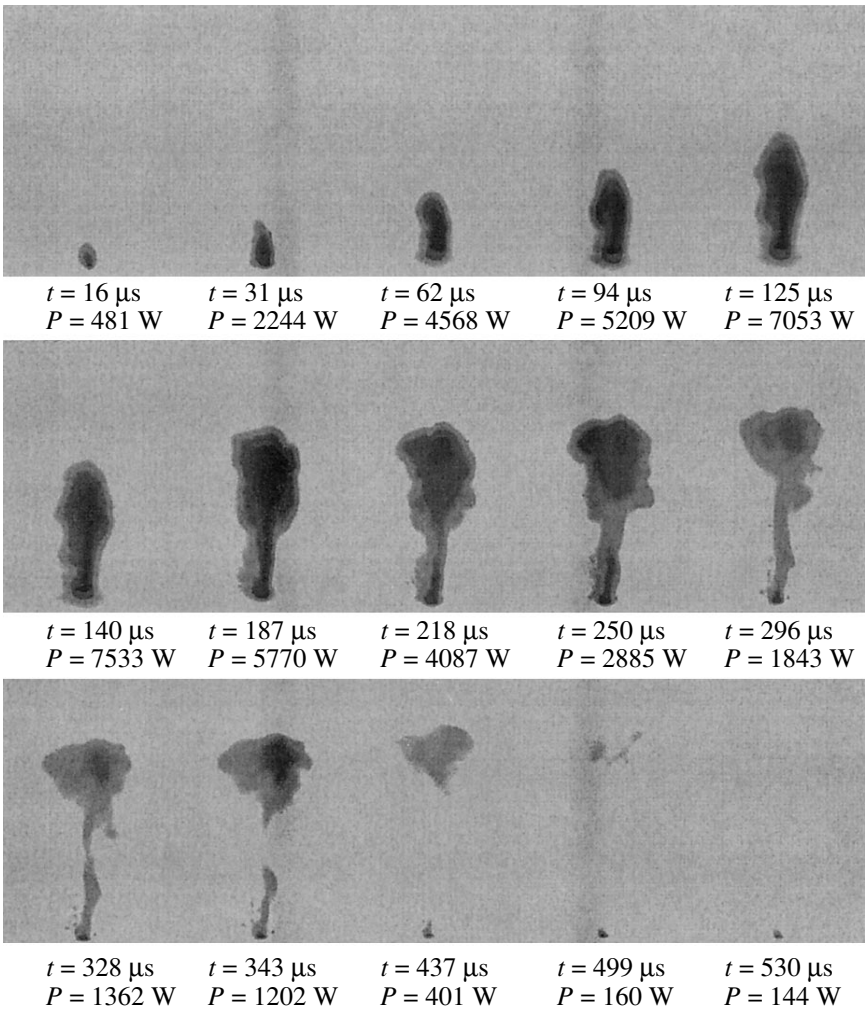

Fig. 1. A sequence of photographs of the emission from a plasma torch generated by a laser pulse of large width.

pulse with a power of $P_m = 7.5$ kW (corresponding to a power density of $Q_m = 3.81972 \times 10^1$ W/m^2) and a width of $\tau_p = 200$ μs. Assuming for the sake of simplicity that the energy source is situated entirely on the target surface, we estimate the velocity of the target–vapor phase boundary [11] at $D_s = 0.338036$ m/s. The thickness of the graphite layer evaporated during the laser pulse action amounts to $\Delta_p = D_s\tau_p = 67.6072$ μm. The electromagnetic field (radiation) penetration depth is $\delta_s = 0.3$ μm $\ll \Delta_p$ (i.e., the above assumption concerning the surface character of the energy source is valid with a high precision).

For the surface energy source, the propagating phase boundary obeys the Jouguet condition $D_s = u - c$ (where u is the hydrodynamic flow velocity and c is the sound velocity behind the discontinuity) [11]. Assuming the vapor to be ideal at both $T_1 = 3000$ K and $T_2 = 4000$ K, the corresponding substance ejection velocities are $u_1 = 1859.94$ m/s and $u_2 = 2147.73$ m/s. Assuming also that the jet propagates without drag over a distance on the order of the laser spot size d_p, the corresponding propagation timed can be estimated at $\tau_1 = 268.826$ ns and $\tau_2 = 232.804$ ns.

Using the above estimates of the time for which the plasma jet height is equal to the focused laser spot size and the experimentally measured height of the luminous region of the plasma torch on the symmetry axis, we evaluated the change in the jet acceleration with time (Fig. 2). As can be seen, the plasma torch is decelerated beginning with a time of about 300 ns (acceleration is directed toward the target). Therefore, this time corresponds to the onset of conditions favoring the development of the Richtmyer–Meshkov instability [12, 13] that is responsible for the formation of a mushroom-shaped (vortex) plasma torch [14] and the related complicated dynamics.

The fact of prolonged emission from the plasma torch, despite termination of the energy supply at 328 μs (Fig. 1), we explain by the Planck emission from strongly heated nanoparticles. In order to confirm

this hypothesis, we performed experiments in which the same graphite target was exposed to pulses of a TEA CO_2 laser with a duration of 1.5 μs and a peak power of 9×10^4 W (FWHM = 50 ns; 20 mJ). The radiation, normally incident on the target, was focused into a spot with a diameter of 0.2 mm. A slit scan of the emission from the plasma torch was obtained using a photoregistrator of the FER-7 type capable of determining the time intervals to within $\Delta t = \pm 0.1$ μs and the spatial coordinates to within $\Delta l = \pm 0.05$ mm. In order to reduce the energy supplied to the target at a high laser power level, we employed optical breakdown in the target material vapor. A minimum time to the optical breakdown was 40 ns. The time of the breakdown onset was detected by the appearance of the N_2^+ line (λ = 470.9 nm) using a setup comprising a monochromator (MSD-1), a photomultiplier (FEU-79), and an oscillograph. From these data, we estimated the energy supplied to the target at ~4 mJ.

Figure 3 shows the slit scan of the emission from a plasma torch generated as described above. As can be seen, the emission appears initially at a distance of 0.5 mm from the target surface. The plasma boundary is unstable and the emission duration virtually coincides with the laser pulse width. The maximum size (1.28 mm) of the plasma torch corresponds to $t \sim 1$ μs.

Once the characteristic energy of the laser radiation supplied to the target, the focal spot size, and crater depth were known, we could estimate the average density of carbon atoms at the torch opening. For T = 3000 K, this value amounts to $n_C = 4.594 \times 10^{16}$ cm^{-3}, which is 245 times smaller than the average density of molecules in the air ($n_{O_2} = 1.128 \times 10^{19}$ cm^{-3}). This circumstance hinders the formation of nanoparticles and, hence, the time of emission from the plasma cannot exceed the laser pulse width by more than the lifetime of excited states (~10^{-7} s), in complete agreement with our experiment.

A significantly different situation takes place when the same target is exposed to a long radiation pulse with an energy of 1.5 J and a power level selected so as to avoid the optical breakdown. In this case, the amount of carbon delivered to the plasma torch was 2.51×10^{-8} kg, which corresponds to a density of carbon atoms at the torch opening $n_C = (1.49–1.72) \times 10^{19}$ cm^{-3}. Since $n_C > n_{O_2}$, the plasma torch expansion into the buffer gas (air) was accompanied by the effective formation of nanoparticles. This factor determines the prolonged emission from the plasma torch observed in this experiment.

Thus, we believe that the shape of the laser-generated plasma torch and the structure of emission from this plasma are determined by the development of the Richtmyer–Meshkov instability at the carbon plasma–air interface, while the duration of emission is determined by the presence of strongly heated ultradisperse particles in the expanding plasma.

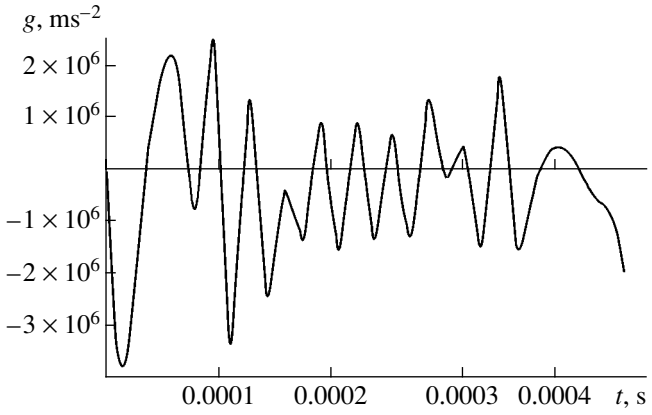

Fig. 2. The dynamics of acceleration of the boundary of emitting region on the plasma torch symmetry axis.

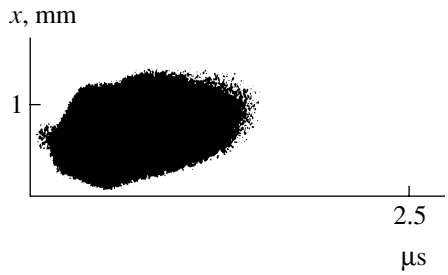

Fig. 3. A slit scan of the emission from a plasma torch generated by a laser pulse of small width.

Acknowledgments. This study was supported in part by the Presidium of the Urals Division of the Russian Academy of Sciences (project "Generation of High-Power Fluxes of Coherent Radiation and Its Use in the Development of Novel Technologies") within the framework of cooperation between the Urals Division and the Siberian Division of the Russian Academy of Sciences.

REFERENCES

1. E. Muller, Ch. Oestreich, U. Popp, *et al.*, Kona (Hirakata, Jpn.), No. 13, 79 (1995).
2. U. Popp, R. Herbig, G. Michel, *et al.*, J. Eur. Ceram. Soc. **18**, 1153 (1998).
3. Yu. A. Kotov, V. V. Osipov, M. G. Ivanov, *et al.*, Zh. Tekh. Fiz. **72** (11), 76 (2002) [Tech. Phys. **47**, 1420 (2002)].
4. V. V. Osipov, M. G. Ivanov, K. V. Molochkov, *et al.*, in *Proceedings of the 5th Conference on Physical Chemistry of Ultradisperse Systems, Yekaterinburg, 2001* (Inst. Fiz. Met., Ural. Otd. Ross. Akad. Nauk, Yekaterinburg, 2001), part 2, p. 231.

5. V. V. Osipov, M. G. Ivanov, V. V. Lisenkov, *et al.*, Kvantovaya Élektron. (Moscow) **32**, 253 (2002).
6. F. Kokai, K. Takahashi, M. Yudasaka, and S. Iijima, J. Phys. Chem. B **104**, 6777 (2000).
7. T. Nichikawa, H. Nakano, N. Uesugi, *et al.*, Appl. Phys. Lett. **75**, 4079 (1999).
8. A. Ubbelohde and F. Lewis, *Graphite and Its Crystal Compounds* (Clarendon Press, Oxford, 1960; Mir, Moscow, 1965).
9. *Properties of Carbon-Based Constructional Materials: A Handbook*, Ed. by V. P. Sosedov (Metallurgiya, Moscow, 1975).
10. C. Kittel, *Introduction to Solid State Physics*, 5th ed. (Wiley, New York, 1976; Nauka, Moscow, 1978).
11. Yu. V. Afanas'ev and O. N. Krokhin, in *The Physics of High Energy Densities*, Ed. by P. Caldirola and H. Knoepfel (Academic Press, New York, 1971; Mir, Moscow, 1974).
12. R. D. Richtmyer, Commun. Pure Appl. Math. **12**, 297 (1960).
13. E. E. Meshkov, Izv. Akad. Nauk SSSR, Mekh. Zhidk. Gaza **5**, 151 (1969).
14. N. B. Volkov, A. E. Maĭer, and A. P. Yalovets, Zh. Tekh. Fiz. **73** (3), 1 (2003) [Tech. Phys. **48**, 275 (2003)].

Translated by P. Pozdeev

Technical Physics Letters, Vol. 29, No. 9, 2003, pp. 775–778. Translated from Pis'ma v Zhurnal Tekhnicheskoĭ Fiziki, Vol. 29, No. 18, 2003, pp. 61–69.

Adaptive Wavelets Applied to the Analysis of Nonlinear Systems with Chaotic Dynamics

V. A. Gusev, A. A. Koronovskiĭ, and A. E. Khramov*

Saratov State University, Saratov, Russia
State Scientific Center "College", Saratov, Russia
**e-mail: aeh@cas.ssu.runnet.ru*

Received April 10, 2003

Abstract—We consider an approach to the analysis of nonstationary processes based on the application of wavelet basis sets constructed using segments of the analyzed time series. The proposed method is applied to the analysis of time series generated by a nonlinear system with and without noise. © *2003 MAIK "Nauka/Interperiodica".*

As is known, the analysis of nonlinear dynamic systems of various natures featuring complicated oscillatory regimes requires special methods [1–4]. Among these methods, of special interest is the wavelet analysis [5–7] offering a powerful means of diagnostics of the behavior of nonlinear dynamic systems [5, 8, 9]. Presently, wavelets are successfully applied to the analysis of nonstationary signals generated by systems of a biological and medical nature [10, 11], geophysical processes [5, 12], electron-plasma systems [4, 13, 14], chaotic and turbulent processes [7, 15–17], etc. An important modification of the wavelet analysis consists in using specially constructed (adaptive) wavelet basis sets, which allows the analysis to reveal certain features of the analyzed signals [8, 18].

In this paper, we describe a new approach to the analysis of time series generated by nonlinear processes. The proposed method is based on the use of adaptive wavelet basis sets constructed using segments of the analyzed time series, which facilitates the separation of characteristic features and structures from signals (even in the presence of noise).

The continuous wavelet transform of a function $x(t)$ is defined as [5–7]

$$W(t, s) = \frac{1}{\sqrt{s}}\int_{-\infty}^{+\infty} x(t')\psi^*\left(\frac{t-t'}{s}\right)dt', \qquad (1)$$

where s is the analyzed time scale and ψ is the base wavelet function (the asterisk denotes complex conjugation). The latter function, although it can be selected rather arbitrarily, must satisfy certain requirements [5, 6, 8], the most important of which are as follows. First, the base wavelet function should be localized in both time and space representations; second, this function has to obey the condition of zero mean $\int_{-\infty}^{+\infty}\psi(t)dt = 0$ or an equivalent relation $\hat{\psi}(0) = 0$, where $\hat{\psi}$ is the Fourier transform of the base wavelet function.

Let us assume that the signal $x(t)$ is generated by a nonlinear dynamic system occurring in an oscillatory regime (in particular, in the state of dynamic chaos). Consider the following procedure for constructing a complex wavelet function ψ using the given time series $x(t)$.

First, we separate the characteristic time scale τ (with the corresponding frequency $\omega_\tau = 2\pi/\tau$) of the nonstationary process $x(t)$. In the case of periodic oscillations, τ coincides with the period. For a chaotic nonregular signal, τ can be defined by various means. For example, if the chaotic signal $x(t)$ is characterized by the phase Φ determined using the Hilbert transform [2], the characteristic frequency can be defined as $\omega_\tau = \lim_{t\to\infty}\Phi(t)/t$. In the simplest case, the frequency ω_τ can be determined as corresponding to the most intense peak in the Fourier spectrum of power $P(\omega)$ of the signal $x(t)$.

Second, we select a certain initial moment t_0 in the time series $x(t)$, relative to which the wavelet basis set will be constructed. The real and imaginary parts of the base wavelet function ψ are constructed according to the formulas

$$\begin{aligned}\mathrm{Re}\psi(t) &= \pi^{-1/4}\left\langle x(t-t_0)\exp\left(-\frac{1}{2}\frac{(t-t_0)^p}{(n\tau)^p}\right)\right\rangle,\\ \mathrm{Im}\psi(t) &= \pi^{-1/4}\left\langle x(t-t_0+\tau/2)\exp\left(-\frac{1}{2}\frac{(t-t_0)^p}{(n\tau)^p}\right)\right\rangle,\end{aligned} \qquad (2)$$

where $\langle\cdot\rangle$ denotes the operation of elimination of the mean value for satisfying the zero mean condition; n

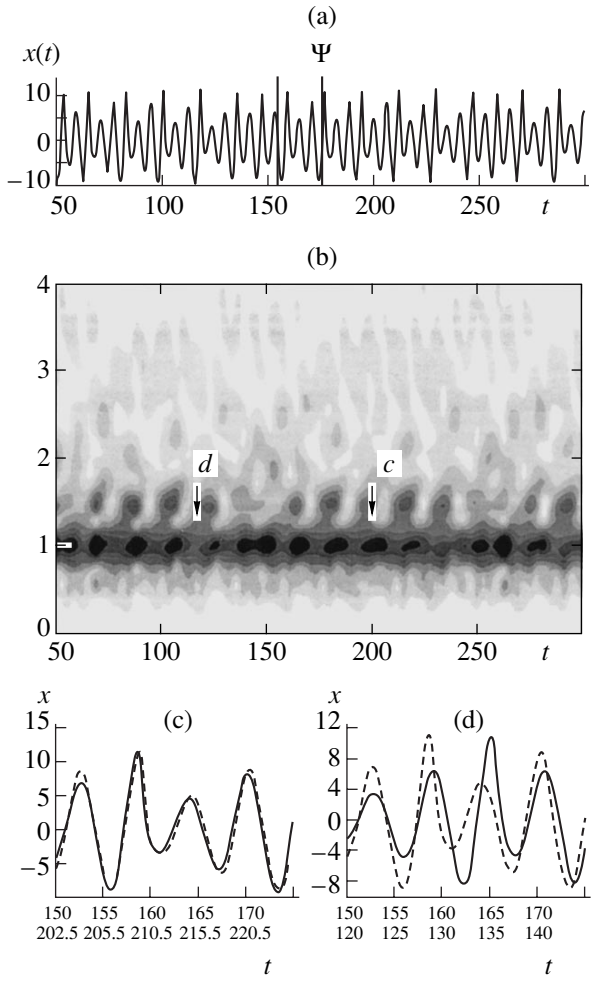

Fig. 1. Wavelet analysis of a noiseless signal: (a) time series $x(t)$ generated by the Rössler system in a chaotic regime; (b) the corresponding wavelet spectrum $|W(t, f_s)|$; (*c*, *d*) comparison of the segments of the time series $x(t)$ corresponding to the maximum and minimum of the wavelet spectrum (indicated by arrows in (b)). Symbol ψ in (a) and the dashed curves in (c, d) indicates a segment used for constructing the base wavelet function. In (c, d), the first row of values on the abscissa axis refers to the base function (dashed curves) and the second row, to the compared segment (solid curve) of the initial time series.

and p are the wavelet parameters. As can be seen from formula (2), the wavelet parameter t_0 characterizes the segment of series $x(t)$ which most significantly influences the wavelet spectrum $W(t, s)$. Note that the base wavelet function of type (2) for $x(t) = \sin\omega_\tau t$ with $n = 1.0$ and $p = 2.0$ is an analog of the widely used Morlet wavelet [5, 8] that meets all requirements to the wavelet functions. For a base wavelet function determined in the form (2), the quantity $f_s = 1/s$ has a meaning analogous to the frequency of the Fourier transform [7, 8].

Using a wavelet transform with the base function of type (2), it is possible to effectively separate segments with the length $\Delta t \approx 4n\tau$ from the time series $x(t)$, which are "like" the segment where $t \in (t_0 - 2n\tau, t_0 + 2n\tau)$. Note that the amplitude of $\psi(t)$ decreases by a factor of $\exp(2^{(p-1)})$ within the time interval $|t - t_0| = 2n\tau$, which implies that the wavelet function is based on a segment of the time series with the middle at $t = t_0$ and a length of $4n\tau$.

To illustrate the above procedure, let us consider the results of the wavelet analysis of a signal generated by the Rössler system [1]

$$\dot{x} = -(y + z), \quad \dot{y} = x + ey, \quad \dot{z} = \omega - mz + xz, \quad (3)$$

which represents a standard nonlinear flow system featuring chaotic dynamics. Below, we consider a system of type (3) with the control parameters $e = w = 0.2$ and $m = 5.8$, which corresponds to the case of ribbon chaos.

Figure 1a shows the time series $x(t)$, while Fig. 1b presents the results of calculation of the wavelet spectrum $|W(t, f_s)|$ for a wavelet function constructed using the segment of $x(t)$ corresponding to $t_0 = 164.5$ ($n = 1.0$, $p = 8.0$) (in Fig. 1a, this segment is indicated by vertical dashed lines). The spectrum in Fig. 1b is plotted as the frequencies f_s (corresponding to the scales s of the wavelet transform) versus time t. The shape of this spectrum indicates that the time scale $s = \tau$ is always present, but the intensity varies with the time t.

The maxima of the wavelet spectrum $|W(t, s \approx \tau)|$ taking place at the moments $t = \hat{t}$ correspond to the regions of the time series that are close to the segment used for constructing the base wavelet function ψ (2). This implies that the integral $\int_{t-2n\tau}^{t+2n\tau}[x(t + t') - x(t_0 + t')]^2 dt'$ exhibits minima at $t \sim \hat{t}$, as illustrated in Fig. 1c showing the segments of time series corresponding to the time $t = 210$ (indicated by arrow "c" in Fig. 1b), at which the wavelet surface exhibits a maximum. For the comparison, Fig. 1d shows the segments of time series corresponding to the time $t = 133$ (indicated by the arrow "d" in Fig. 1b), at which the wavelet spectrum $|W(t, s \approx \tau)|$ exhibits a maximum. Dashed curves in Figs. 1c and 1d show the initial segments of the time series used for the formation of the base wavelet function ψ. A comparison of Figs. 1c and 1d shows that the segments of the time series virtually coincide in the former case and exhibit significant distinctions in the latter case.

Real signals are usually distorted by noise and an important problem consists in finding a means of effectively separating the useful signal $x(t)$ from the initial noisy time series. Let us consider a time series $y(t)$ comprising a superposition of the deterministic signal $x(t)$ and a noise component:

$$y(t) = x(t) + D\xi(t), \quad (4)$$

where $\xi(t)$ is a random function modeling the Gaussian white noise.

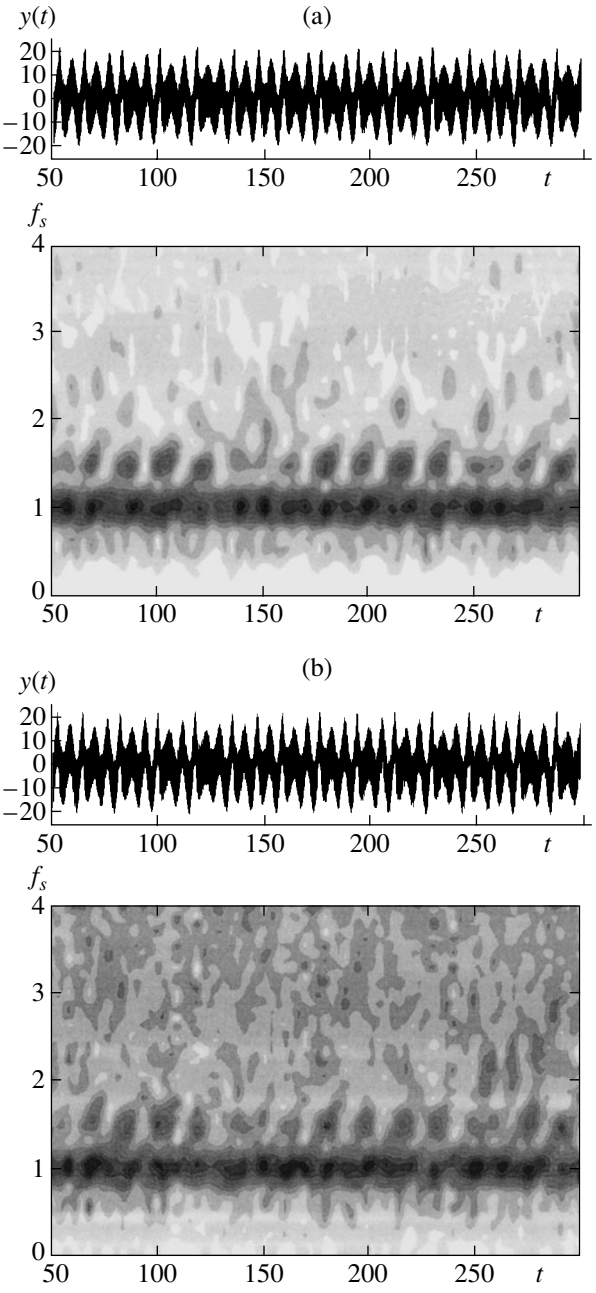

Fig. 2. Wavelet analysis of noisy signals: time series $y(t)$ and the corresponding wavelet spectra for different relative noise intensities $\chi = 1.0$ (a) and 0.5 (b). The base wavelet function was constructed using the same segment of the time series as in Fig. 1.

As above, we assume that the deterministic signal $x(t)$ is generated by the Rössler system (3) with the same control parameters. Consider the wavelet spectra of the signal $y(t)$ (4) obtained for various noise amplitudes D (i.e., various signal to noise ratios $\chi = |x_{max}|/D$, where $|x_{max}|$ is the maximum value of variable $x(t)$).

An analysis of the wavelet spectra constructed for the time series (4) with different noise amplitudes showed that effective separation of the characteristic features of the deterministic signal $x(t)$ by means of the wavelet transform is possible for the signal to noise ratio $\chi > 0.2$–0.3. This is illustrated by Fig. 2 showing the time series $y(t)$ of type (4) and the corresponding wavelet spectra $|W(t, f_s)|$ constructed for two values of the signal to noise ratio, $\chi = 1.0$ (Fig. 2a) and 0.5 (Fig. 2b). For the convenience of comparison of the results of separating the useful signal $x(t)$ from the noise, the time series and wavelet spectra in Fig. 2 are constructed for the same time intervals as in Fig. 1. The base wavelet function (2) was constructed using a segment of the noisy time series with $t_0 = 164.5$ for $n = 1.0$ and $p = 8.0$ (cf. Fig. 1a).

As can be seen from Fig. 2 (with reference to Fig. 1 constructed in the absence of noise), the wavelet transform with a base function (2) representing a segment of the analyzed noisy time series (as well as in the case of the signal free of a noise component) allows us to separate and analyze the characteristic features of the useful signal. For a relatively small noise intensity (Fig. 2a, $\chi = 1.0$), the form of the resulting wavelet surface only slightly differs from the corresponding spectrum of the signal without noise (Fig. 1b). As the noise intensity increases (Fig. 2b, $\chi = 0.5$), the form of the wavelet surface is distorted and the maxima are less pronounced. The wavelet spectrum in Fig. 2b is especially strongly impaired (in comparison to Fig. 1b) in the region of scales $f_s > 2.0$. At the same time, the structure of the wavelet surface $|W(t, f_s)|$ in the region of $s \sim 1.0$ is close to that of the spectrum obtained for the signal without noise, which provides for a correct analysis. As the noise intensity grows further, the wavelet surface structure is broken even in the region of the time scales $s \sim 1.0$, which hinders separation and analysis of the initial signal $x(t)$ in the presence of noise.

Thus, we have demonstrated the possibility of effective analysis of a time series (including noisy signals) by means of wavelet analysis using basis functions representing segments of the analyzed time series.

Acknowledgments. This study was supported by the Russian Foundation for Basic Research, project nos. 02-02-16351 and 01-02-17392.

REFERENCES

1. S. P. Kuznetsov, *Dynamical Chaos* (Fizmatlit, Moscow, 2001).
2. V. S. Anishchenko, T. E. Vadivasova, and V. V. Astakhov, *Nonlinear Dynamics of Chaotic and Stochastic Systems* (Saratov. Gos. Univ., Saratov, 1999).
3. N. V. Karlov and N. A. Kirichenko, *Oscillations, Waves, and Structures* (Fizmatlit, Moscow, 2001).
4. D. I. Trubetskov and A. E. Khramov, *Lectures on Microwave Electronics for Physicists* (Fizmatlit, Moscow, 2003), Vol. 1.

5. N. M. Astaf'eva, Usp. Fiz. Nauk **166**, 1145 (1996) [Phys. Usp. **39**, 1085 (1996)].
6. I. Daubechies, *Ten Lectures on Wavelets* (SIAM, Philadelphia, 1992; NITs "Regul. Khaot. Din.", Izhevsk, 2001).
7. A. A. Koronovskiĭ and A. E. Khramov, *Continuous Wavelet Analysis and Its Applications* (Fizmatlit, Moscow, 2003).
8. A. A. Koronovskiĭ and A. E. Khramov, *Continuous Wavelet Analysis: Application to Nonlinear Dynamics Problems* (Gos. UNTs "Kolledzh", Saratov, 2002).
9. V. G. Anfinogentov, A. A. Koronovskiĭ, and A. E. Khramov, Izv. Ross. Akad. Nauk, Ser. Fiz. **64**, 2383 (2000).
10. *Wavelets in Medicine and Biology*, Ed. by A. Aldroubi and M. Unser (CRC Press, Boca Raton, 1994).
11. M. Unser and A. Aldroubi, Proc. IEEE **84**, 626 (1996).
12. C. Torrence and G. P. Compo, Bull. Am. Meteorol. Soc. **79**, 61 (1998).
13. B. Ph. Van Milligen, E. Sánchez, T. Estrada, *et al.*, Phys. Plasmas **2**, 3017 (1995).
14. A. A. Koronovskiĭ and A. E. Khramov, Fiz. Plazmy **28**, 722 (2002) [Plasma Phys. Rep. **28**, 666 (2002)].
15. F. Argoul, A. Arneodo, G. Grasseau, *et al.*, Nature **338**, 51 (1989).
16. M. Farge, Annu. Rev. Fluid Mech. **24**, 395 (1992).
17. A. A. Koronovskiĭ and A. E. Khramov, Pis'ma Zh. Tekh. Fiz. **27** (1), 3 (2001) [Tech. Phys. Lett. **27**, 1 (2001)].
18. P. Frick, S. L. Baliunas, D. Galyagin, and D. W. Sokoloff, Astrophys. J. **483**, 426 (1997).

Translated by P. Pozdeev

Technical Physics Letters, Vol. 29, No. 9, 2003, pp. 779–780. Translated from Pis'ma v Zhurnal Tekhnicheskoĭ Fiziki, Vol. 29, No. 18, 2003, pp. 70–74.

Measuring Local Thermal Fluxes during Thermal Exchange between a Surface and a Vortex Structure

V. P. Samsonov

Surgut State University, Surgut, Russia

e-mail: svp@iff.surgu.ru

Received April 2, 2003

Abstract—The effect of a vortex structure in a "dumped" flame on the intensity of heat exchange between this flame and a flat surface has been studied. An optical polarization technique is proposed for the visualization and measurement of an inhomogeneous temperature field at the surface and inside the heat exchanger wall. It is shown that the gas circulation in large vortex cells leads to an increase in the local thermal fluxes. In the range of Reynolds numbers $50 < \mathrm{Re} < 400$, a thermal flux from the "dumped" flame to a flat heat exchanger surface is 20–30% greater than that for an oncoming laminar flame. *© 2003 MAIK "Nauka/Interperiodica".*

Measuring the heat transfer coefficient on the surface of a body involved in the heat exchange with an inhomogeneous and nonisothermal flux presents a complicated problem, especially in the presence of large temperature gradients in lateral directions. Traditional optical methods used for the visualization of thermal inhomogeneities have a common disadvantage of providing only integral characteristics of these inhomogeneities [1]. For example, the order of interference lines on the image of a thermal inhomogeneity is determined by the phase difference between interfering light waves

$$\Delta\varphi = \left[2\pi\int_0^l (n_0 - n)dx\right]/\lambda,$$

where λ is the light wavelength; n_0 and n are the refractive indices of the medium in the thermal inhomogeneity and in the surrounding medium, respectively; and l is the geometric pathlength of a light ray. A solution of this integral equation cannot be found for an optical inhomogeneity of arbitrary shape. In some cases, a body on the surface of which the heat exchange has to be studied can be modeled by a stack of thin transparent plates. The phase shift of the light wave in each plate is determined by the simple relation $\Delta\varphi = 2\pi\Delta x(n_0 - n_i)/\lambda$, where n_i is the refractive index of the ith plate, Δx is the plate thickness, and λ is the light wavelength.

In order to establish the mechanism of the influence of a vortex structure in a "dumped" flame on the intensity of heat exchange between the flame and a flat heat exchanger surface, we have visualized the temperature field in the heat exchanger wall using a special optical polarization technique. The "dumped" flame was formed during combustion of a gas supplied via a vertical burner nozzle turned upside down. The vector of the gas flow velocity on the nozzle axis coincided with the direction of the force of gravity.

The main element of the experimental setup schematically depicted in Fig. 1 is the heat exchanger representing a stack of rectangular Plexiglas plates tightly pressed to each other so as to form a rectangular parallelepiped. Plexiglas was selected due to the ability of this material to polarize the incident light. The stack was rendered transparent by polishing the side faces of the plates. A vertical channel with a diameter of 0.001 m drilled in the stack was used to supply a combustible gas to the bottom horizontal surface of the stack. The channel axis was lying in the interface of two plates.

At a certain flow rate of the gas, a vortex structure is formed in the flame at the heat exchanger surface [2]. By placing the heat exchanger between polarizer and analyzer of a polariscope-polarimeter PKS-125, it was possible to obtain an image of the interference pattern formed in the temperature field in the heat exchanger body. The image is formed as a result of interference of the ordinary and extraordinary light rays. The difference between refractive indices for the ordinary and extraordinary rays is given by the relation $n_o - n_e = c\sigma$, where c is the optico-mechanical coefficient and σ is the internal stress.

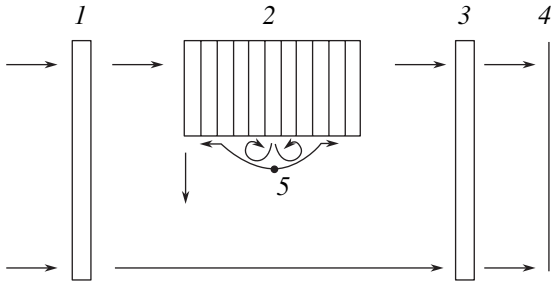

Fig. 1. Schematic diagram illustrating visualization of the "dumped" flame and the temperature field in a heat exchanger wall: (*1*) polarizer; (*2*) heat exchanger representing a stack of plates; (*3*) analyzer; (*4*) screen; (*5*) "dumped" flame.

1063-7850/03/2909-0779$24.00 © 2003 MAIK "Nauka/Interperiodica"

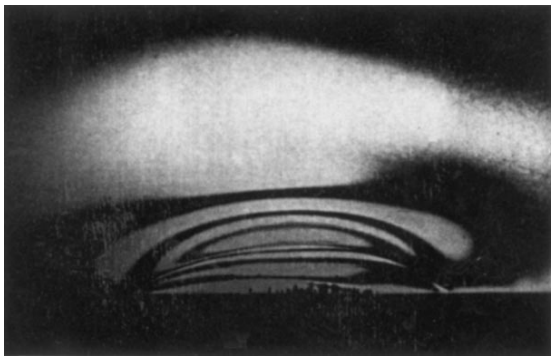

Fig. 2. Interference pattern of a thermal inhomogeneity in the heat exchanger wall.

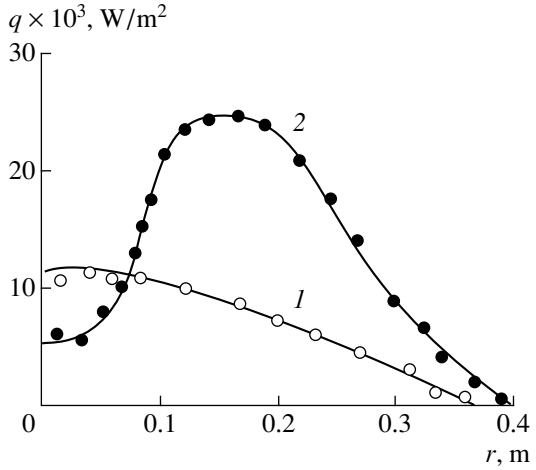

Fig. 3. Radial distributions of the thermal fluxes on the heat exchanger surface for a (*1*) "dumped" flame and (*2*) laminar flame.

The internal stress component σ in the direction of propagation of the light wave is $\sigma = -\alpha TE$, where α is the thermal expansion coefficient, T is the absolute temperature, and E is the Young modulus. By transmitting light separately through each plate in the stack, it is possible to obtain interference images of the temperature field in the flat zones, with the phase difference of the light waves being $\Delta\varphi = 2\pi\Delta x(-c\alpha TE)/\lambda$. Using the wall temperature measured preliminarily at a certain point and the interference order at this point, it is possible to calculate the temperature at any other point inside the heat exchanger wall.

After heating the bottom surface of the heat exchanger, the stack can be disassembled and the interference pattern formed in the temperature field can be observed separately in an arbitrary plane of the heat exchanger wall. The time required for disassembly of the stack in our experiments was 1–2 s. Evidently, the relative error of the temperature determination using the order of the interference band observed for the plate transilluminated in the normal direction is related to a change in the shape of the thermal inhomogeneity. In the order of magnitude, the error is determined by the ratio of the plate thickness to the thermal inhomogeneity radius. Under the conditions of our experiments, the thermal inhomogeneity diameter varied from 0.015 to 0.070 m at a plate thickness of 0.002 m. The interference lines could be considered as isotherms with an error ranging from 2.5 to 13%.

Figure 2 presents the typical interference pattern observed for a thermal inhomogeneity in a heat exchanger wall, which corresponds to a plate occurring at a radial distance of 0.018 m from the channel (the radius of thermal inhomogeneity on the heat exchanger surface is 0.036 m). The upper edge of a dark horizontal band observed in the bottom part of the photograph, on which the interference lines terminate, corresponds to the position of a boundary on the heat exchanger surface heated from below. The photograph in Fig. 2 illustrates the penetration of the thermal wave into the heat exchanger wall. The velocity of propagation of a thermal wave is proportional to the thermal flux through the surface, the latter being dependent on the surface temperature.

The temperature at any point inside the heat exchanger body can be determined using the order of interference of the light waves, which is calculated using the number of the interference band counted from the top or bottom edge of the image of the thermal inhomogeneity. For the known image scale and the coefficient of thermal conductivity χ of the wall material, the thermal flux through the heat exchanger surface was calculated as $q = \chi\Delta T/\Delta y$, where ΔT is the temperature difference (calculated using the numbers of adjacent interference bands) and Δy is the spacing between adjacent interference bands in the direction perpendicular to the heat exchanger surface.

Figure 3 shows the results of calculations of the radial distribution of thermal fluxes on a horizontal heat exchanger surface slowly heated by a "dumped" vortex flame and by a laminar flame for the same nozzle diameters (0.001 m) and equal gas flow rates (1.5×10^{-3} m^3). The combustible gas was propane. The gas burner channel forming a laminar flame was vertical; the nozzle edge was spaced by 0.002 m from the heat exchanger surface. The maximum of $q(r)$ (Fig. 3, curve *2*) for the "dumped" vortex flame takes place in the vortex region, where the vector of the combustion product velocity is directed toward the heat exchanger surface. A comparison of curves *1* and *2* shows that an increase in the thermal flux in the "dumped" flame is related to the convective heat transfer during circulation of the combustion products in the vortex structure.

REFERENCES

1. W. Höuf and U. Grigull, *Optical Methods in Heat Transfer*, in *Advances in Heat Transfer* (Academic Press, New York, 1970; Mir, Moscow, 1973).
2. M. V. Alekseev, V. P. Samsonov, and I. G. Fateev, Fiz. Goreniya Vzryva **25** (6), 47 (1989).

Translated by P. Pozdeev

Technical Physics Letters, Vol. 29, No. 9, 2003, pp. 781–783. Translated from Pis'ma v Zhurnal Tekhnicheskoĭ Fiziki, Vol. 29, No. 18, 2003, pp. 75–80.

Hybridization of Acoustic Waves in Piezoelectric Plates

I. A. Borodina, B. D. Zaĭtsev*, I. E. Kuznetsova, A. A. Teplykh, and V. V. Shurygin

Saratov Branch, Institute of Radio Engineering and Electronics, Russian Academy of Sciences, Saratov, Russia

**e-mail: zaitsev@ire.san.ru*

Received April 3, 2003

Abstract—The conditions for hybridization of the zero-order and high-order acoustic waves propagating in a piezoelectric crystal plate have been studied. The dependence of the phase velocity of the hybrid waves on the parameter *hf* (*h* is the plate thickness and *f* is the wave frequency) is established for the potassium niobate and lithium niobate plates possessing various crystallographic orientations and conductivities. It is found that hybridization takes place when the conductivity of a thin surface layer exceeds a certain critical value, which can vary within broad limits depending on the plate material and orientation. The degree of dispersive repulsion of the coupled modes grows with increasing electromechanical coupling coefficient. © *2003 MAIK "Nauka/Interperiodica".*

Under certain conditions, waves of different types propagating in a multimode waveguide system exhibit coupling and cannot exist independently of one another. Such coupled waves are referred to as hybrid modes. The phenomenon of hybridization is well known in dielectric electromagnetic waveguides [1], magnetic materials [2], and some other systems. In recent years, it was reported that hybrid modes can also exist in strongly piezoelectric crystals.

In particular, it was theoretically predicted that coupled surface waves of the Rayleigh and Gulyaev–Bleustein types can propagate along the *Z* axis of a metal-coated ($Y + 66°$)-cut semi-infinite crystal of lithium niobate [3]. Our theoretical results [4] showed that a *Y*-cut plate of potassium niobate with one electrically shorted surface can exhibit a weak coupling between an antisymmetric A_0 wave and an SH_0 wave with transverse horizontal polarization propagating in the $X + 15°$ direction. These waves form a hybrid mode provided that the parameter *hf* (*h* is the plate thickness and *f* is the wave frequency) is close to 1000 m/s. No hybridization takes place when both surfaces of the plate are electrically open. However, our knowledge about the conditions of hybridization of acoustic waves in piezoelectric crystals is by no means exhaustive, and this phenomenon requires further thorough investigation.

This paper continues theoretical investigations of the coupled zero-order acoustic waves of the A_0–SH_0 type propagating along the $X + 15°$ direction in *Y*-cut potassium niobate crystals. We have attempted to find new hybrid couples among the acoustic modes of both zero and higher orders in a lithium niobate plate. Thorough analysis revealed the existence of another hybrid couple, formed by a symmetric first-order Lamb wave S_1 and a second-order wave with transverse horizontal polarization SH_2, propagating in an *Y*–*X* plate of lithium niobate. In addition, we have theoretically studied the influence of a thin (as compared to the wavelength) conducting layer on the characteristics of the aforementioned hybrid modes in piezoelectric plates of potassium niobate and lithium niobate.

In order to find new hybrid couples, we have solved the problem of acoustic wave propagation in a piezoelectric plate of thickness *h* occurring in vacuum, with (i) both surfaces electrically open or (ii) one surface electrically shorted. The numerical solution of a system of the equations of motion, Laplace equation, and material equations for a piezoelectric medium in combination with standard boundary conditions was described in detail elsewhere [5]. The analysis yielded the dependences of the wave phase velocity on the parameter *hf* for the aforementioned materials in various crystallographic situations. From these data, we determined the regions of parameters and the modes for which hybridization is possible.

Then we studied the influence of a thin conducting film on the characteristics of hybrid couples. It was assumed that the conducting layer thickness is small as compared to the wavelength λ, so that the mechanical load upon the plate could be ignored. The method of solving such problems, whereby the presence of a conducting layer is taken into account only in the electrical boundary conditions, was described previously [6].

Figure 1 shows plots of the phase velocities of the A_0 and SH_0 waves propagating in the $X + 15°$ direction versus parameter *hf* for the *Y*-cut potassium niobate plates with various values of the surface conductivity. Figure 2 presents analogous curves for the S_1–SH_2 hybrid couple

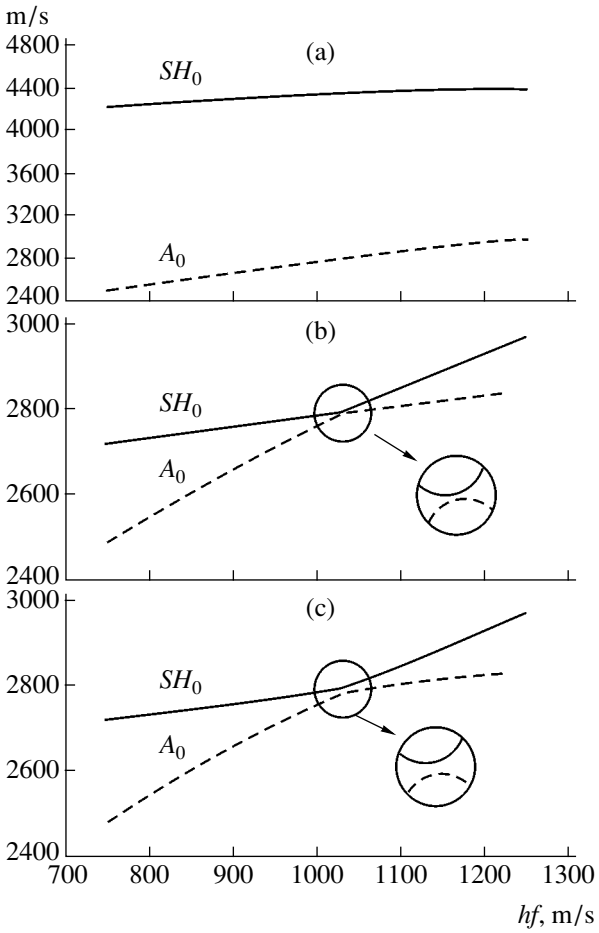

Fig. 1. Plots of the phase velocities of the A_0 and SH_0 waves propagating in the $X + 15°$ direction versus parameter *hf* for the *Y*-cut potassium niobate plates with various values of conductivity of a thin surface film: (a) $\sigma = 10^{-8}$ S; (b) $\sigma = \sigma_{cr} = 4 \times 10^{-4}$ S; (c) $\sigma = 10^{-2}$ S.

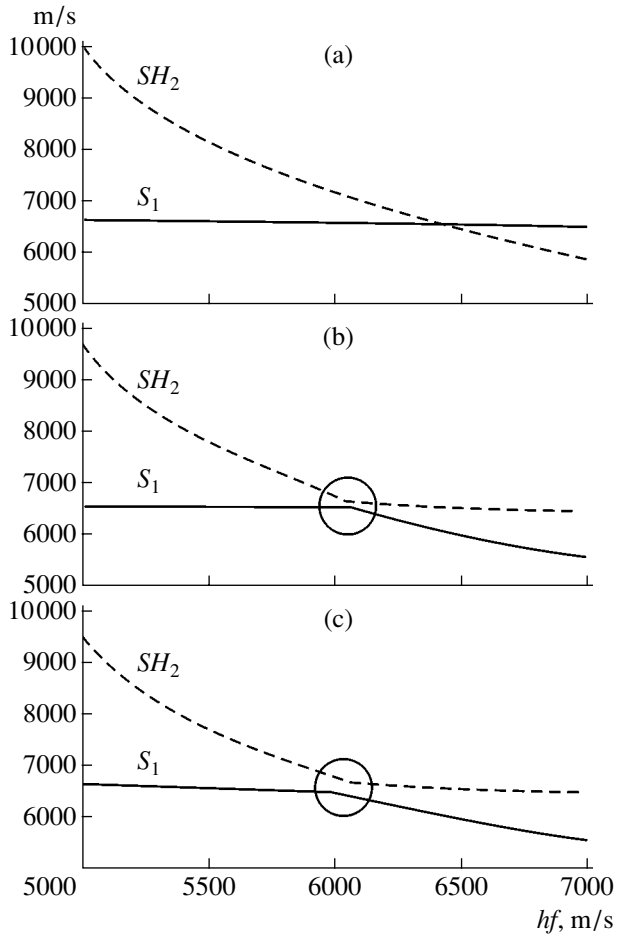

Fig. 2. Plots of the phase velocities of the S_1 and SH_2 waves propagating in the *X* axis direction versus parameter *hf* for the *Y*-cut lithium niobate plates with various values of conductivity of a thin surface film: (a) $\sigma = 10^{-8}$ S; (b) $\sigma = \sigma_{cr} = 6 \times 10^{-6}$ S; (c) $\sigma = 10^{-2}$ S.

propagating along the *X* axis in the *Y*-cut plates of lithium niobate. These results allow us to conclude that hybridization arises when the surface conductivity σ exceeds a certain critical value σ_{cr}, which can vary within broad limits depending on the plate material and orientation. For example, $\sigma_{cr} = 4 \times 10^{-4}$ S for the aforementioned zero-order A_0–SH_0 hybrid couple in a potassium niobate plate with $hf \approx 1040$ m/s (Fig. 1b) and $\sigma_{cr} = 6 \times 10^{-6}$ S for the S_1–SH_2 hybrid couple in a lithium niobate plate with $hf \approx 6050$ m/s (Fig. 2b). The modes under consideration are not coupled in the same plates with electrically free surfaces and with $\sigma < \sigma_{cr}$, whereby the dispersion curves exhibit no characteristic splitting (Figs. 1a and 2a). For $\sigma = \sigma_{cr}$, the dispersion curves exhibit "repulsion," the extent of which increases with σ and tends to maximum as $\sigma \longrightarrow \infty$ (Fig. 1c).

As can be seen from Figs. 1c and 2c, the dispersion curves of the piezoelectrically more active S_1–SH_2 couple propagating in the *Y*–*X* lithium niobate exhibit more pronounced repulsion as compared to that for the piezoelectrically less active A_0–SH_0 couple propagating in the Y–$(X + 15°)$ potassium niobate. Based on this fact, we conclude that the degree of repulsion between the dispersion curves of coupled modes grows with increasing electromechanical coupling coefficient of the waves under consideration.

Thus, the results of our investigation showed that piezoelectric plates of a certain crystallographic orientation covered with a thin conducting surface film can feature hybrid modes of the zero and higher orders, provided that the film conductivity exceeds a definite critical value. These results are not only of interest from the fundamental standpoint but can find practical application in the research and development of various devices such as amplitude and phase modulators and controlled directional couplers. These devices employ piezoelectric plates coated with thin conducting films,

the conductivity of which can be controlled by various external factors such as the electric or magnetic field, light, etc.

Acknowledgments. This study was supported by the Russian Foundation for Basic Research (project no. 01-02-16266a) and by a grant from NSF.

REFERENCES

1. *Integrated Optics*, Ed. by T. Tamir (Springer-Verlag, Berlin, 1975; Mir, Moscow, 1978).
2. J. W. Tucker and V. W. Rampton, *Microwave Ultrasonics in Solid State Physics* (North-Holland, Amsterdam, 1972; Mir, Moscow, 1975).
3. V. G. Mozhaev and M. Weihnact, Proc. IEEE Ultrason. Symp. 73 (1999).
4. B. D. Zaitsev and I. E. Kuznetsova, J. Appl. Phys. **90**, 3648 (2001).
5. B. D. Zaitsev, S. G. Joshi, and I. E. Kuznetsova, IEEE Trans. Ultrason. Ferroelectr. Freq. Control **48**, 624 (2001).
6. Yu. V. Gulyaev, I. E. Kuznetsova, B. D. Zaĭtsev, *et al.*, Pis'ma Zh. Tekh. Fiz. **25** (8), 21 (1999) [Tech. Phys. Lett. **25**, 302 (1999)].

Translated by P. Pozdeev

Technical Physics Letters, Vol. 29, No. 9, 2003, pp. 784–786. Translated from Pis'ma v Zhurnal Tekhnicheskoĭ Fiziki, Vol. 29, No. 18, 2003, pp. 81–87.

On the Velocity of Propagation of a Frequency-Modulated Signal in a Strongly Dispersive Medium

N. S. Bukhman

Samara State Academy of Building and Architecture, Samara, Russia

e-mail: buhman@ssaba.smr.ru

Received March 31, 2003

Abstract—The velocity of propagation of a narrowband, frequency-modulated signal in a medium characterized by a strong dispersion of absorption or amplification may significantly differ from the group velocity, with which an analogous narrowband signal without frequency modulation propagates in the same medium. In particular, the velocity of the frequency-modulated signal can be supraluminal or negative, even when the group velocity is subluminal. *© 2003 MAIK "Nauka/Interperiodica".*

1. In recent years, much interest has been devoted to the velocity of propagation of wave packets in a strongly dispersive media (see, e.g., [1–3] and references therein). This interest is related primarily to effects such as the motion of the wave packet maximum with a supraluminal or negative group velocity and to the possibility of "self-regeneration" of a partly transmitted signal. The group velocity of a signal is usually identified with the velocity of propagation of the signal maximum.

As will be demonstrated below, this approach to the group velocity definition is generally inapplicable to frequency-modulated (FM) signals propagating in a strongly dispersive medium: FM signals can propagate with velocities significantly different (toward both increase and decrease) from the group velocity in such a medium. As a result, the aforementioned effects in a strongly dispersive medium can take place in the case of both anomalous (positive) and normal (negative) dispersion. Moreover, the velocity of propagation of an FM signal (and the above effects) can be controlled by changing the character of the frequency modulation.

This is related to the fact that a strong dispersion of the real refractive index of a given medium is accompanied (according to the Kramers–Kronig relations [4]) by a strong dispersion of the absorption (or amplification) coefficient of this medium. Therefore, a strongly dispersive medium is, strictly speaking, always selectively (with respect to frequency) absorbing or amplifying and, hence, a description of the propagation of a wave packet in such a medium has to take into account both dispersion of the real refractive index and the dispersion of the absorption (or amplification) coefficient. This is most readily achieved in terms of the complex group velocity [2, 3, 5] or using an equivalent concept of the complex signal delay time.

2. Consider a narrowband signal $E(z, t)$ with a carrier frequency ω_1 and a complex envelope $A(z, t)$ propagating along the z axis in a homogeneous isotropic medium:

$$E(z, t) = A(z, t)\exp(-i\omega_1 t) + A^*(z, t)\exp(i\omega_1 t). \quad (1)$$

Let the wave packet propagate in a medium with the refractive index $n(w) = n_0 + \Delta n(\omega)$, where $\Delta n(\omega)$ is a complex additive related to the spectral amplification band centered at ω_0 and n_0 is the background (nonresonance) value of the refractive index weakly dependent on the light frequency in the region of ω_0.

Let us introduce the following notation: $\alpha_0 \equiv i(\omega_0/c)\Delta n(\omega_0)$ is the amplitude amplification coefficient at the center ω_0 of the selective amplification band; $g(\Omega) \equiv ik\alpha_0^{-1}\Delta n(\omega_0 + \Omega)$ is the complex form factor of the line normalized to unity at the at the center ω_0 of the spectral amplification band; Ω is the detuning of a wave frequency from the central frequency of the spectral amplification band ($\omega \equiv \omega_0 + \Omega$); $\xi \equiv \alpha_0 z$ is the optical pathlength in the layer of a substance with a thickness of z; $\Omega_0 = \omega_1 - \omega_0$ is the frequency shift of the carrier frequency ω_1 relative to the center ω_0 of the spectral amplification band.

Recently [2, 3], the following expression was obtained in the complex group velocity approximation for the complex envelope $A(z, t)$ of a wave packet of arbitrary shape transmitted via a layer of dispersive medium:

$$A(z, t) = \exp(ik_0 n(\omega_0)z + \xi g(\Omega_0))A^{(0)}(t - \tau(z)), \quad (2)$$

where Z is the layer thickness, $A^{(0)}(t) \equiv A(0, t)$ is the time dependence of the signal at the boundary of the

layer (i.e., at $z = 0$), and $\tau(z)$ is the complex signal delay time. The latter quantity is determined by the relations

$$\tau(z) \equiv \tau_0 + \tau_r + i\tau_i \equiv z/v_{gr}^{compl}, \quad \tau_0 \equiv z/v_{ph}, \quad v_{ph} \equiv c/n_0,$$
$$\tau_r \equiv \xi\frac{\partial(\mathrm{Im}g(\Omega_0))}{\partial\Omega_0}, \quad \tau_i \equiv -\xi\frac{\partial(\mathrm{Re}g(\Omega_0))}{\partial\Omega_0}. \tag{3}$$

Here, the parameter τ_0 has the meaning of the signal delay time in vacuum and is always positive. The parameter τ_r represents an additional (with respect to vacuum) real signal delay time and can be either positive or negative (negative vales of this parameter are usually related to the possibility of supraluminal or negative group velocity of the wave packet). The parameter τ_i has the meaning of the imaginary part of the complex signal delay time. In the case of amplitude-modulated signals, this parameter describes a signal distortion caused by the dispersion of the absorption (or amplification) coefficient of the medium.

For an FM signal, the imaginary part of the signal delay time may lead to a shift of the time dependence of the signal intensity, that is, to a change in the velocity of motion of the signal maximum. This can be illustrated for a Gaussian signal with a linear frequency modulation (LFM):

$$A^{(0)}(t) = \exp\left(-\frac{t^2}{T^2}(1 - i\pi m/2)\right), \tag{4}$$

where T is the signal duration and m is the LFM index.[1] The Gaussian time dependence of this signal (see Fig. 1a) is independent of the LFM index.

As can be readily checked, the application of formula (2) in the complex group velocity approximation leads to the following expression for the time variation of the signal intensity $I(z, t) = |A(z, t)|^2$ upon traveling a distance z in the dispersive medium:

$$I(z, t) = \exp\left(2\xi\mathrm{Re}g(\Omega_0) + \frac{2\tau_i^2(1 + (\pi m/2)^2)}{T^2} + \frac{2(t - t_c)^2}{T^2}\right), \tag{5}$$

where

$$t_c(z) = \tau_0(z) + \tau_r(z) + (\pi m/2)\tau_i(z) \tag{6}$$

for the central point of the signal.

As can be seen, the LFM Gaussian signal (as well as a signal without FM) propagates, in the complex group velocity approximation, without changes in the shape or duration.[2] The presence of FM ($m \neq 0$) leads to an additional (as compared to the case of an unmodulated signal, $m = 0$) increase in the signal amplitude and a change in the velocity of propagation of the signal maximum. The velocity of propagation of the LFM Gaussian signal can be either higher or lower (depending on the sign of the modulation index) than the velocity of a Gaussian signal without FM (i.e., than the "true" group velocity).

The factors accounting for this result are quite evident. The greater amplitude of the LFM signal as compared to that of the signal without such modulation is related to the fact that an increase in the modulation index leads to expansion of the frequency spectrum and to an increase in the integral (over the entire spectrum) amplification coefficient (as compared to that at the middle frequency of the signal spectrum).

The difference between the velocity of propagation of an LFM signal from that of an unmodulated signal is related to the fact that the signal components with the frequencies closer to the central frequency of the spectral amplification band exhibit a stronger amplification in the course of propagation. In other words, the difference of the velocity of propagation of an FM signal from the group velocity of a signal without FM in this case is caused by the predominant amplification of the leading and trailing parts of the packet, which is related to the difference of the carrier frequencies in these parts. This mechanism is close to a nonlinear mechanism responsible for the supraluminal group velocity, related to the predominant amplification of the signal front in a medium with nonlinear saturation of the amplification coefficient [7, 8].

3. The above results can be illustrated by calculations. Let us restrict the consideration (as in [2, 3]) to the case of a Lorentzian profile of the spectral amplification band with the width $\Delta\Omega_{1/2}$ and the coherence time $\tau_l \equiv 2/\Delta\Omega_{1/2}$:

$$g(\Omega) = (1 - i2\Omega/\Delta\Omega_{1/2})^{-1}. \tag{7}$$

The signal parameters are as follows: duration, $T = 10\tau_l$; carrier frequency shift relative to the center of the spectral amplification band $x_0 = \Omega_0\tau_l = 1$ modulation index $m = 0, \pm 5$. The results of calculations of the signal shape in different approximations are presented in Fig. 1, which shows the time variation of the signal intensity $I(z, t) \equiv |A(z, t)|^2$ for various pathlengths (and, accordingly, for various values of the complex signal delay time $\tau_{compl} = \tau_r + i\tau_i$): $\xi = 0$ ($\tau_{compl} = 0$, Fig. 1a); $\xi = 1.5$ ($\tau_{compl} = 0.75i\tau_l$, Fig. 1b); $\xi = 3$ ($\tau_{compl} = 1.5i\tau_l$, Fig. 1c). The results of numerical calculations are

[1] A frequency modulation of this type is acquired by a Gaussian wave packet, initially possessing no modulation, in the course of propagation in a nonabsorbing weakly-dispersive medium (see [6]).

[2] A non-Gaussian signal, either with or without FM, propagating at a complex group velocity, naturally exhibits a distortion. In this sense, the presence or absence of the FM is insignificant.

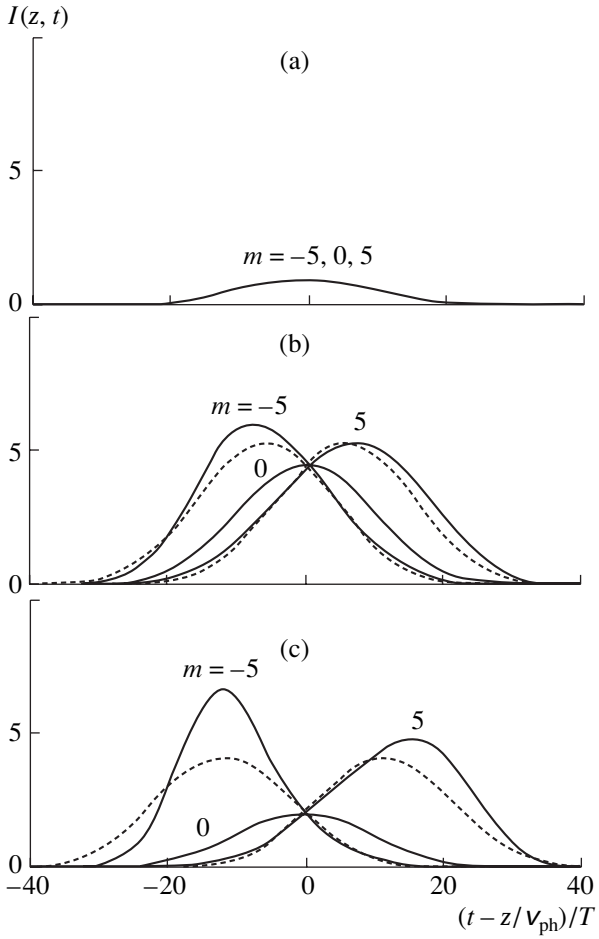

Fig. 1. Propagation of a frequency-modulated Gaussian signal in a dispersive medium for various values of the modulation index (m = –5, 0, +5) and the optical pathlength ξ = 0 (a), 1.5 (b), and 3 (c).

depicted by solid curves and the results obtained within the framework of the complex group velocity approximation (analytical formulas (2) and (3)) are presented by the dashed curves. For the selected shift of the carrier frequency, the additional (relative to vacuum) real signal delay time is zero, which implies that the real group velocity coincides with the phase velocity (i.e., with the light velocity in vacuum for $n_0 = 1$). For this reason, the unmodulated signal ($m = 0$) in the comoving frame employed in Fig. 1 occurs "in rest" and only slightly deforms with increasing pathlength ξ. In the case of a positive (or negative) FM, the signal maximum appears significantly earlier (or later) than that of the unmodulated signal.

Thus, the velocity of propagation of the FM signals in a strongly dispersive medium can be controlled by changing the modulation. The resulting velocity can significantly differ (toward both increase and decrease) from the group velocity in the given medium. In particular, the velocity of propagation of an FM signal can be supraluminal or negative, even when the group velocity is subluminal. In this case, the character of the signal propagation is analogous to that of a signal with a supraluminal group velocity, whereby a "nonantropogenic" signal prediction and "self-regeneration" of a partly transmitted signal are possible (see [2, 3]).

REFERENCES

1. A. M. Akul'shin, A. Cimmino, and G. I. Opat, Kvantovaya Élektron. (Moscow) **32**, 567 (2002).
2. N. S. Bukhman, Kvantovaya Élektron. (Moscow) **31**, 774 (2001).
3. N. S. Bukhman, Zh. Tekh. Fiz. **72** (1), 136 (2002) [Tech. Phys. **47**, 132 (2002)].
4. L. D. Landau and E. M. Lifshitz, *Course of Theoretical Physics*, Vol. 8: *Electrodynamics of Continuous Media* (Nauka, Moscow, 1982; Pergamon, New York, 1984).
5. L. A. Vaĭnshteĭn, Usp. Fiz. Nauk **118**, 339 (1976) [Sov. Phys. Usp. **19**, 189 (1976)].
6. M. B. Vinogradova, O. V. Rudenko, and A. P. Sukhorukov, *The Theory of Waves* (Nauka, Moscow, 1979).
7. N. G. Basov, R. V. Ambartsumyan, V. S. Zuev, *et al.*, Dokl. Akad. Nauk SSSR **165**, 58 (1965) [Sov. Phys. Dokl. **10**, 1039 (1965)].
8. P. G. Kryukov and V. S. Letokhov, Usp. Fiz. Nauk **99**, 169 (1969) [Sov. Phys. Usp. **12**, 641 (1969)].

Translated by P. Pozdeev

Technical Physics Letters, Vol. 29, No. 9, 2003, pp. 787–789. Translated from Pis'ma v Zhurnal Tekhnicheskoĭ Fiziki, Vol. 29, No. 18, 2003, pp. 88–94.

The Carbon Web Formation during the Synthesis of Single-Sheet Nanotubes in the Jet of Laser Ablation Products Expanding in Electric Field

G. I. Kozlov

Institute for Problems of Mechanics, Russian Academy of Sciences, Moscow, Russia
e-mail: kozlov@ipmnet.ru

Revised manuscript received May 6, 2003

Abstract—An external electric field was used for the first time as a factor controlling the synthesis of single-sheet carbon nanotubes in the expanding jet of products formed in the course of laser ablation of a carbon target with a catalyst. Application of the electric field leads to a dramatic change in a macroscopic pattern of the process, whereby almost entire reactor volume is filled with a fine carbon web. According to the results of analysis of the web fibers by Raman scattering, the material consists of single-sheet carbon nanotubes with diameters ranging from 1.23 to 1.41 nm. © *2003 MAIK "Nauka/Interperiodica".*

The synthesis of single-sheet carbon nanotubes [1] is performed by various methods, the most promising of which are the electric arc discharge, laser ablation of graphite, and catalytic pyrolysis of hydrocarbons. Extensive information about the results of investigations in this field is summarized in reviews [2, 3]. Despite considerable progress, there are still many problems related to the development of effective methods ensuring self-organized synthesis of single-sheet carbon nanotubes (SCNTs) and other functional molecular nanostructures with preset characteristics and to the elucidation of mechanisms involved in these processes.

In this context, of special interest are the methods of laser ablation [4, 5], which offer a convenient tool for studying the mechanism and kinetics of the entire sequence of processes involved in the SCNT synthesis, including both the initial stage of the evaporation of carbon and catalyst and the subsequent stages of self-organized nucleation and growth of molecular associates, compact clusters, and carbon nanostructures. Naturally, the most interesting problem is to elucidate the mechanisms controlling the nucleation and self-organized growth of SCNTs and to establish factors influencing these processes. We suggest that one such factor is the electric field. It is therefore of interest to determine how the course of the synthesis and the characteristics of carbon nanostructures change when the reaction zone is exposed to a constant electric field.

Here were report for the first time about a strong effect of the applied electric field on the synthesis of single-sheet carbon nanotubes in the expanding jet of products formed in the course of laser ablation of a carbon target with a nickel–yttrium catalyst. The experiments were performed in a modified laser setup described in detail elsewhere [5, 6], which was previously used for the investigations of pyrolysis waves and the laws of SCNT synthesis by laser ablation of graphite with catalyst.

The output radiation of a CW gas-discharge CO_2 laser with a power of 2 kW and a beam divergence of 8×10^{-4} rad, focused by a zinc selenide lens with a focal length of 20 cm, entered via a salt window into a quartz tube reactor with an internal diameter of 7.1 cm and a length of 51 cm. The radiation was concentrated on the edge surface of a cylindrical graphite target with a diameter of 5 mm and a length of 9 mm. The target had a channel with a diameter of 3.8 mm and a length of 7 mm filled with a mixture of carbon and a nickel–yttrium catalyst (C : Ni : Y = 95 : 4 : 1 at. %). The laser spot diameter on the target surface was 2 mm. The reactor was purged with helium (relaxant of the variational energy of the synthesized nanostructures) at a flow rate of 0.5 l/min and a pressure of 760 Torr.

The laser action induced intensive vaporization of the target with the formation of a jet of the laser ablation products expanding in the direction opposite to the incident the laser beam and the helium flow. A special diaphragm situated at a distance of 6 cm from the target deflected the jet of ablation products and directed it along the wall toward the reactor output. The nanoparticles formed in the course of condensation in the cold peripheral regions of the reactor were deposited on special substrates, as well as on the diaphragm and the reactor walls. The deposited products were studied by methods of Raman scattering and scanning electron microscopy.

In order to study the influence of an external electric field on the synthesis and to provide for the most favorable conditions of the self-organized synthesis of SCNTs, the process was conducted in a constant elec-

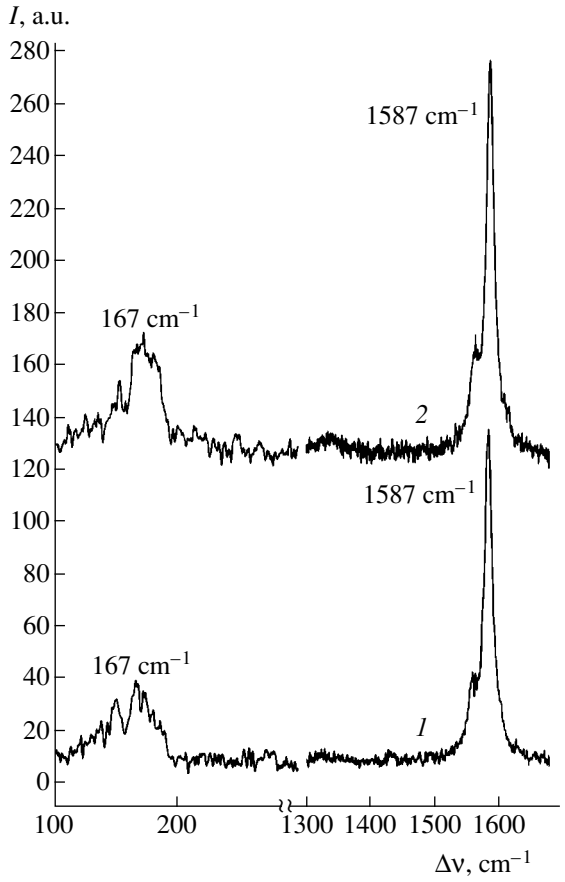

Fig. 1. Raman spectra of the carbon deposits collected (*1*) on the substrate and (*2*) on a diaphragm (spaced by 2 and 6 cm, respectively, from the laser-ablated carbon target).

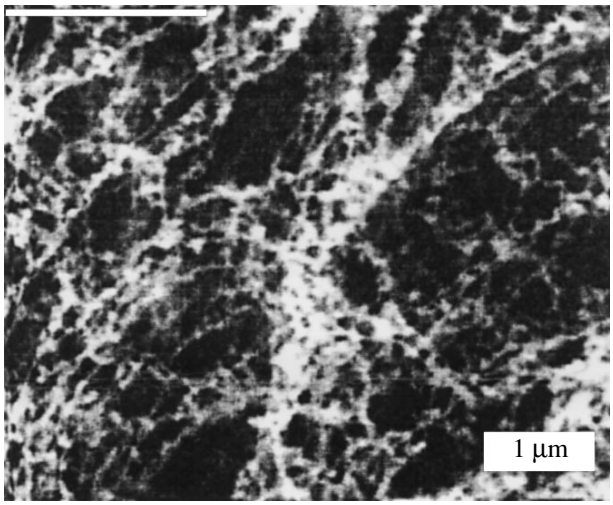

Fig. 2. Scanning electron micrograph of a carbon web.

tric field generated between various elements situated in the reactor volume between the target and the diaphragm. Both the target and the diaphragm were grounded, and a negative potential was applied to the substrate closest (2 cm) to the target. The voltage between this substrate and the target was 400 V.

Application of the electric field leads to a dramatic change in a macroscopic pattern of the process: instead of deposition of the typical carbon products on various parts and the reactor walls, almost the entire reactor volume between the target and the diaphragm is filled with a very fine network structure having the form of a carbon web. The web is formed between various parts and elements of the device, as well as between walls of the quartz reactor and various elements of the substrate holder. There was an impression that most coarse fibers of the web were oriented in the direction of field lines. Since virtually no usual carbon deposit was formed, we can ascertain that switching on the electric field led to conversion of 80–85% of the total amount of carbon evaporated from the graphite–catalyst target into the weblike carbon structures. Such a dramatic change in the macroscopic pattern of the process may reflects the field-induced changes probably taking place in the mechanism of synthesis of the carbon nano- and microstructures.

Figure 1 shows the Raman spectra of the deposits collected from the substrate and the diaphragm, representing a predominantly weblike material. The structure of these spectra is typical of the SCNTs (with a characteristic splitting of the axial mode and a line shift of $\Delta\nu = 1587$ cm^{-1}), which is evidence of the SCNT synthesis in our experiments. The radial mode observed in the low-frequency part of the spectrum ($\Delta\nu = 150$–200 cm^{-1}) bears information about the spectrum of diameters of the deposited SCNTs. Estimates analogous to those obtained in [5] showed that the carbon web synthesized under the conditions studied comprises SCNTs with the diameters ranging from 1.23 to 1.41 nm, the average value being 1.32 nm. It should be noted that the absence of a peak at 1350 cm^{-1} in the Raman spectrum is indicative of the absence of amorphous carbon in the web.

Details and special features of the microstructure of the weblike material can be determined from the data of scanning electron microscopy. Figure 2 shows a micrograph of the weblike carbon structure. As can be seen, the material consists of involved carbon fibers rather uniformly distributed over the sample volume. Among the fibers, there are very thin ones (20–30 nm in diameter). The fiber junctions apparently contain some particles, but neither the nature of these particles nor any relations between the particles and fibers were established so far. As for the internal structure of the web fibers, the Raman spectra indicate that the fibers are composed of SCNTs. Subsequent investigations will show whether the fibers consist entirely of SCNTs or may contain some other carbon clusters and/or structures.

The strong influence of an applied electric field acting as a controlling factor upon the SCNT synthesis can be rationalized as follows. First, the external electric

field induces a dipole moment in the growing molecules. Owing to this, the neighboring molecules or associates with the dipole moments identically aligned in the field exhibit attraction due to the dipole–dipole interaction and, thus, form chain structures favoring the formation of nanotubes. Second, the inhomogeneous electric field generated under the conditions studied acts upon a dipole with the force $F = p_e\Delta E/\Delta l$, where p_e is the dipole moment of a molecule or associate and $\Delta E/\Delta l$ is the electric field gradient. Under the action of this force, the dipoles move to the region of a stronger field and are attracted to charged bodies. Application of the electric field leads essentially to electrophoresis (i.e., to the motion of charged nanoparticles and other species with induced dipole moments suspended in a gaseous medium), which favors effective trapping of the migrating particles with the web formation. For this reason, using the electric field, it is possible to control the synthesis of carbon nanotubes and modify the properties of the synthesized structures. From the standpoint of practice, it would be important to transform the carbon web into a continuous high-strength fiber material. This would open the way to the development of a technology for the obtaining of nanoconductors, either directly or by filling the nanotubes with a an appropriate metal, thus creating a nanocomposite material.

At first glance, it might seem that the process of synthesis of nanostructures in the jet of laser ablation products in an external electric field, as it was studied in our experiments, is very close to the process taking place during the synthesis of carbon nanotubes in an electric arc discharge. However, the two processes are substantially different, since the evaporation and synthesis stages in the arc discharge are interrelated. The decreasing current–voltage characteristic of the arc discharge does not allow the voltage and current to be varied independently. In order to increase the evaporation rate, we have to increase the current, but this leads to a decrease in the discharge voltage. In our experiments, the stages of evaporation and synthesis are separated, since the rate of evaporation is determined by the laser radiation power density, while the electric field strength controlling the synthesis of nanostructures can be changed independently and set almost arbitrarily.

Presently, the experiments are in progress to determine the control parameters of the process and to develop effective methods for the synthesis of SCNTs with preset parameters determining the electrical and mechanical characteristics of the material.

Acknowledgments. The author is grateful to N.G. Solov'ev and V.A. Kuznetsov for their help in this work.

This study was partly supported by the Russian Foundation for Basic Research, project no. 02-01-00452.

REFERENCES

1. S. Iijima, Nature **354**, 56 (1991).
2. A. V. Eletskii, Usp. Fiz. Nauk **172**, 401 (2002) [Phys. Usp. **45**, 369 (2002)].
3. É. G. Rakov, Usp. Khim. **69**, 41 (2000).
4. W. K. Maser, E. Munoz, A. M. Benito, *et al.*, Chem. Phys. Lett. **292**, 587 (1998).
5. G. Assovskii and G. I. Kozlov, Dokl. Akad. Nauk **388** (3), 349 (2003) [Dokl. Phys. Chem. **388**, 13 (2003)].
6. G. I. Kozlov, Kvantovaya Élektron. (Moscow) **29**, 177 (1999).

Translated by P. Pozdeev